A Study of Nuclear Sizes of Unstable Nuclei

(不安定原子核の大きさに関する研究)

山　川　　修

A Study of Nuclear Sizes of Unstable Nuclei

by

Osamu Yamakawa

Department of Physics, Nagoya University
Chikusa-ku, Nagoya, Japan

Abstract

The first measurement of the interaction cross sections and the interaction radii of unstable nuclei (He,Li and Be isotopes), were made at 790 MeV/nucleon by using beams of β-unstable nuclei produced by the projectile fragmentation in high-energy heavy-ion collisions.

In high-energy nucleus-nucleus collisions projectile fragments are emitted into a narrow cone with nearly the same velocity as that of the projectile. For example when the incident energy is about 1 GeV/nucleon, the momentum spreads of the fragments both in the tangential and transverse directions are only a few percent of the incident momentum. Specific projectile fragments were selected according to their magnetic rigidity by using a magnetic analysing system and according to their dE/dx and time-of-flight by using scintillation counters.

The interaction cross sections σ_I for collisions between these nuclei and the targets of Be, C, and Al were measured by using a transmission-type experiment. From the measured interaction cross sections the interaction radii of these nuclei were deduced by using the equation

$$\sigma_I(p,t)=\pi[R_I(p)+R_I(t)]^2$$

where $R_I(p)$ is the interaction radius of a projectile nucleus and $R_I(t)$ is that of the target nucleus. In this equation we assumed that the surface diffuseness of nucleus is effectively included in the interaction radius. The separability of $R_I(p)$ and $R_I(t)$ assumed in the equation was found to be valid within ± 0.02 fm due to the observation that the interaction radius of the projectile nucleus is independent of species of the target nucleus and vice versa.

The interaction cross sections and the interaction radii for all the known He and Li isotopes and ^{9}Be were measured, for the first time, and the dependence of the interaction radii on isobars (^{6}He-^{6}Li,^{8}He,^{8}Li) and isotopes (He and Li isotopes) were studied. The interaction radii of light nuclei, including unstable ones, showed the mass number dependence of roughly $1.2 \times A^{1/3}$.

It was also found that the interaction radius of ^{3}He is larger than that of ^{4}He. This is consistent with the difference of their charge radii determined by electron scattering experiments. However, the interaction radius of ^{11}Li was found to be considerably larger than $1.2 \times A^{1/3}$. A measurement of the isobar dependence shows that the interaction radii of ^{6}Li and ^{8}Li are smaller by about 0.1 fm than those of ^{6}He and ^{8}He, respectively.

The interaction radii R_I obtained in this experiment for stable nuclei were compared with the root-mean-square radii R^e_{rms} determined from electron scattering. The semi-classical optical model calculation, which assumes Gaussian density distribution for nuclear matter, reproduced measured R_I and R^e_{rms} reasonably well.

Contents

1. Introduction

Since Rutherford had found the effect of a strong-interaction radius of the atomic nucleus in early alpha-particle scattering (1929), much effort has been made to measure the radii for various nuclei and many methods have been developed during the past 50 years. Although precise information has been obtained from the electron scattering experiments[1,2,3] as well as with other electro-magnetic probes such as muonic X-rays[4] and isotope shifts[5], they are primarily sensitive to charge distribution and thus to proton distribution. Matter distribution and neutron radii should be studied using strong-interacting particles. So far the most reliable result on matter distribution has been obtained by scattering of high-energy protons[6,7,8] from nuclei. High-energy proton experiments have the advantage that the scattering mechanism at high energy is well known and there exists a reliable scattering theory which establishes the relationship between cross sections and free proton-nucleon amplitudes as well as the nuclear densities to be investigated.

Nuclear radii of stable isotopes have been extensively studied by electron scattering, muonic X-ray and optical isotope-shift measurements. The difference in root-mean-square(RMS) radius between isotopes and isotones shows a systematic trend with a strong shell effect, e.g., the difference of radii is large at the beginning of a neutron or proton shell and decreases linearly toward the end of the shell[9].

The isotope-shift measurement has been extended to unstable isotopes[10]. Interesting data have been obtained on Hg and on alkali isotopes. Although the applicability of the method is restricted to specific elements, it already provides a challenging test for our understanding of the nuclear structure. In order to expand the study to a wider region in the (N,Z) plane up to the particle drip line, we used nuclear beams of unstable nuclei.

In the last 10 years, projectile fragmentation process has been studied extensively in high energy nucleus-nucleus collisions[11,12,13]. It has been found that a wide variety of isotopes could be produced in the process and fragments could be emitted into a narrow cone in the direction of the incident beam with the velocity nearly equal to that of the projectile. This characteristic of projectile fragments enables an efficient production of secondary beams of unstable nuclei.

In this experiment we have successfully measured for the first time the interaction cross sections (σ_I) for nucleus-nucleus collisions using beams of unstable nuclei. The σ_I is defined as the cross section for the change of proton and/or neutron number in the incident nucleus. We have then deduced the interaction radii (R_I) of the nuclei from the σ_I measured in a transmission-type experiment. The secondary beams of unstable nuclei were produced by bombarding a Be target with primary beams of ^{11}B, ^{19}F and ^{20}Ne at an incident energy of 800 MeV/nucleon. The beams were accelarated by the high energy heavy ion accelerator (Bevalac) at Lawrence Berkeley Laboratory (LBL). The produced nuclei were selected according to their magnetic rigidity (P/Z), the velocity (βc) and the charge (Z). The secondary beams of the identified nuclear species , e.g., all He,Li,Be,B isotopes and some C and N isotopes, were projected onto reaction targets of Be,C and Al to measure the attenuation of the beam intensity due to the nuclear reactions. The same selection procedure was used to determine the number of non-interacting nuclei, however, in this case the magnetic rigidity, the velocity and the charge were determined after they had passed through the reaction target.

The interaction cross section σ_I is written as

$$\sigma_I = \frac{A}{N_A\, t} \ln \frac{N_{inc}}{N_{out}} \tag{1.1}$$

where A is the mass number of the target, N_A is the Avogadro number, t is the target thickness in g/cm^2, N_{inc} is the number of incident nuclei and N_{out} is the number of non-interacting nuclei.

The interaction cross section at the present energy region is simply related to the elementary nucleon-nucleon total cross section, and the average nucleon density $\rho(r)$ at radius r, under the condition that the nucleons in the target nucleus scatter or absorb the nucleons in the projectile nucleus independently of each other. For the independent condition to hold strictly, it is necessary that the nucleon de Broglie-wavelength λ and the range of nucleon-nucleon interactions be smaller than the average internucleon spacing. The nucleon-nucleon interaction range is $c\,\tau = 0.3\times10^{-13}$ cm, where c is the velocity of light and τ is the interaction period for a strong interaction. At 790 MeV/nucleon, λ=0.14×10^{-13} cm and the mean nucleon-nucleon separation is about 1.8×10^{-13} cm so the condition is well satisfied.

The interaction cross sections for stable nuclei are known to be essentially independent of the beam energy in this energy region. It is therefore plausible that the interaction cross section reflects a well-defined geometrical nuclear size in this energy region. It is thus natural to express the interaction cross sections $\sigma_I(p,t)$ by the interaction radii R_I as follows

$$\sigma_I(p,t)=\pi[R_I(p)+R_I(t)]^2 \tag{1,2}$$

where p and t denote the projectile and target nucleus respectively. The validity of this relation is strengthened by the fact that the deduced radii $R_I(p)$ and $R_I(t)$ are independent of the combination of projectile and target nuclei.

This thesis will report the results of the measurements made with He and Li isotopes. In chapter 2 the principle and the method of the experiment are described. The production and the properties of the secondary beams are also described. The data analysis method is explained in chapter 3. Sources of error and data corrections are discussed. The interaction cross sections and interaction radii deduced from the interaction cross sections are reported in chapter 4. The results of this experiment are compared with the other experimental results in chapter 5.

2. Experimental method

2.1. Production of the secondary beam

The secondary beams of unstable nuclei as well as stable nuclei were used in the present experiment. In this section, the production method of the secondary beam is described. First, we discuss the production mechanism of unstable nuclei. Second, the principle of selecting the secondary beam of interest is discussed. Finally we describe the secondary beam line which we used.

2.1.1. Projectile fragmentation

In high-energy nucleus-nucleus collisions, only those constituent nucleons in a projectile nucleus, which interact with other constituent nucleons in a target nucleus, take part in strong nucleon-nucleon collision, and they are classified as participants. While other nucleons, which did not interact strongly with other nucleons, remain intact as spectators. Figure 1 shows a schematic picture of this process. Spectators, the projectile fragments in other words, move at the same speed as that of the incident beam[11].

It was found[14] that the projectile fragments have, in the rest frame of the projectile, a Gaussian momentum (P) distribution

$$W(P)=\exp\frac{-P^2}{2s^2}$$

with

$$s=s_0\sqrt{\frac{F(B-F)}{B-1}} \qquad (2.1)$$

where B is the mass number of the beam, F is the mass number of the fragment, and $s_0 = 90$ MeV/c corresponding to the Fermi momentum in the nucleus. The longitudinal momentum

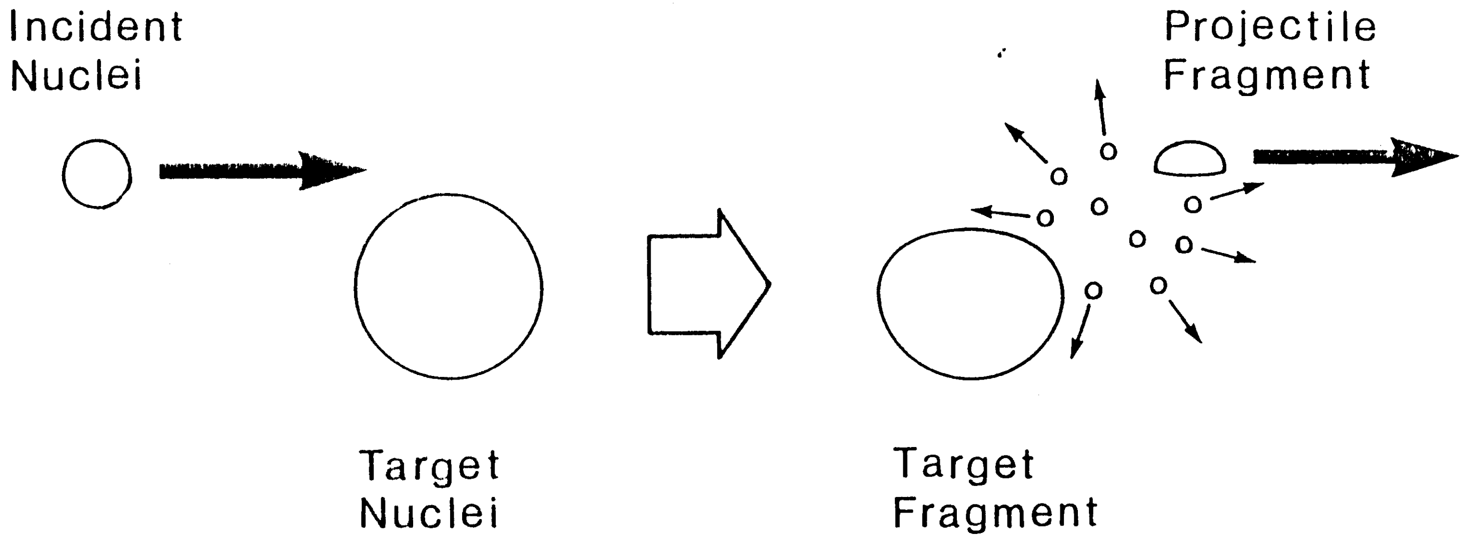
Incident
Nuclei
Target
Nuclei
Projectile
Fragment
Target
Fragment

Figure 1

spread (ΔP) of a fragment in the laboratory system is

$$\Delta P = \frac{s}{\sqrt{1-\beta^2}} \tag{2.2}$$

For instance when 800 MeV/nucleon ^{11}B is used as a primary beam, the momentum spread (ΔP) of ^{8}He in the laboratory frame is about 2.2 %. The spread in emission angle ($\Delta\theta$) is about 0.7 degree. A high collection efficiency is expected when the projectile fragments are used as a secondary beam, because of these characteristics of the projectile fragment.

2.1.2. The principle of selection for nuclide

In order to separate nuclide of interest from various other nuclear species produced in the projectile fragmentations, the nuclei must be sorted using both the mass number (A) and the charge (Z) of the nucleus. For this purpose, the magnetic rigidity (P/Z), the energy loss (dE/dx) and the velocity (βc) are used. The detail of each selection is discussed below.

(1) The magnetic rigidity (P/Z) was selected by adjusting the bending magnets, the focussing magnets and the collimation slits in the secondary beam line.

The principle of rigidity selection is shown schematically in Fig. 2. The primary beam is projected onto the production target positioned at F1, the focus of the primary beam. Among the various nuclear species produced in the production target, the nuclei with different rigidity are focused onto different positions at F2 through the bending and focussing magnets. A pair of Cu blocks was placed at F2 to degrade the energy of nuclei which have rigidity values different from that of the nuclei of interest. Only the nuclei with selected rigidity are then transported to the experimental area through the secondary beam line. Because projectile fragments are emitted with velocity equal to that of the incident beam, the rigidity separation is almost identical to the A/Z separation because $P/Z = pA/Z = \beta mA/(Z\sqrt{1-\beta^2})$ and β is almost constant.

Schematic diagram for rigidity selection

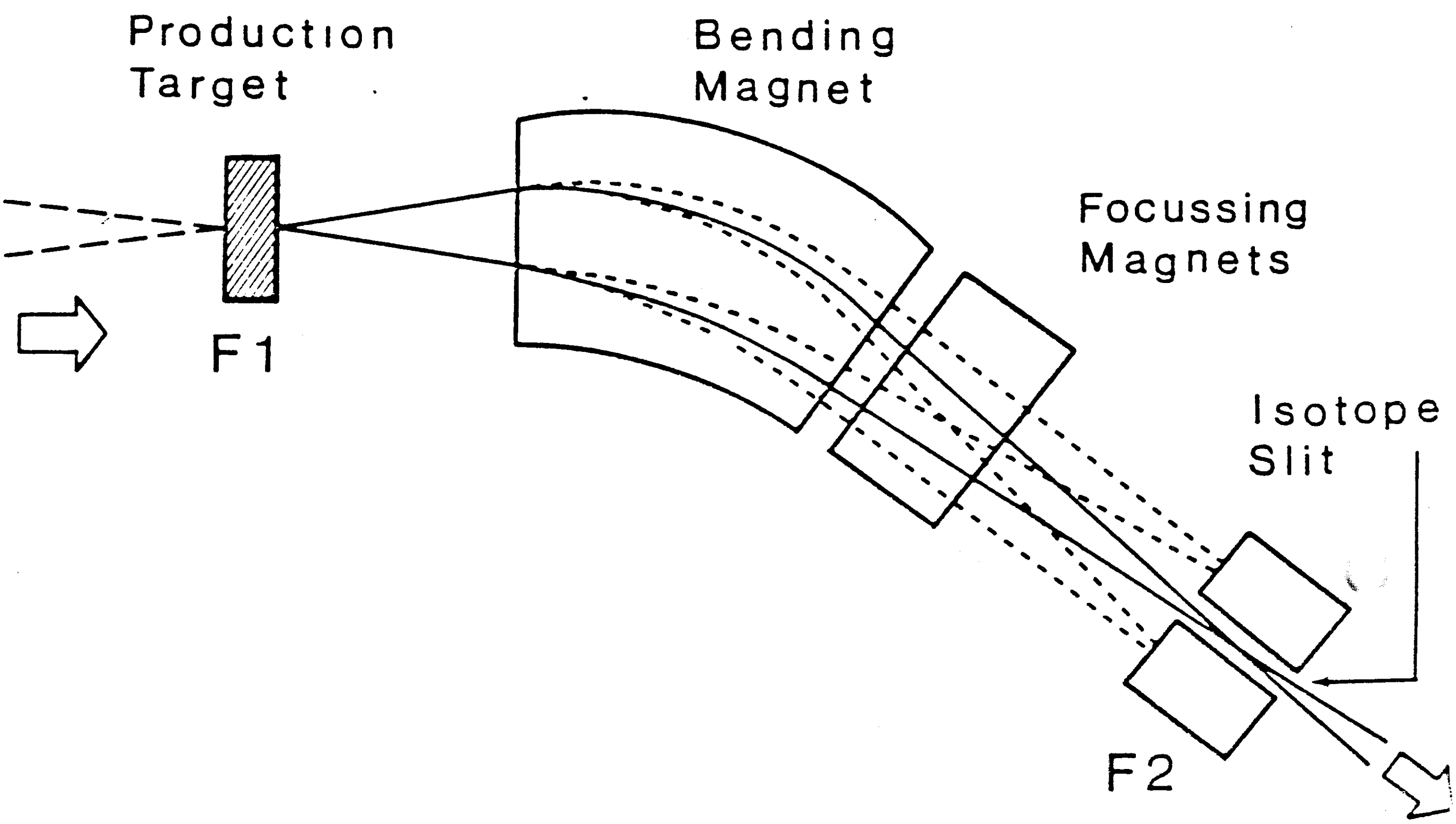

Figure 2

Here m is the nucleon mass and p is the momentum of one nucleon.

Figure 3 shows an example of intensity distribution of various nuclide at F2, when the ^{12}C primary beam is used. In this case the bending and focussing magnets are adjusted so as to select $A/Z \approx 3$. When we set a slit of 5 mm width at the center of distribution, the secondary beam of ^6He, ^9Li and ^3H will be obtained. After the magnetic rigidity selection, the secondary beam is still a mixture of nuclei with different charges.

(2) The charge of the nucleus was identified by the pulse height in the scintillation counters.

When a relativistic particle passes through a plastic scintillator, the pulse height is almost proportional to Z^2 for small Z. Figure 4 shows a pulse height distribution in a scintillation counter, when ^6He, ^9Li, and ^3H were selected by the beam line. The ^3H peak is not seen in this figure because most of the ^3H was disregarded by setting the discriminator threshold to be higher than the ^3H pulse height. Clear separation between ^3H, ^6He and ^9Li was observed.

(3) Time-of-flight (TOF) was measured by two scintillation counters (50 m separation) to determine the particles velocity.

When two or more isotopes of the same charge were mixed in a rigidity region, they were separated by their velocity. In this experiment, which covers only a small mass range $A < 12$, the separation of nuclear species by their rigidity and charge was so clear that TOF separation was used only to reduce the background in the beam.

2.1.3. The beam line for secondary beam at the Bevalac

The secondary beam line used in this experiment at the Bevalac of Lawrence Berkeley Laboratory is shown schematically in Fig 5. The primary ^{11}B beam was focused at F1 , the first focus after extraction of beam from the Bevalac, and here a production target of Be (5 g/cm^2 in

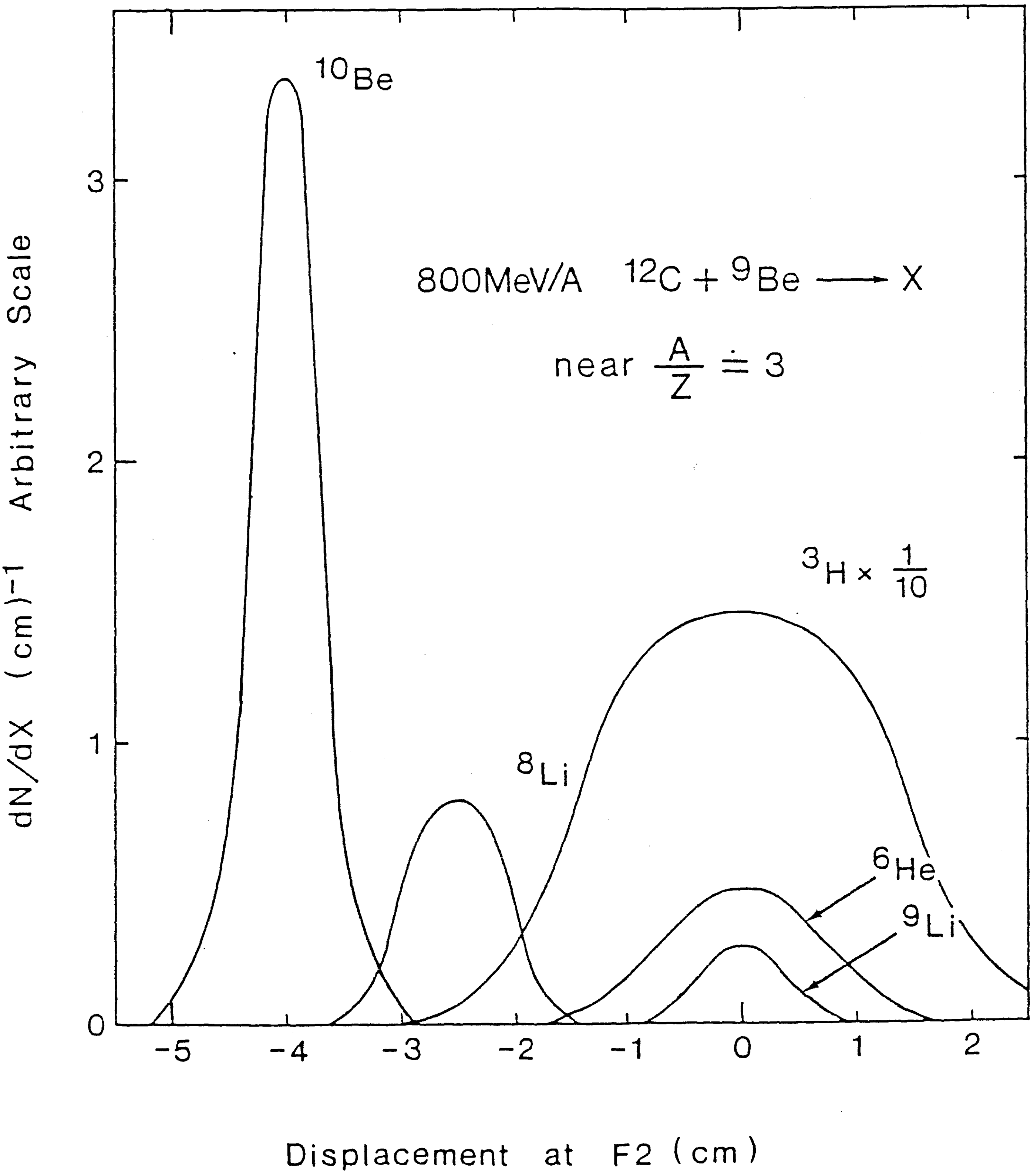

^{10}Be
800MeV/A ^{12}C + ^{9}Be ⟶ X
near $\frac{A}{Z} \doteq 3$
^{3}H × $\frac{1}{10}$
^{8}Li
^{6}He
^{9}Li
dN/dX (cm)$^{-1}$ Arbitrary Scale
Displacement at F2 (cm)
0
1
2
3
-5
-4
-3
-2
-1
0
1
2

Figure 3

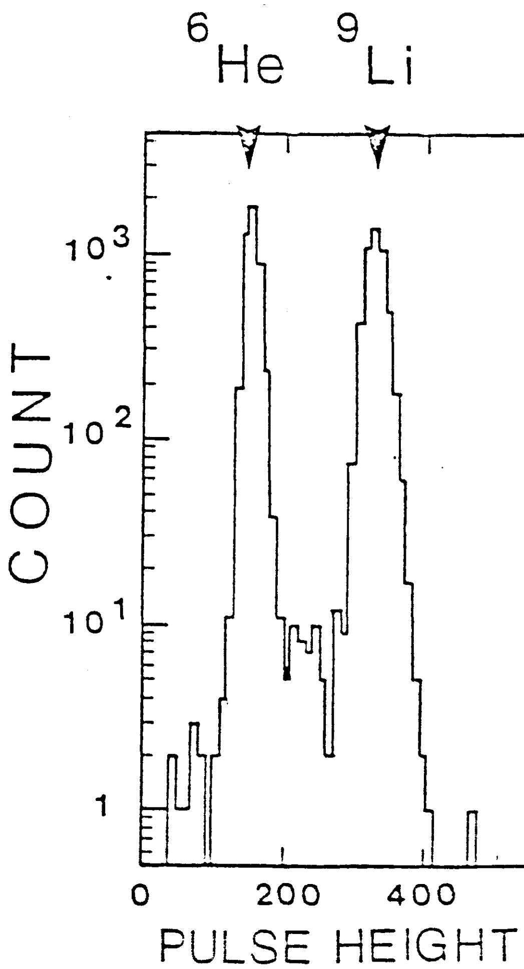

Figure 4

Figure 5

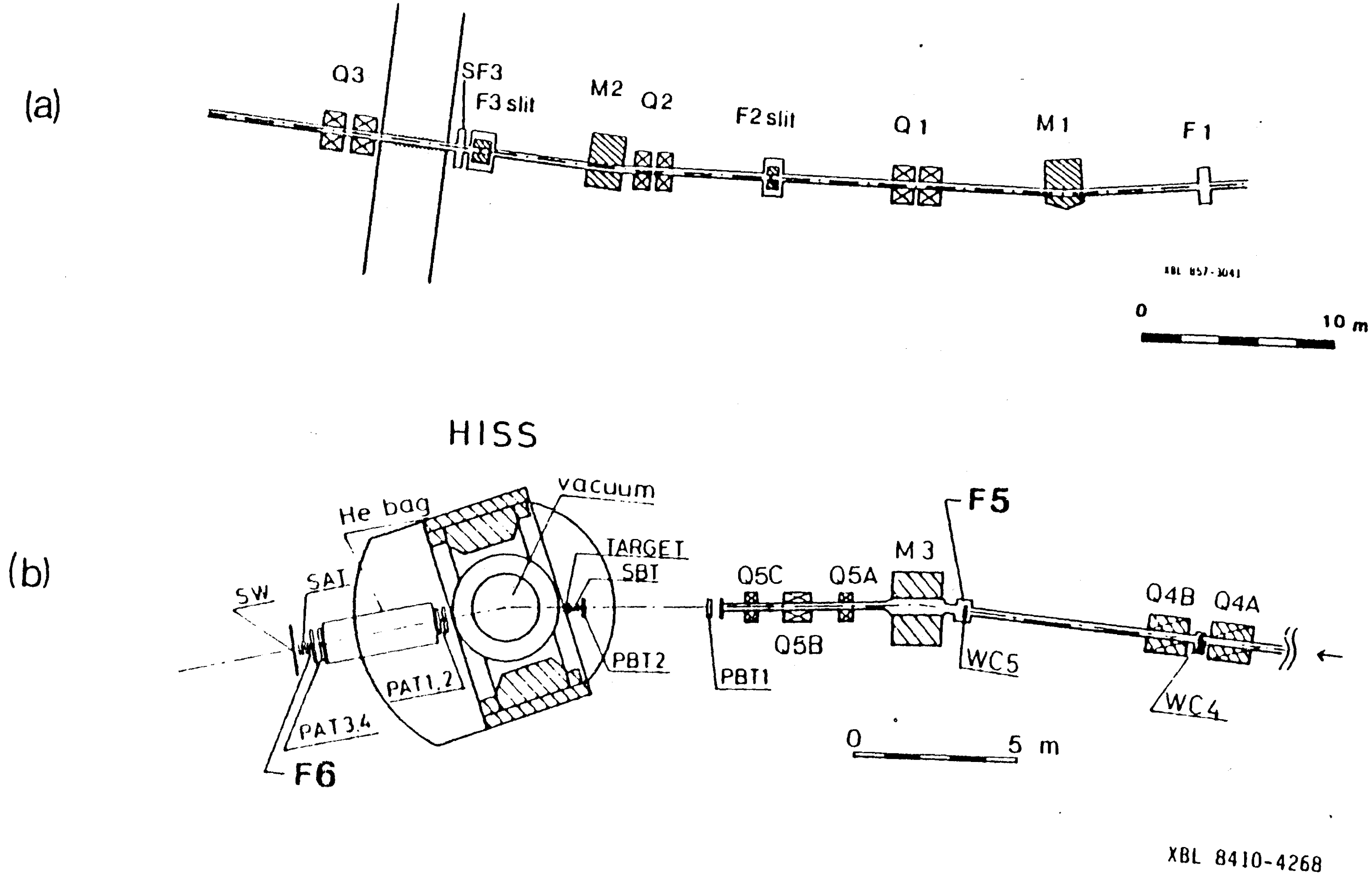
(a)
Q3
SF3
F3 slit
M2
Q2
F2 slit
Q 1
M 1
F 1
XBL 857-3041
0
10 m
HISS
(b)
He bag
vacuum
TARGET
SBT
SW
SAT
PAT1,2
PAT3,4
PBT2
PBT1
F6
Q5C
Q5A
Q5B
M 3
F5
WC5
Q4B
Q4A
WC4
0
5 m
XBL 8410-4268

thickness)

was positioned.

The uncertainty in secondary-beam momentum arises from two sources. One is the momentum spread due to the production reaction, which depends on the mass number of the incident and the product nuclei. (See Eq. (2.1) and Eq. (2.2)) The other is due to the difference in the energy loss in the target between the incident and the product nuclei. The mechanism which produces the energy broading is schematically shown in Fig. 6. When an incident nucleus reacts at the entrance of the target, the energy loss in the production target is that of the product nucleus. When an incident nucleus reacts at the exit of the target, the energy loss in the production target is that of the incident nucleus. When the interaction occurs somewhere in the middle of the target, the energy loss is in between. When the production target is thicker, the yield of the secondary product will be greater as well. However, when the momentum spread is larger, lower transmission efficiency through the beam line must be tolerated

The thickness of the production target was chosen so that the momentum spread of the product nuclei due to the difference in energy losses of the incident and the product nuclei, is comparable to the momentum spread due to the production reaction. The relation between momentum spread and the thickness of production target is shown in Fig. 7. Here, ^{8}He is produced by the fragmentation of ^{12}C nucleus on Be target. From Fig. 7 it is seen that a Be production target with thickness 5 g/cm^2 is optimum.

Various nuclear species produced in the production target were then transported through the bending magnet (M1) and a set of focussing magnets (Q1) to the momentum dispersive focus, F2. Isotopes with different rigidities were focused on different positions at F2 as described in the previous section. We placed the isotope slit made of a pair of Cu blocks (35 cm in length) at F2 for degrading the energy of other species which have different rigidity from that of the

Schematic diagram for energy loss in production target

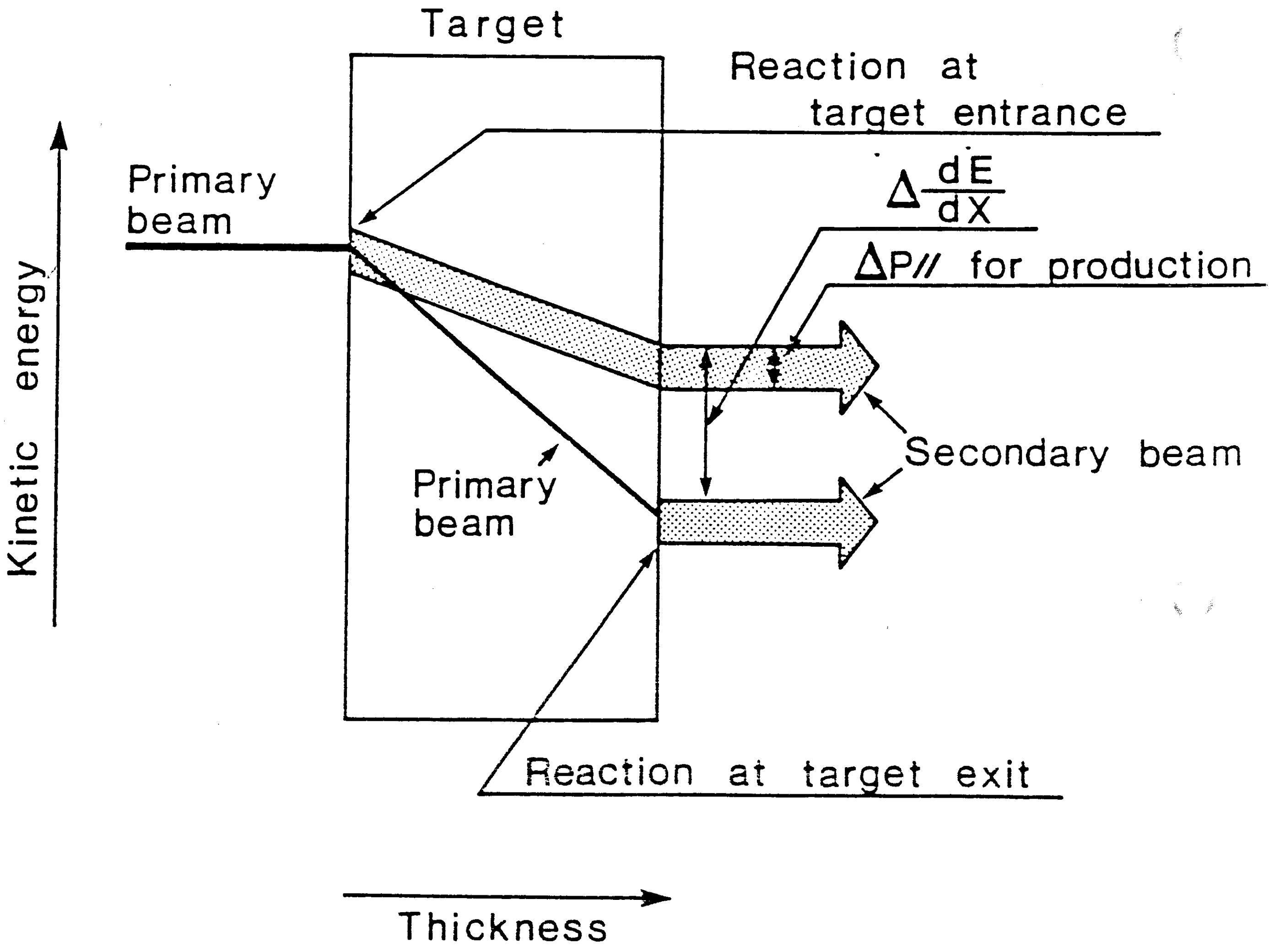

Figure 6

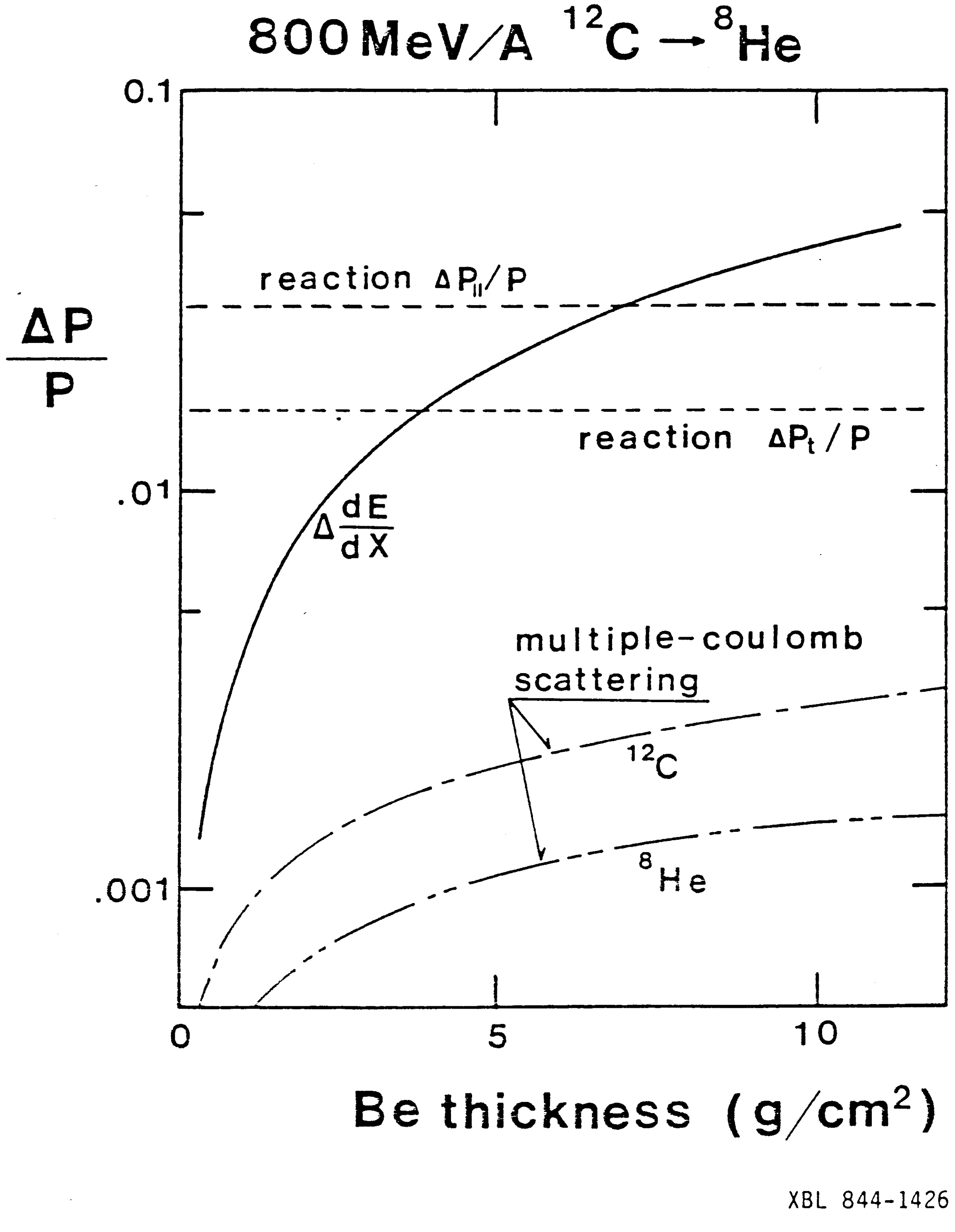
800 MeV/A $^{12}C \rightarrow ^{8}He$
0.1
.01
.001
$\frac{\Delta P}{P}$
reaction $\Delta P_{\parallel}/P$
reaction $\Delta P_t/P$
$\Delta\frac{dE}{dX}$
multiple-coulomb scattering
^{12}C
^{8}He
0
5
10
Be thickness (g/cm^2)
XBL 844-1426

Figure 7

isotopes of interest. A clean-up collimator slit (50 cm in length) was placed at an achromatic focus F3 after another bending magnet (M2) and a set of focussing magnets (Q2) (See Fig.5). A momentum spread of a few percent was attained by transporting the rigidity spread nuclei to the experimental area.

The procedure of selecting the nuclei of interest is as follows: The incoming isotopes are selected by a scatter plot of pulse height and TOF. Then the widths of the slits at F2 and F3 are determined such that the ratio (Intensity of secondary beam)/(Intensity of primary beam) is maximized under the condition that the background nuclei in the scatter plots is minimal.

2.1.4. The Property of secondary beam

In this experiment, ^{11}B, ^{19}F and ^{20}B were used as primary beam. The following secondary beams were produced from these primary beams,

$^{11}B \rightarrow {}^{3}H$,

$^{3}He, {}^{4}He, {}^{6}He, {}^{8}He$,

$^{6}Li, {}^{7}Li, {}^{8}Li, {}^{9}Li$,

$^{7}Be, {}^{9}Be, {}^{10}Be$

$^{19}F \rightarrow {}^{10}B, {}^{12}C, {}^{14}N$

$^{20}Ne \rightarrow {}^{11}Li$,

$^{11}Be, {}^{12}Be, {}^{14}Be$,

$^{8}B, {}^{11}B, {}^{12}B, {}^{13}B, {}^{14}B, {}^{15}B$,

$^{10}C, {}^{13}C, {}^{15}C, {}^{16}C$,

$^{15}N, {}^{17}N$

Scatter plots and histograms of the pulse height vs. the TOF of each He isotope are shown in Figs. 8 - 11, and those of Li isotopes are shown in Figs. 9,10,12,13. The charge separation between nuclei with selected rigidity but differing charge was so clear that the proportion of nuclei with a charge state different from that of the nucleus of interest was well less than 10^{-3}. Full widths at half maximum (FWHM) of the TOF spread were 1.3 to 1.7 nano-second, which correspond to momentum spreads of 2.6 to 3.4 percent for He isotopes. When ^{8}He was transported, we opened the slit at F2 wide enough to cover the entire momentum spread so that the maximum yield of ^{8}He isotopes was obtained. In other cases (^{3}He,^{4}He,^{6}He), only a narrower portion of the secondary beams was selected by the smaller slit width at F2. The running conditions for He isotopes and Li isotopes are summarized in Table 1.

2.2. Measurement of interaction cross sections

2.2.1. Definitions of the interaction cross section and the interaction radii

The interaction cross section is defined to be the cross section for the change of proton and/or neutron number in the incident nucleus. We used the transmission method to measure the attenuation of incident nuclei in the reaction target. Both the incoming nuclei and the outgoing nuclei were identified, and the number of incident nuclei and the number of non-interacting nuclei were counted. The counter system after the reaction target was large enough to detect most of the non-interacting nuclei which experienced Coulomb scattering or nuclear elastic scattering.

The interaction cross section σ_I was calculated by the following equation

$$\sigma_I = \frac{A}{N_A\, t} \ln \left[\frac{\gamma_0 (1-P_m)}{\gamma} \right] \qquad (2.3)$$

Running condition of beam line				
Discription	^3He	^4He	^6He	^8He
^{11}Be intensity (per one pulse)	2×10^8	1×10^7	2×10^7	2×10^8
Opening width				
F2 Slit (cm)	1.02	0.54	0.76	2.30
F3 Slit (cm)	1.27	1.81	1.52	1.80
# of count (typical)				
at F3	10000	20000	2500	1000
trigger	1000	1500	1000	400
accepted trigger	500	700	320	270
width of TOF FWHM (ns)	1.3	1.4	1.4	1.7
correspone to $\Delta P/P(\%)$	2.6	2.8	2.8	3.4

Table 1

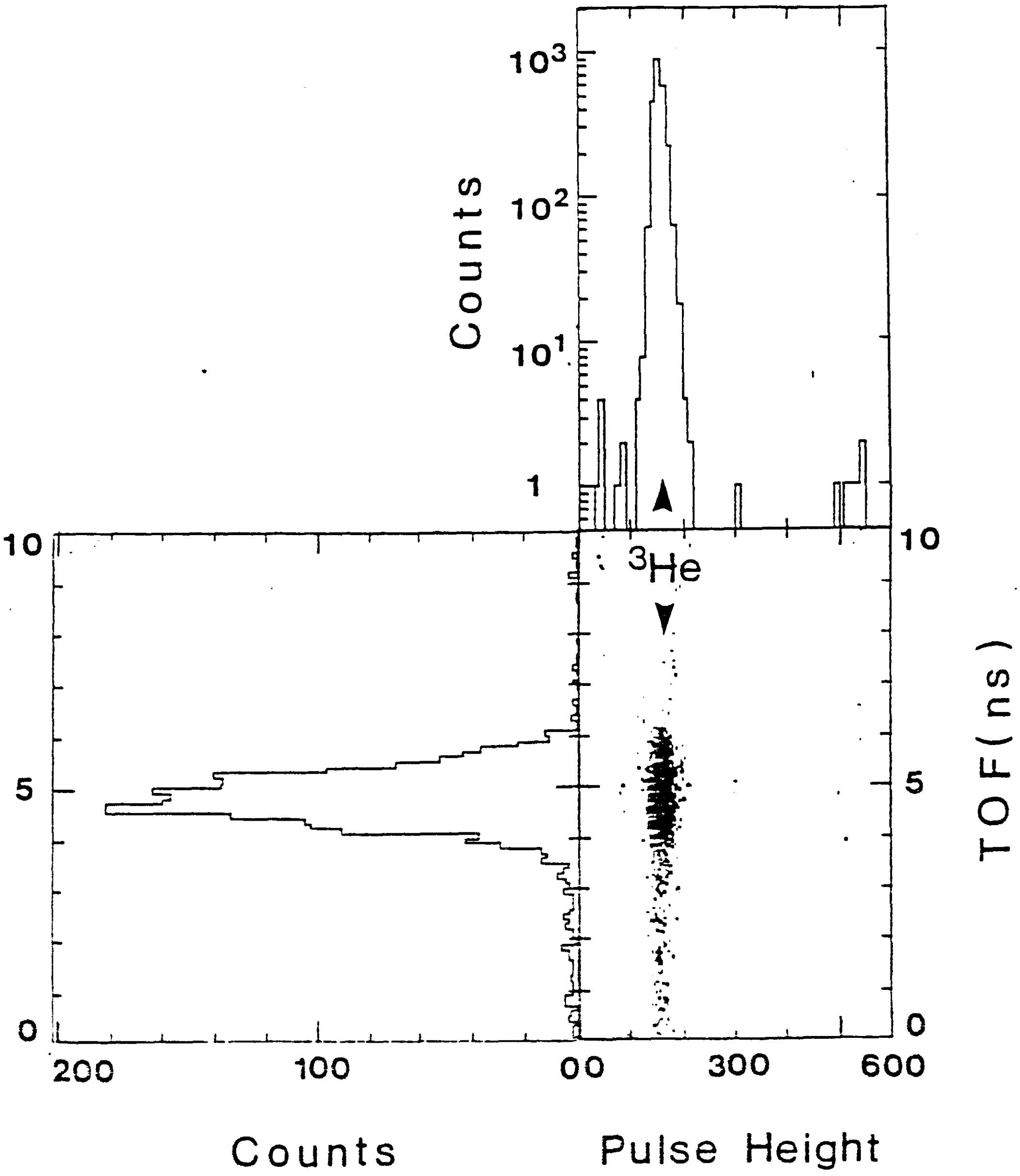

Counts
10^3
10^2
10^1
1
^{3}He
10
5
0
200
100
00
300
600
Counts
Pulse Height
TOF(ns)

Figure 8

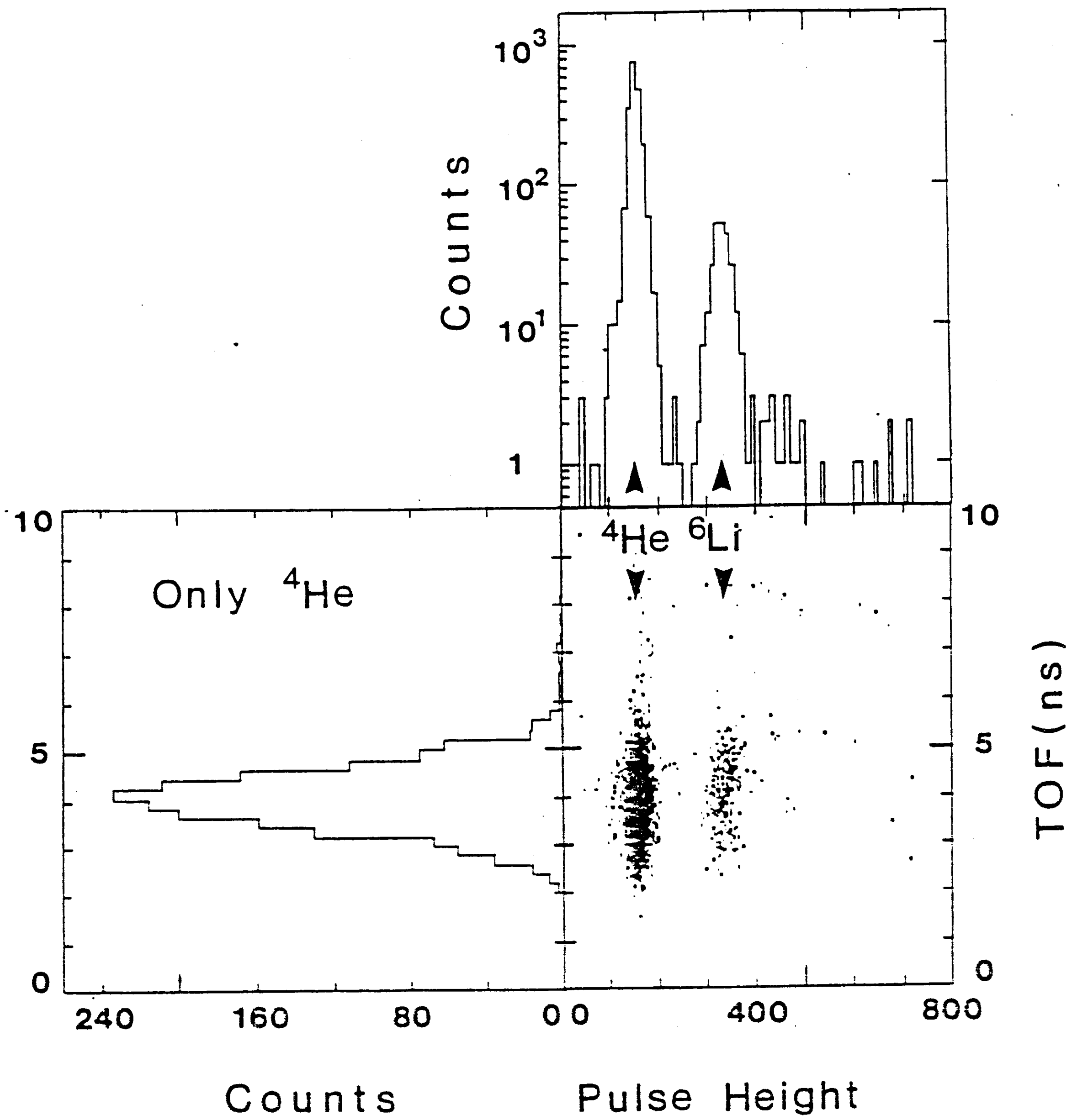

Counts
10^3
10^2
10^1
1
10
Only ^{4}He
^{4}He ^{6}Li
5
0
240
160
80
0 0
400
800
10
5
0
TOF(ns)
Counts
Pulse Height

Figure 9

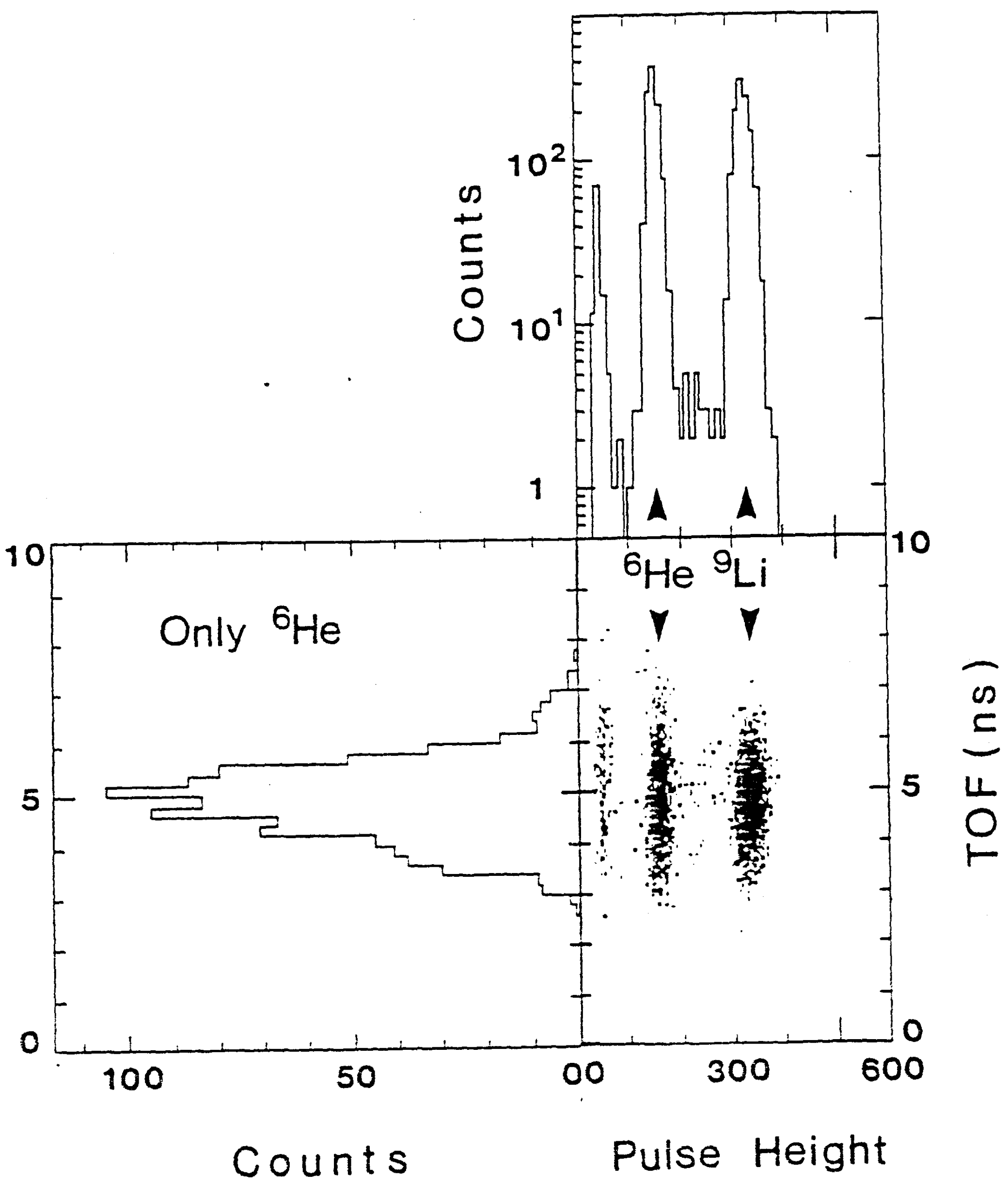
Counts
10^2
10^1
1
10
5
0
Only ^{6}He
100
50
0
Counts
^{6}He ^{9}Li
0
300
600
Pulse Height
TOF (ns)

Figure 10

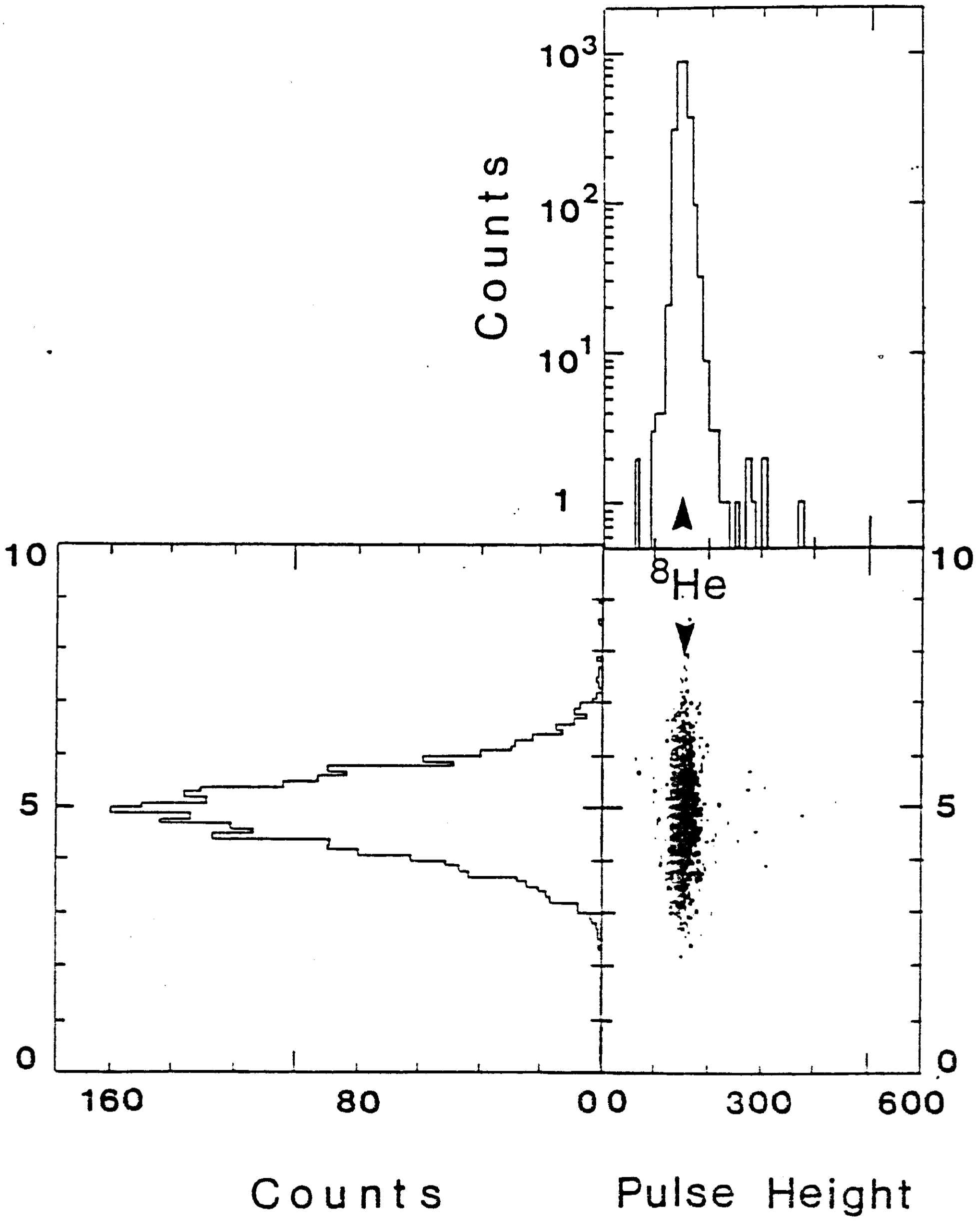
Counts
10^3
10^2
10^1
1
^{8}He
10
5
0
160
80
0 0
300
600
10
5
0
TOF(ns)
Counts
Pulse Height

Figure 11

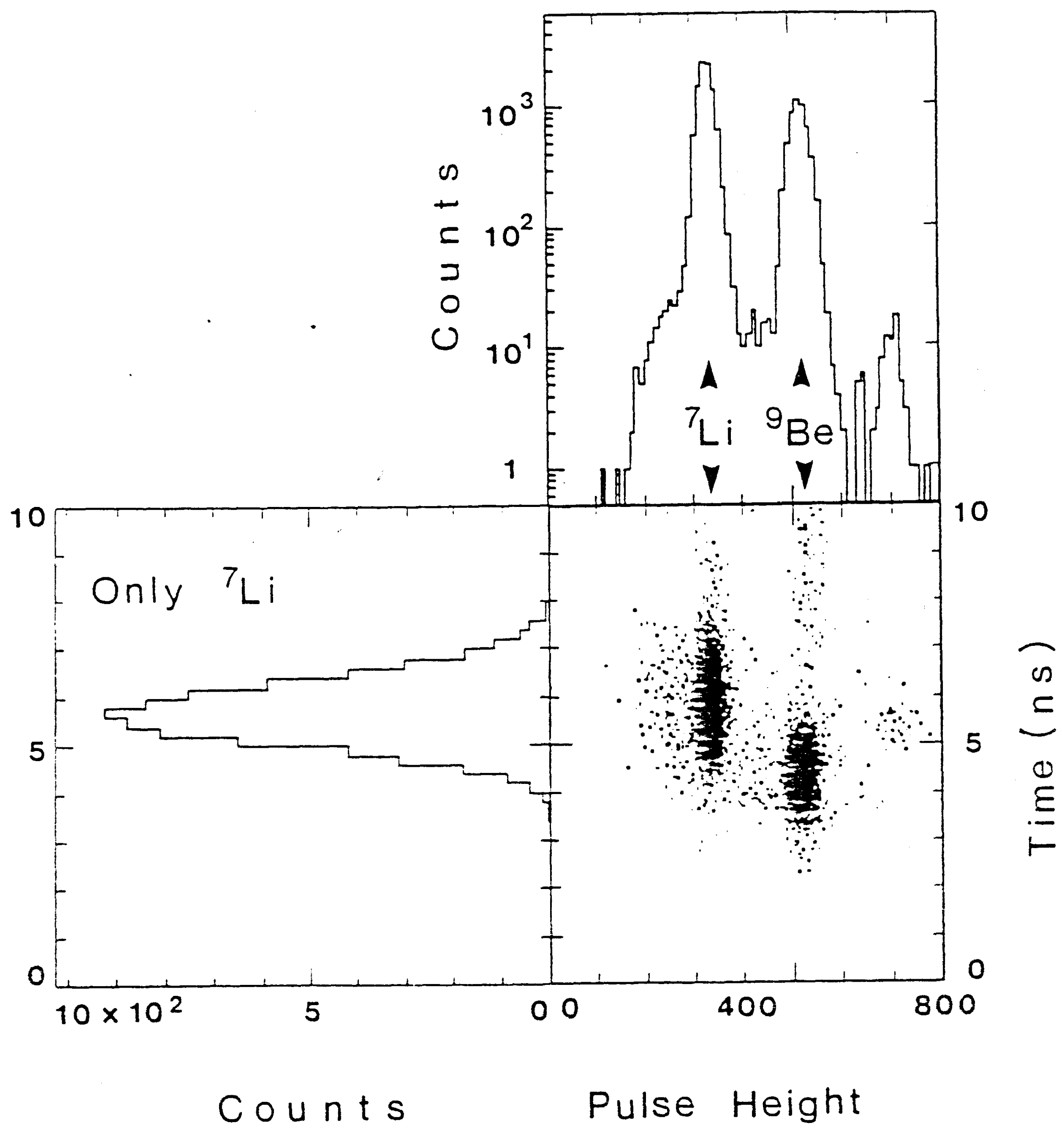
Counts
10^3
10^2
10^1
1
^{7}Li
^{9}Be
Only ^{7}Li
10
5
0
10×10^2
5
0
0
400
800
Time (ns)
Counts
Pulse Height

Figure 12

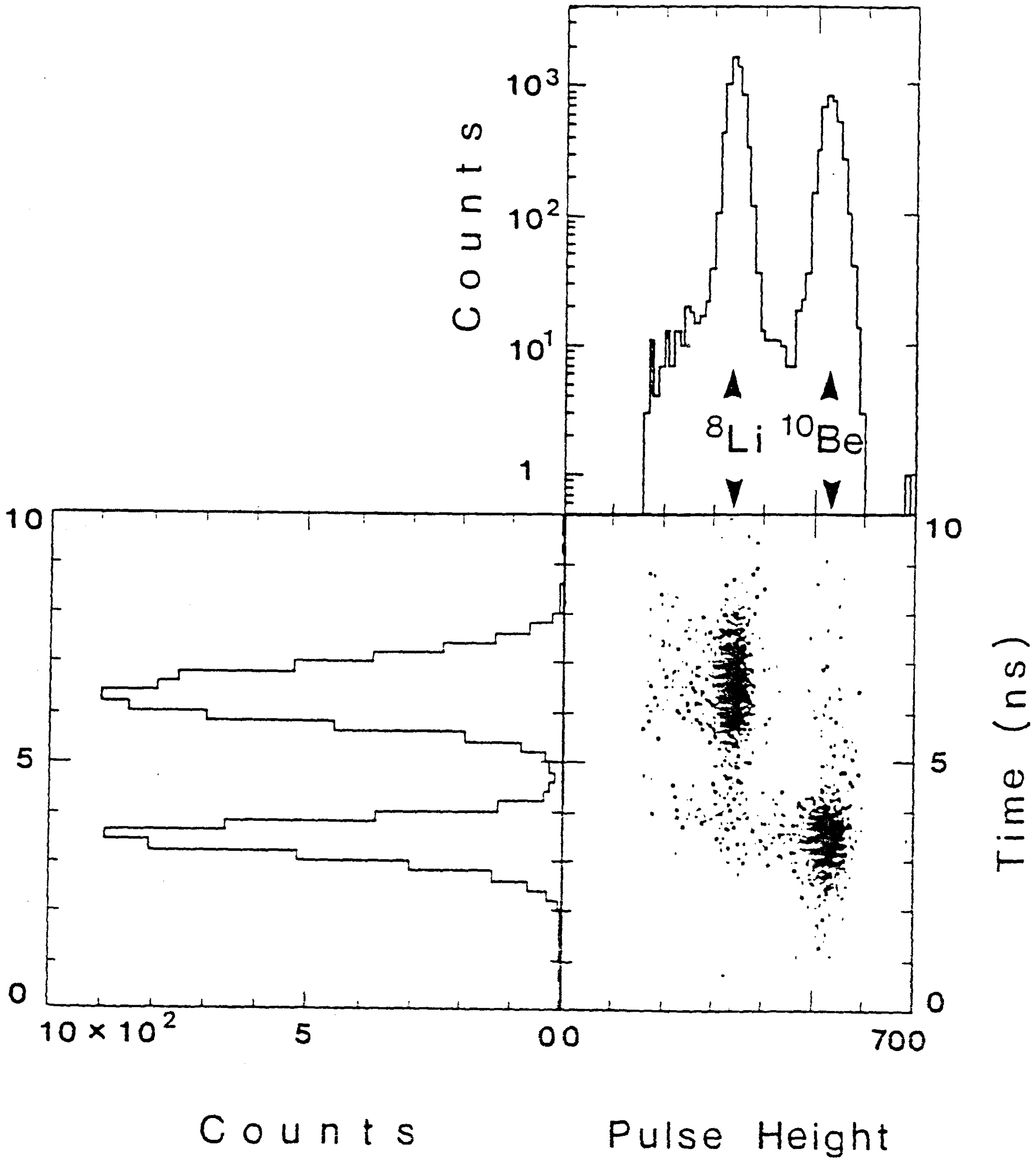
Counts
10^3
10^2
10^1
1
^{8}Li
^{10}Be
10
5
0
10×10^2
5
0 0
700
10
5
0
Time (ns)
Counts
Pulse Height

Figure 13

where A is the mass number and t is the thickness (g/cm^2) of the reaction target, N_A is the Avogadro number. The beam attenuation factor γ is defined as $\gamma = N_{out}/N_{inc}$ for a target-in run (N_{inc} is the number of incoming nuclei, N_{out} is the number of outgoing nuclei which have the same charge and mass as the incident nuclei) γ_0 is the same ratio for a target-out run. By taking the ratio γ_0/γ, uncertainties due to the counter efficiency and reactions occurring outside of the reaction target were automatically corrected. The factor $(1-P_m)$ is a correction for scattering out of non-interacting nuclei out of the counter system after the target due to multiple Coulomb scattering or nuclear elastic scattering.

From Eq. (2.3), we calculated the error in σ_I as

$$\left(\frac{\Delta\sigma_I}{\sigma_I}\right)^2 = \left\{\frac{1-\gamma}{N_{inc}\,\gamma} + \frac{1-\gamma_0}{N_{0inc}\,\gamma_0} + \left[\frac{\Delta(\gamma/\gamma_0)}{(\gamma/\gamma_0)}\right]^2 + \left[\frac{\Delta(1-P_m)}{(1-P_m)}\right]^2\right\}\left(\frac{A}{\sigma_I N_A\, t}\right)^2 + \left(\frac{\Delta t}{t}\right)^2 \tag{2.4}$$

where N_{0inc} is the number of incoming nuclei before the reaction target for a target-out run. The first and second terms are statistical errors which are dependent on the uncertainty of γ and γ_0. The first term are calculated by using the binominal distribution of the numbers N_{out} and N_{0out}, where N_{0out} is the number of the non-intercting nuclei for a target-out run. When the N_{out} follows the binominal distribution, $\Delta N_{out} = \sqrt{N_{inc}\,\gamma\,(1-\gamma)}$ and $\Delta\gamma = (\Delta N_{out}/N_{inc}) = \sqrt{\gamma\,(1-\gamma)/N_{inc}}$. Using this $\Delta\gamma$, the first term of Eq. (2.4) was obtained. The second term is obtained by the same procedure. In this experiment, these two terms were the dominant source of errors. The third term is due to the mixture of the different nuclei. The fourth term comes from the uncertainty in the scattering-out factor P_m. The fifth term comes from the error in determining the thickness of the reaction target, and it was negligibly small in all of the measurements.

The interaction cross sections for stable nuclei are known to be essentially independent of the incident energy above a few hundred MeV/nucleon[12,15]. The nucleon-nucleon cross section shows the saturation at above 800 MeV. It is therefore considered that interaction cross section (σ_I) reflects a geometrical nuclear size. We operationally define a interaction nuclear radius[15] by the equation

$$\sigma_I = \pi[R_I(p) + R_I(t)]^2 \tag{2.5}$$

where $R_I(p)$ and $R_I(t)$ are the interaction radii of the projectile and the target nuclei respectively. We assume the separability of the radii of the target and the projectile nuclei here. In other words, we assume that the Bradt-Peter overlap parameters[16] are zero, as pointed out by D.L.Cheshire et al[17]. The radii of stable nuclei which have been deduced before, using this equation, are plotted in Fig. 14. The behavior of dependence on $A^{1/3}$ is consistent with the half density radius obtained from electron scattering. The validity of the assumption of separability will be checked later using the experimental data, by the independence of the projectile radius from different targets as well as the independence of the target radius from the species of projectile.

2.2.2. Experimental setup

2.2.2.1. General design

The experimental setup is shown schematically in Fig.15 The plan view of the setup is shown in Fig.16.

A plastic scintillation counter was placed in the beam line (See Fig. 5) at F3 (SF3: Scintillation counter at **F3**). In the experimental area, wire chambers (PBT1, PBT2: multi wire **P**roportional chambers **B**efore the reaction **T**arget) and plastic scintillation counters (SBT1 - SBT4: Scintillation counters **B**efore the reaction **T**arget) and a veto scintillation counter were used before the reaction target. A spectrometer magnet (HISS: Heavy Ion Spectrometr System) Wire

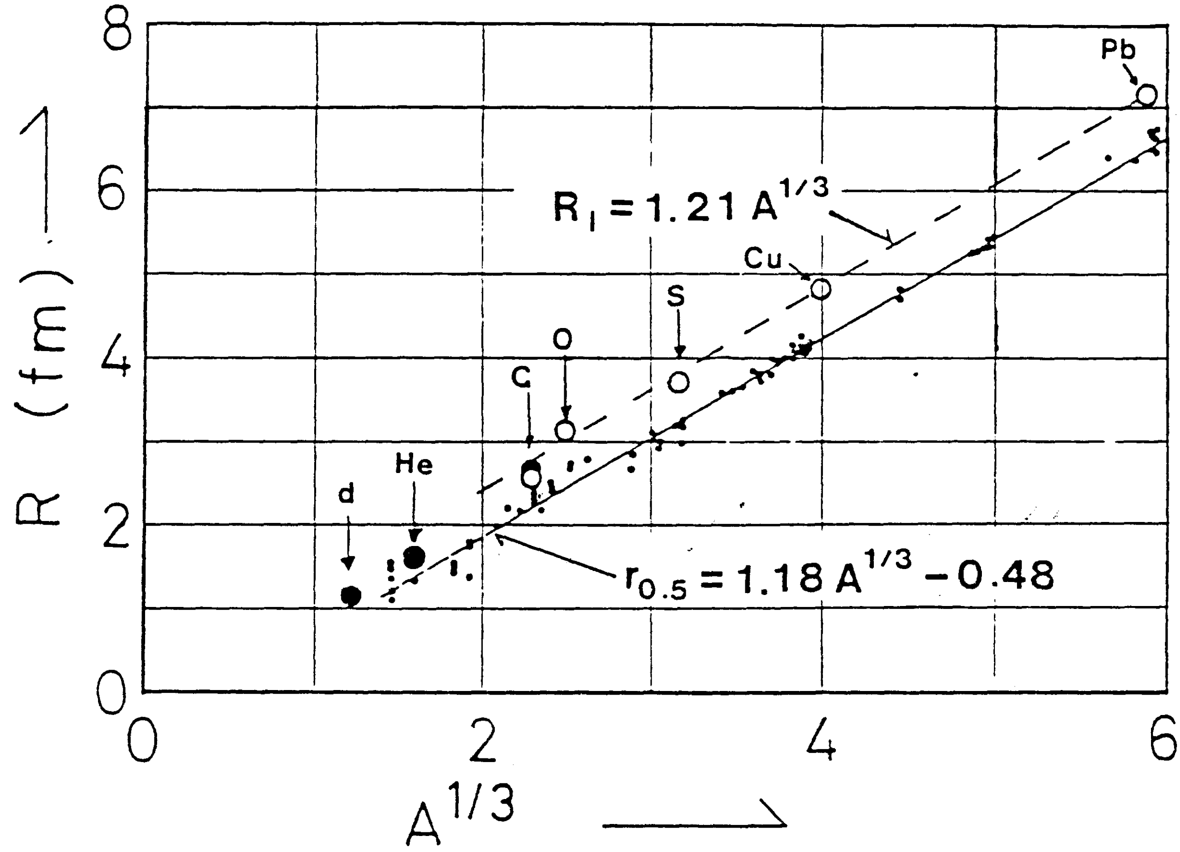

XBL 844-1419

Figure 14

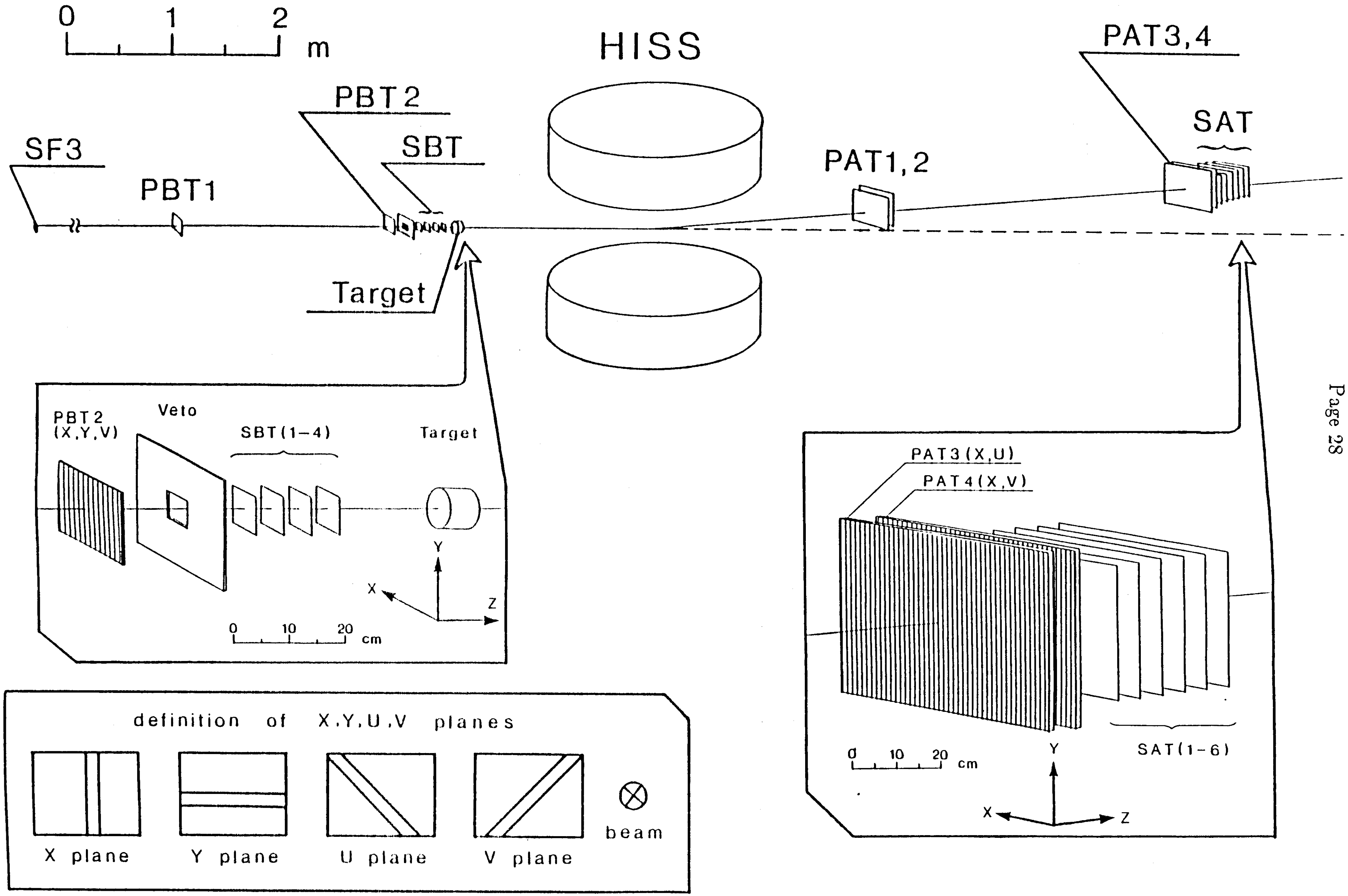
0 1 2 m
HISS
PBT2
SF3
PBT1
SBT
Target
PAT1,2
PAT3,4
SAT
PBT2 (X,Y,V)
Veto
SBT(1-4)
Target
Y
X
Z
0 10 20 cm
PAT3(X,U)
PAT4(X,V)
SAT(1-6)
0 10 20 cm
Y
X
Z
definition of X,Y,U,V planes
X plane
Y plane
U plane
V plane
beam

Figure 15

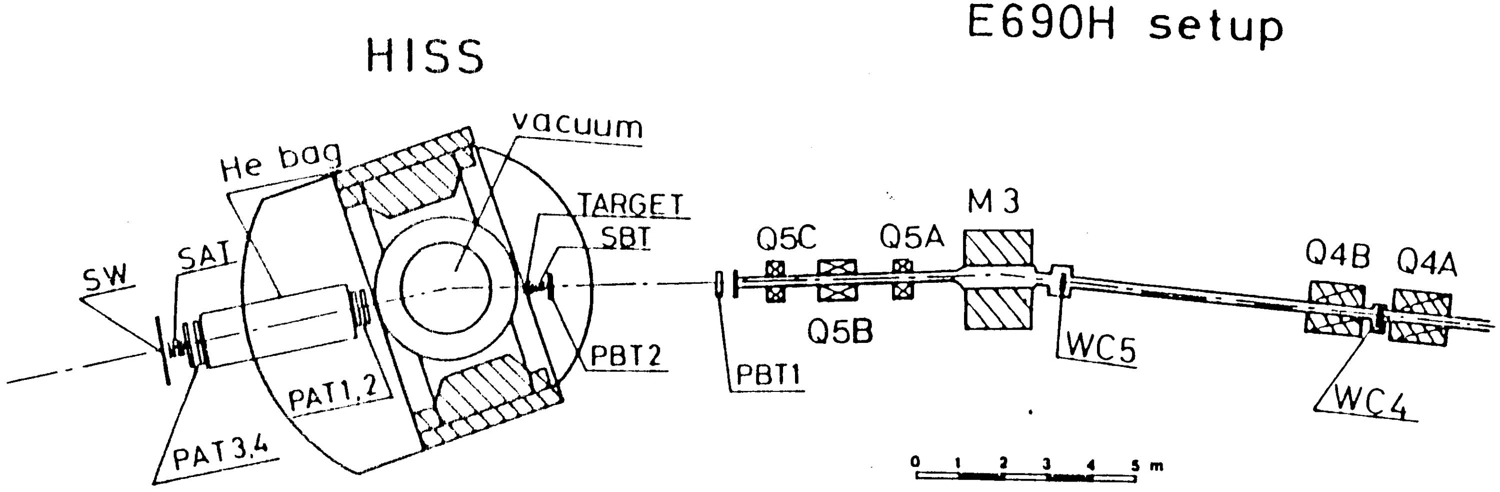

XBL 844-1421

Figure 16

chambers (PAT1 - PAT4: multi wire Proportional chambers After the reaction Target) and six plastic scintillation counters (SAT1 - SAT6: Scintillation counters After the reaction Target) were placed after the bending magnet (HISS).

After the reaction target, the trajectories were determined by the wire chambers PAT1, PAT2, PAT3, PAT4 to measure the bending angle by the HISS magnet. The pulse heights of SATs were also measured.

2.2.2.2. Targets

All targets were cylindrically shaped with a diameter of 7.62cm. The lengths is varid from 5 g/cm^2 to 20 g/cm^2. We used three different target materials (Be, C, Al) in order to see the mass dependence of the interaction cross sections and to verify the interaction radius separability. Two or three different thicknesses of the same target material were used to confirm the thickness independence of the interaction cross sections. The targets of different thicknesses were also used to examine and correct for intensity losses due to the scattering-out of non-interacting nuclei. For γ_0=1 and P_m =0, the statistical error for interaction cross sections is written as a function of attenuation factor

$$\frac{\Delta\sigma_I}{\sigma_I} = \frac{1}{\lfloor \ln\gamma \rfloor}\sqrt{\frac{1-\gamma}{N_{inc}\,\gamma}} \tag{2.6}$$

The error is affected not only by the counting statistics $\sqrt{N_{inc}}$ but also by the thickness of the target. Figure 17 shows the factor

$$\frac{1}{\lfloor \ln\gamma \rfloor}\sqrt{\frac{1-\gamma}{\gamma}} \tag{2.7}$$

depends on the attenuation factor γ. When the same number of incident nuclei are counted, the error is minimized for a target whose thickness is chosen such that γ=0.2. On the other hand, a thicker target causes a larger percentage of multiple Coulomb scattering which leads to a larger

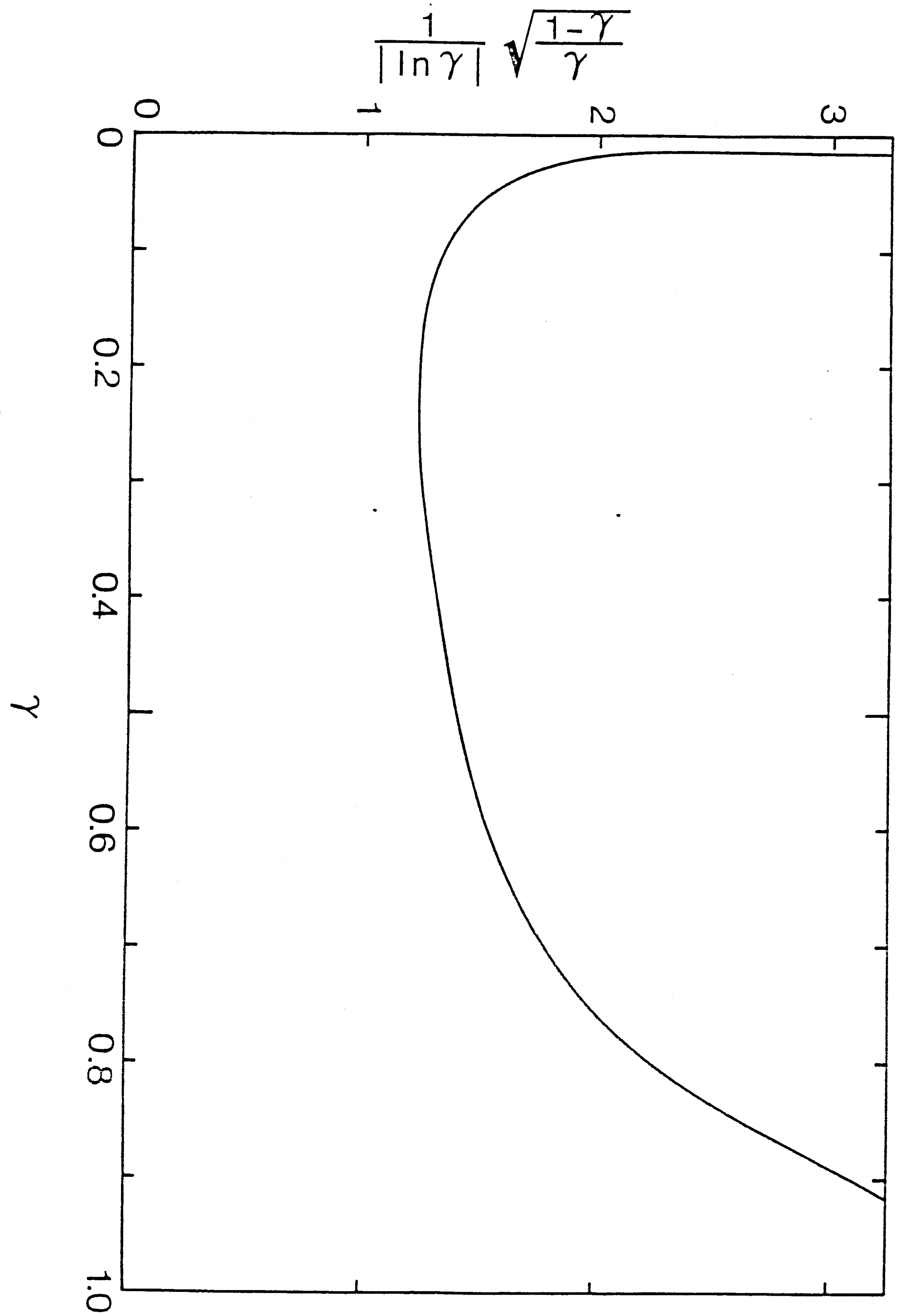
$\frac{1}{|\ln \gamma|}\sqrt{\frac{1-\gamma}{\gamma}}$
0
1
2
3
0
0.2
0.4
0.6
0.8
1.0
γ

Figure 17

uncertainties in P_m. The target thickness were chosen to keep the statistical error as low as possible under the condition that at least 99 percent of non-interacting nuclei could be detected by scintillation counters after the reaction target. The targets and their parameters are summarized in Table 2.

2.2.2.3. Scintillation counters

The charges (Z) of the nuclei was identified by the pulse heights in scintillation counters SBTs and SATs. The velocity of particles was also measured by the time difference between event in two scintillation counters SF3 and SBTs. Geometrical dimensions of the scintillation counters are listed in Table 3.

The SBTs consisted of four scintillation counters (SBT1, SBT2, SBT3, SBT4). Scintillation light in SBT1 and SBT3 was taken from the right-hand side of the scintillators. Scintillation light in SBT2 and SBT4 was taken from the left-hand side of the scintillators. The veto counter was used to define the maximum size of the incident beam and to reduce background triggers. Figure 18 shows a pulse height spectrum in SBT1. Clean charge separation can be seen in the spectrum. The inclusion of any other charges was less than 10^{-2} when charge was selected by one scintillation counter. The average time difference as measured with SBT1-SBT2 and with SBT3-SBT4 is shown in Fig. 19. The resolution in this time difference is 400 pico-second (FWHM).

The SATs consist of six scintillation counters (SAT1, SAT2, SAT3, SAT4, SAT5, SAT6). The signals were collected at both ends of each scintillator, thus the location independent pulse height of SATs could be obtained. Figure 18 shows the pulse height spectrum of SAT1. The inclusion of any other charges in a selected charge by one scintillation counter was less than 10^{-2} here, also.

Reaction target parameters						
Name	Z	A	t Thickness (g/cm^2)	$(t/L_R)^{1/2}$	attenuation(γ) for He isotopes	Note
Be1	4	9	8.864	0.37	0.61-0.71	99.46 % ^{9}Be 0.33 % ^{16}O in weight
Be2	4	9	18.255	0.53	0.38-0.53	99.46 % ^{9}Be 0.33 % ^{16}O in weight
C1	6	12	10.196	0.49	0.63-0.73	98.90 % ^{12}C 1.10 % ^{13}C in weight
C3	6	12	5.179	0.35	0.77-0.83	98.90 % ^{12}C 1.10 % ^{13}C in weight
Al1	13	27	6.739	0.53	0.79-0.85	
Al2	13	27	13.455	0.75	0.66-0.75	
Al3	13	27	20.197	0.92	0.55-0.67	

Diameter of all target are 7.62 cm

L_R is the radiation length of the matter.

Table 2

Plastic scintillation counters				
Name	X (mm)	Y (mm)	thickness (mm)	Location
SF3	30.0	30.0	3.0	at F3
SBTs (SBT1-SBT4)	50.0	70.0	3.0	before reaction target (4 scint.)
Veto (hole)	200.0 50.0	200.0 50.0	3.0	before reaction target
SATs (SAT1-SAT6)	400.0	300.0	3.0	after reaction target (6 scint.)

Table 3

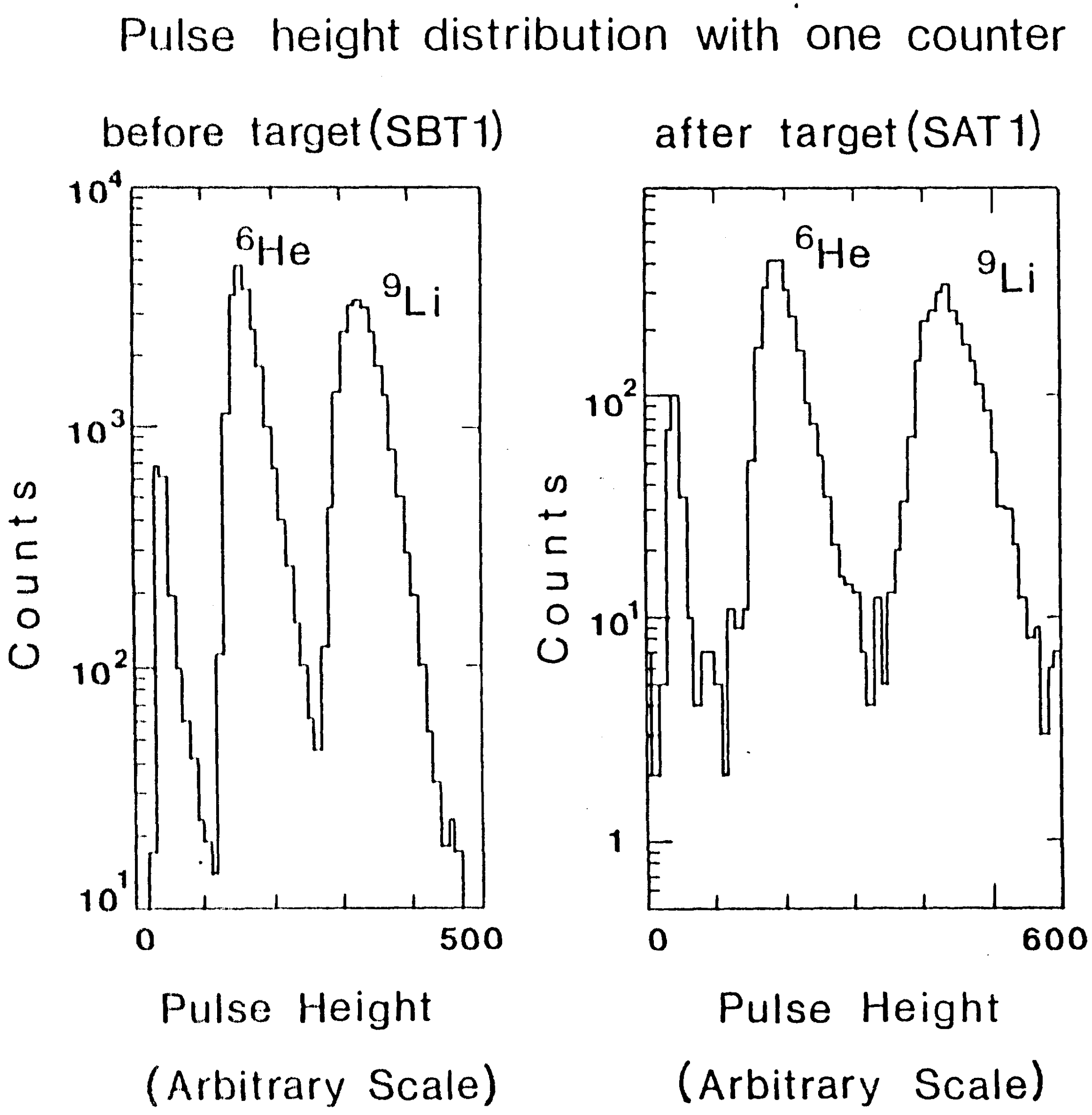
Pulse height distribution with one counter
before target (SBT1)
after target (SAT1)
Counts
Counts
10^4
10^3
10^2
10^1
10^2
10^1
1
^{6}He
^{9}Li
^{6}He
^{9}Li
0
500
0
600
Pulse Height
(Arbitrary Scale)
Pulse Height
(Arbitrary Scale)

Figure 18

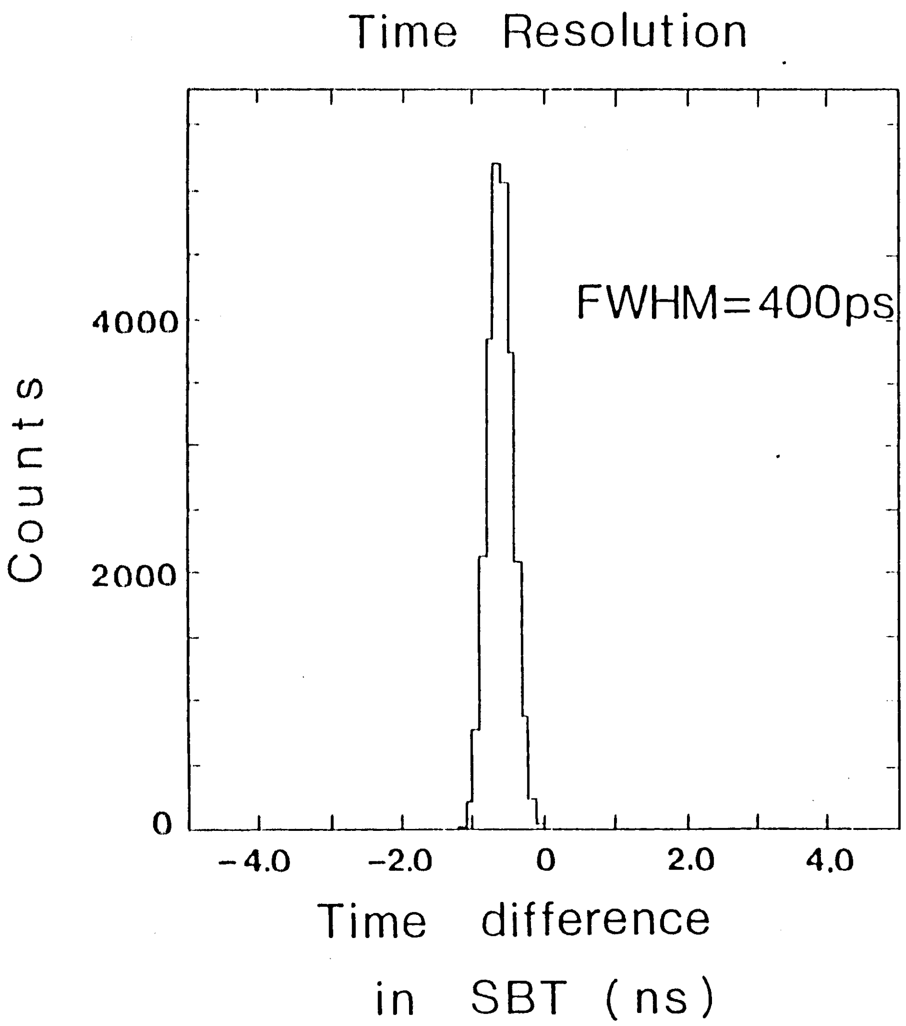
Time Resolution
FWHM=400ps
Counts
0
2000
4000
-4.0
-2.0
0
2.0
4.0
Time difference in SBT (ns)

Figure 19

2.2.2.4. Multi-wire proportional chambers and the bending magnet HISS

Thirteen planes of multi-wire proportional chambers (MWPCs) were used to determine the trajectory and to select the rigidity of the nucleus with the HISS spectrometer magnet. The definition of coordinates is given in Fig. 16. Geometrical dimensions of MWPCs are listed in Table 4.

The incoming angle of the nucleus was determined by two planes of PBT1(X,Y) and three planes of PBT2(X,Y,V) and the outgoing angle was measured by one plane of PAT1(X), three planes of PAT2(X,Y,U), two planes of PAT3(X,U) ,and two planes of PAT4(X,V). The definitions of X,Y,U,V planes are shown in Fig. 16. The bending angle resolution determined by these MWPCs and HISS magnet was 3.0 mrad (FWHM) as shown in Fig. 20. On the average, the nuclei were bent through an angle of 11 degree after the reaction target, rigidity resolusion of the system was thus 1.6 percent (FWHM). We used MWPCs redundantly after the reaction target to obtained good MWPC system efficiency. As a result of this redundancy the tracking efficiency of the MWPC system after the reaction target was greater than 99.0 percent.

The HISS spectrometer magnet has a pole gap of 1 m and a pole diameter of 2 m. In order to reduce the multiple Coulomb scattering and background reactions, a vacuum was maintained in the gap volume. This resulted in a reduction to 10.6 percent by weight of the amount of material from the reaction target to the exit window of HISS.

2.2.2.5. The helium bag

A helium bag was placed after the vacuum chamber to further reduce the amount of material. It had a columnar shape 3 m in length and 60 cm in diameter. The amount of material from the exit window of HISS to SAT was reduced to 20.8 percent in weight by the addition of using the helium bag. The amount of material in the beam line before and after SBTs are listed in Table 5 and Table 6 respectively.

Multi wire proportional chambers				
Name	Active area (mm)	Wire spacing (mm)	Number of wires	Location
PBT1X PBT1Y	128.0 128.0	2.0 2.0	64 64	before reaction target
PBT2X PBT2Y	128.0 128.0	2.0 2.0	64 64	before reaction target
PAT1X	384.0	3.0	128	after reaction target
PAT2X PAT2Y PAT2U	384.0 336.0 480.0	3.0 3.0 3.0	128 112 160	after reaction target
PAT3X PAT3U	528.0 672.0	3.0 6.0	176 112	after reaction target
PAT4X PAT4V	528.0 672.0	3.0 6.0	176 112	after reaction target

Table 4

Amount of material in the beam line before reaction target			
Name	Material	Thickness (g/cm^2)	Note
PBT1 (X,Y)	Mylar ($C_5H_8O_2$)	0.0278	window, 100 μm
	Argon (Ar)	0.0089	gas, 5 cm
	Copper (Cu)	0.0076	H.V. wire, 60 μm ϕ
	Tungsten (W)	0.0006	sense wire, 20 μm ϕ
PBT2 (X,Y)	Mylar ($C_5H_8O_2$)	0.0278	window, 100 μm
	Argon (Ar)	0.0089	gas, 5 cm
	Copper (Cu)	0.0076	H.V. wire, 60 μm ϕ
	Tungsten (W)	0.0006	sense wire, 20 μm ϕ
PBT2 (V)	Mylar ($C_5H_8O_2$)	0.0278	window, 100 μm
	Argon (Ar)	0.0053	gas, 3 cm
	Copper (Cu)	0.0051	H.V. wire, 60 μm ϕ
	Tungsten (W)	0.0006	sense wire, 20 μm ϕ
SF3	Scintillator	0.3096	plastic, 3 mm
	Aluminum (Al)	0.0346	cover, 64 μm
SBT1	Scintillator	0.3096	plastic, 3 mm
	Aluminum (Al)	0.0346	cover, 64 μm
SBT2	Scintillator	0.3096	plastic, 3 mm
	Aluminum (Al)	0.0346	cover, 64 μm
SBT3	Scintillator	0.3096	plastic, 3 mm
	Aluminum (Al)	0.0346	cover, 64 μm
SBT4	Scintillator	0.3096	plastic, 3 mm
	Aluminum (Al)	0.0346	cover, 64 μm
Veto	Aluminum (Al)	0.0346	cover, 64 μm
Air	Air	0.6025	total 5 m air gap before reaction target
Total		2.4867	total amount before reaction target

Table 5

Amount of material in the beam line after reaction target			
Name	Material	Thickness (g/cm^2)	Note
PAT1 (X)	Mylar ($C_5H_8O_2$)	0.0278	window, 100 μm
	Argon (Ar)	0.0107	gas, 6 cm
	Copper (Cu)	0.0101	H.V. wire, 60 μm ϕ
	Tungsten (W)	0.0006	sense wire, 20 μm ϕ
PAT2 (X,Y,U)	Mylar ($C_5H_8O_2$)	0.0278	window, 100 μm
	Argon (Ar)	0.0107	gas, 6 cm
	Copper (Cu)	0.0101	H.V. wire, 60 μm ϕ
	Tungsten (W)	0.0006	sense wire, 20 μm ϕ
PAT3 (X,U)	Mylar ($C_5H_8O_2$)	0.0278	window, 100 μm
	Argon (Ar)	0.0089	gas, 5 cm
	Copper (Cu)	0.0076	H.V. wire, 60 μm ϕ
	Tungsten (W)	0.0006	sense wire, 20 μm ϕ
PAT4 (X,V)	Mylar ($C_5H_8O_2$)	0.0278	window, 100 μm
	Argon (Ar)	0.0089	gas, 5 cm
	Copper (Cu)	0.0076	H.V. wire, 60 μm ϕ
	Tungsten (W)	0.0006	sense wire, 20 μm ϕ
SAT1	Scintillator	0.3096	plastic, 3 mm
	Aluminum (Al)	0.0346	cover, 64 μm
SAT2	Scintillator	0.3096	plastic, 3 mm
	Aluminum (Al)	0.0346	cover, 64 μm
SAT3	Scintillator	0.3096	plastic, 3 mm
	Aluminum (Al)	0.0346	cover, 64 μm
SAT4	Scintillator	0.3096	plastic, 3 mm
	Aluminum (Al)	0.0346	cover, 64 μm
SAT5	Scintillator	0.3096	plastic, 3 mm
	Aluminum (Al)	0.0346	cover, 64 μm
SAT6	Scintillator	0.3096	plastic, 3 mm
	Aluminum (Al)	0.0346	cover, 64 μm
HISS	Capton	0.017	window, up stream
	Capton	0.034	window, down stream
He bag	Alminyaed mylar	0.0010	window, up and down stream
	Helium (He)	0.0534	3 m
Air	Air	0.0844	70 cm air gap from target to SAT6
Total		2.4432	total amount after reaction target

Table 6

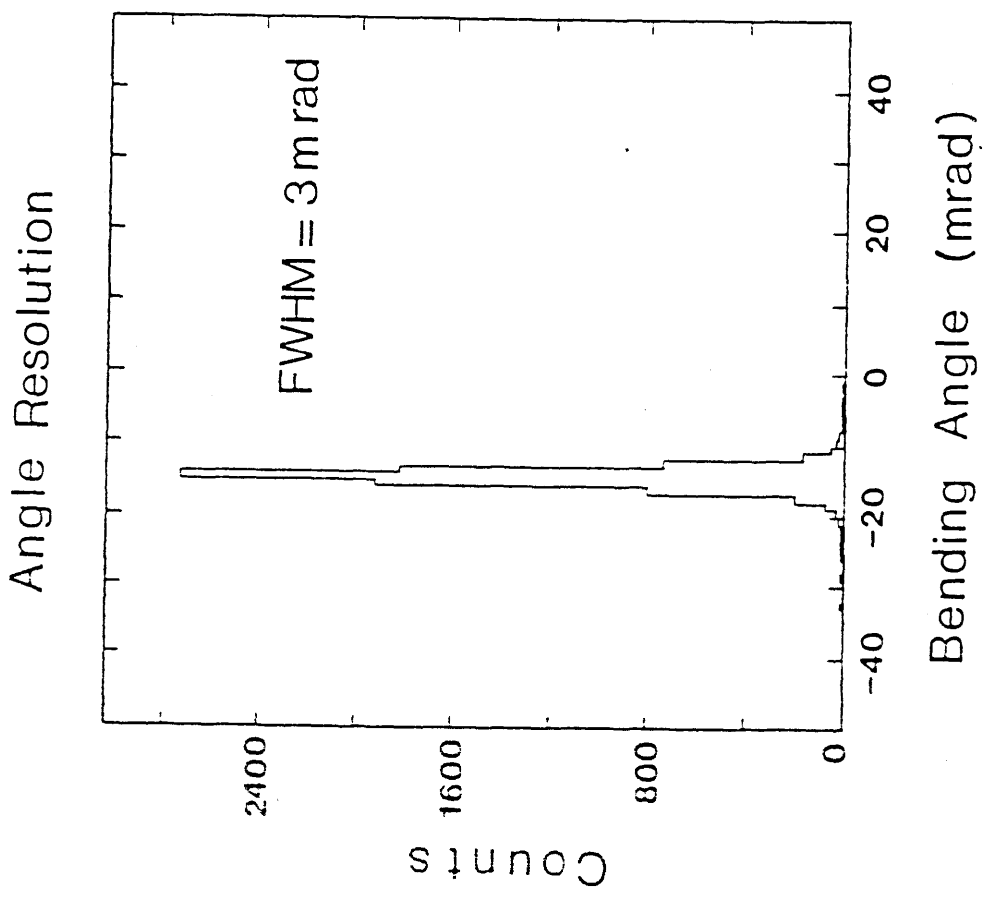
Angle Resolution
FWHM = 3 mrad
Bending Angle (mrad)
Counts
-40
-20
0
20
40
0
800
1600
2400

Figure 20

2.2.3. The electronics and the data acquisition system

2.2.3.1. The trigger system

The circuit diagram of the trigger system is shown in Fig. 21. The main trigger was

$$Trig = SF\,3 * (SBT\,1 * SBT\,2 * SBT\,3 * SBT\,4) * \overline{Veto} \tag{2.8}$$

where '*' means logical AND.

In this experiment, we used window discriminators, which allow lower and upper limits on the pulse heights, to select the proper charge. The timing of the trigger was determined by SBT1. Typical event rates per beam pulse for each counter are listed in Table 1.

2.2.3.2. The on-line data acquisition system

The on-line data acquisition system is schematically shown in Fig. 22. Using this system, we recorded all pulse heights in the ADCs and all timing information in the TDCs. We also logged the hit patterns of all MWPCs and the contents of all scalers. The beam-on period was about 1 second and the beam-off period was about 4 seconds.

The stream of data taking was as follows: The MBD(Micro programmed Branch Driver) was started by a "beam-on" interrupt signal from Bevalac and waited for an event trigger signal. After the event trigger signal was accepted by the MBD, it started to read the registers, the ADCs, the TDCs and data concerning the hit positions of the MWPCs through a CAMAC crate. The data were subsequently transfered to a memory module(256K words) in the CAMAC crate. This procedure was repeated during the beam-on period to accumulate the data. When the beam-off signal from the Bevalac was accepted, the MBD read back the data from the memory module, then recorded the data onto a hard disk connected to the PDP 11/44 computer, which then recorded all the data onto the magnetic tape. On-line data analysis was performed during the beam-off period. Histograms and scatter plots of any combination of the data

The circuit diagram of trigger system

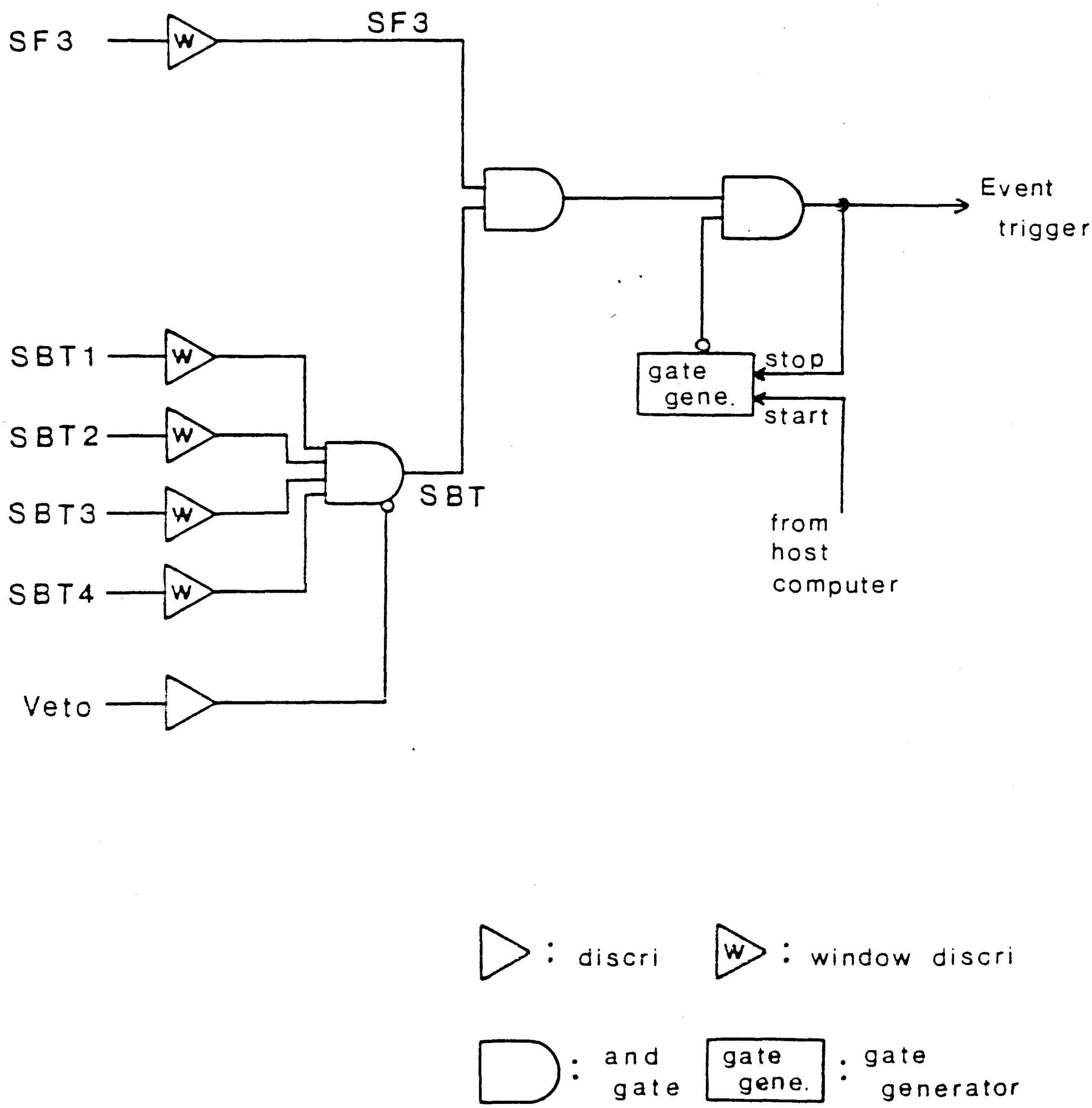

Figure 21

Schematic diagram for data taking system

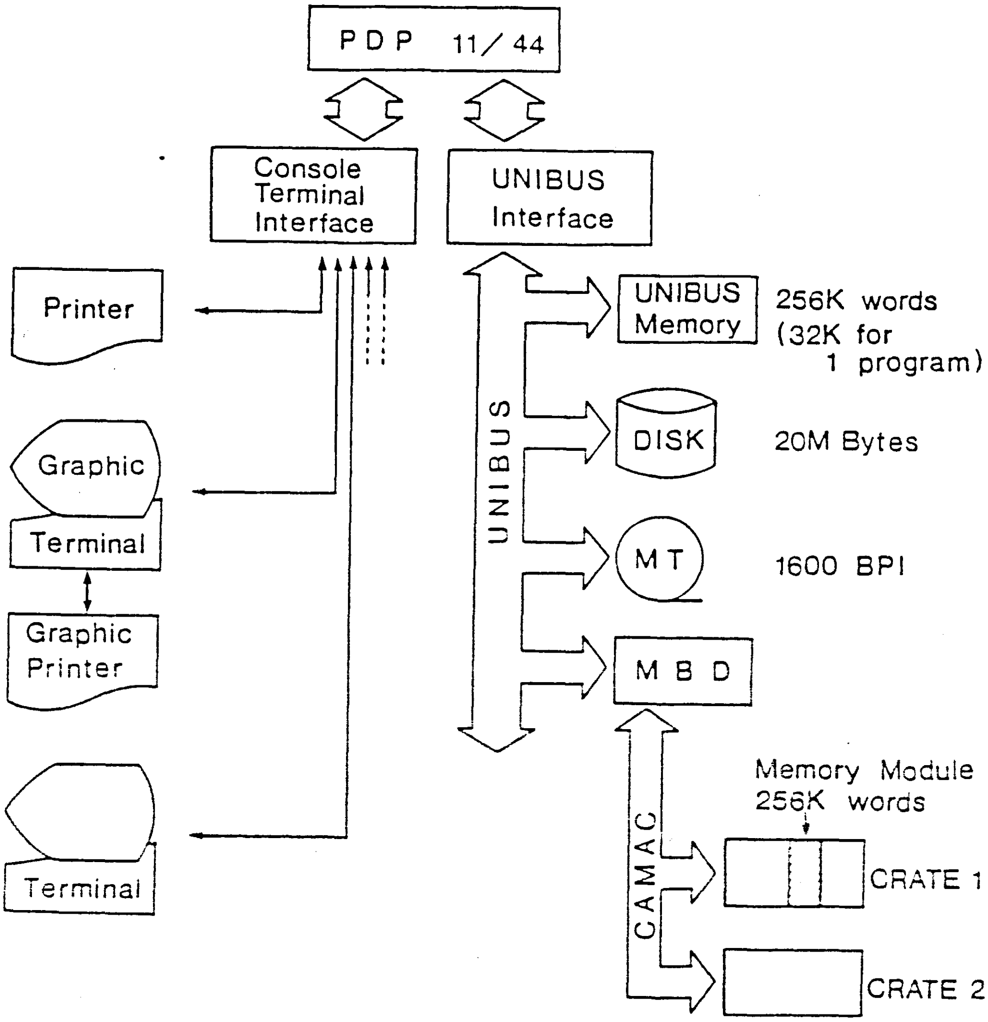

Figure 22

could be displayed to monitor the experimental system.

3. Data analysis

3.1. Procedure of data analysis

Data analysis was done using VAX 11/780 of the HISS group at the Bevalac.

First, we counted the number of incoming nuclei (N_{inc}) after identifying each nucleus. The selection criteria were so stringent that the inclusion of other nuclear species in the incident beam was negligible. We then counted the number of non-interacting nuclei (N_{out}) among the incident species of nuclei after identifying each nucleus again. Details of the selection are described below.

3.1.1. Identification of incident nuclei

The incoming nuclei were identified as follows:

(1) The TOF between SF3 and SBTs was in a proper range.

(2) The pulse heights of all four SBTs were in a proper range.

(3) Only one track was observed by PBTs before the reaction target.

A typical pulse height and the TOF spectra are shown in Fig. 9. The inclusion of other atomic number nuclei is less than 10^{-2} by using one scintillation counter for the identification. The inclusion was negligibly small when all four scintillation counters before the reaction target were used. The number of incoming nuclei (N_{inc}) was obtained by counting the nuclei which satisfy the above conditions.

3.1.2. Identification of non-interacting nuclei

After the reaction target, all nuclei which hit the SATs were identified. In order to select the non-interacting nuclei, the following criteria were used.

(1) The nuclei detected after the reaction target were required to have the same charge as those detected before the reaction target.

Figure 23 shows the pulse height distribution of one of the SATs for charges of 2 or 3 as selected by using the SBT. The inclusion is about 1.0×10^{-2} for each SAT. Using the six sintillation counters after the reaction target, the charge was determined by two independent methods. The first method was to take the majority of the six charges identified by individual SAT. The other method was to take the average of the SATs pulse heights, the charge was then determined from them. These two method was found to give the same charge except negligible number of cases.

Even with the charge separation, other isotopes which were produced in the reaction target were still mixed in the proper rigidity range.

(2) The rigidity for the nucleus obtained by MWPCs and HISS magnet after the reaction target is in a proper range.

The mass of nucleus can be separated by sorting the beam according to their rigidity after the reaction target. Typically the momentum spread due to the production reactions in the reaction target is at most a few percent. For light nuclei ($A < 10$), therefore, there is no rigidity overlap between neighboring isotopes.

Figure 24(a) shows a scatter plot between spectrometer exit angle and the position for the outgoing nuclei at PAT1,2 with an incident beam of ^{6}He. A clear separation between ^{4}He, which is produced in the target, and ^{6}He is seen. Figures 24 and 25 show the rigidity distribution for He and Li isotopes after the reaction target. All histograms show clear separation between beam nuclei and the other isotopes.

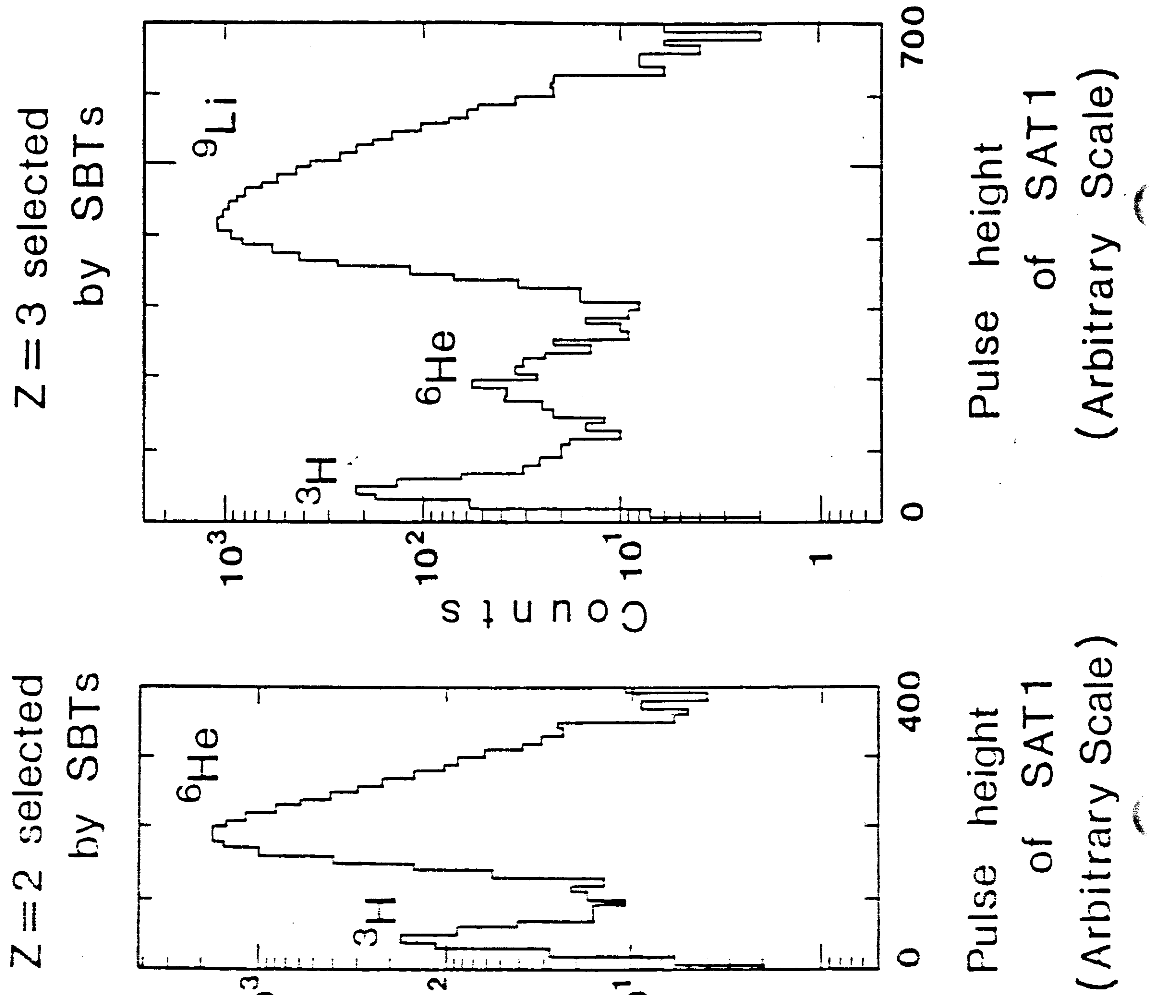
Z = 2 selected by SBTs
Z = 3 selected by SBTs
^{6}He
^{3}H
^{9}Li
Counts
10^3
10^2
10^1
1
0
400
700
Pulse height of SAT1 (Arbitrary Scale)

Figure 23

Rigidity separation of He isotopes

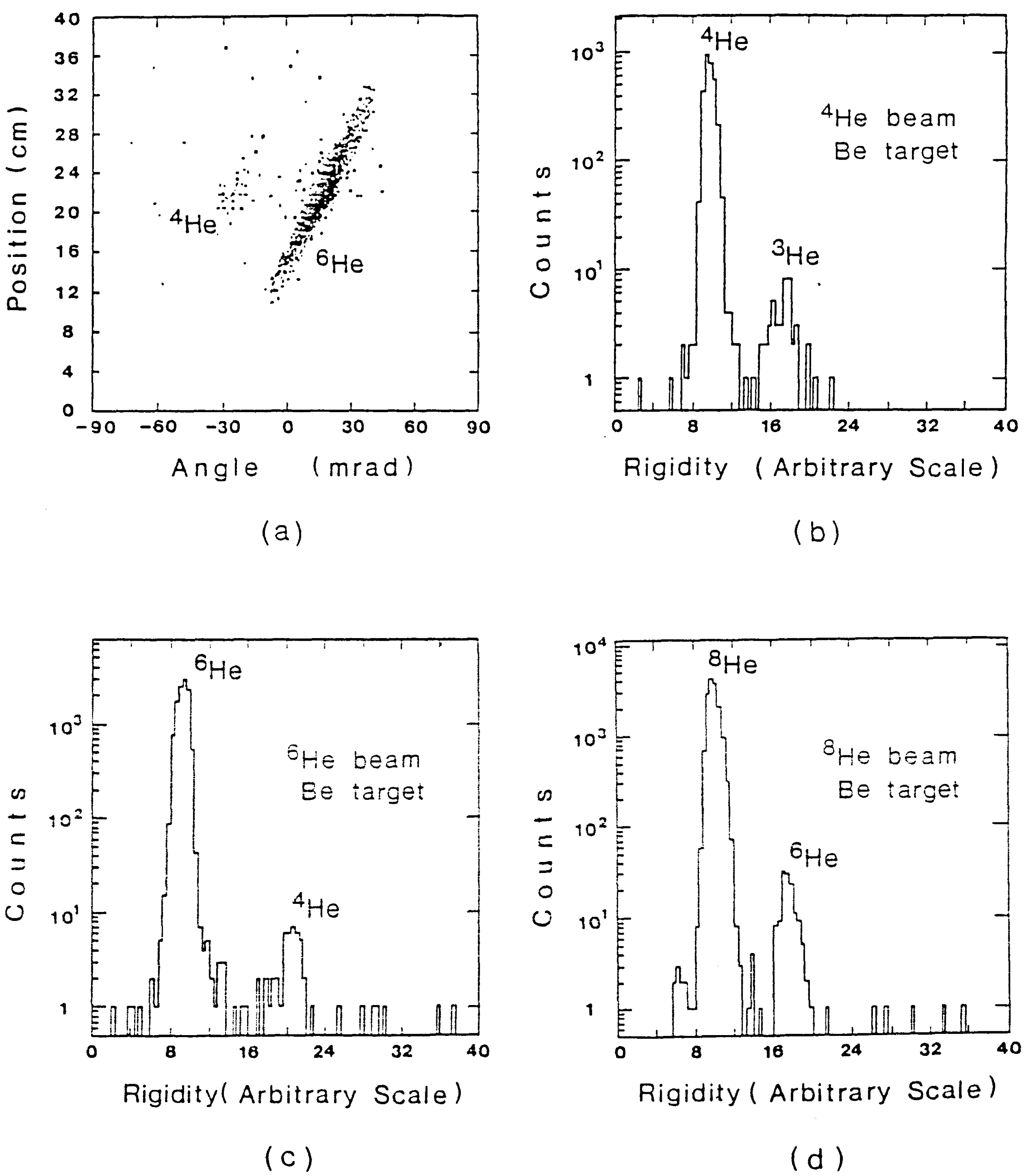

Figure 24

Rigidity separation of Li isotopes

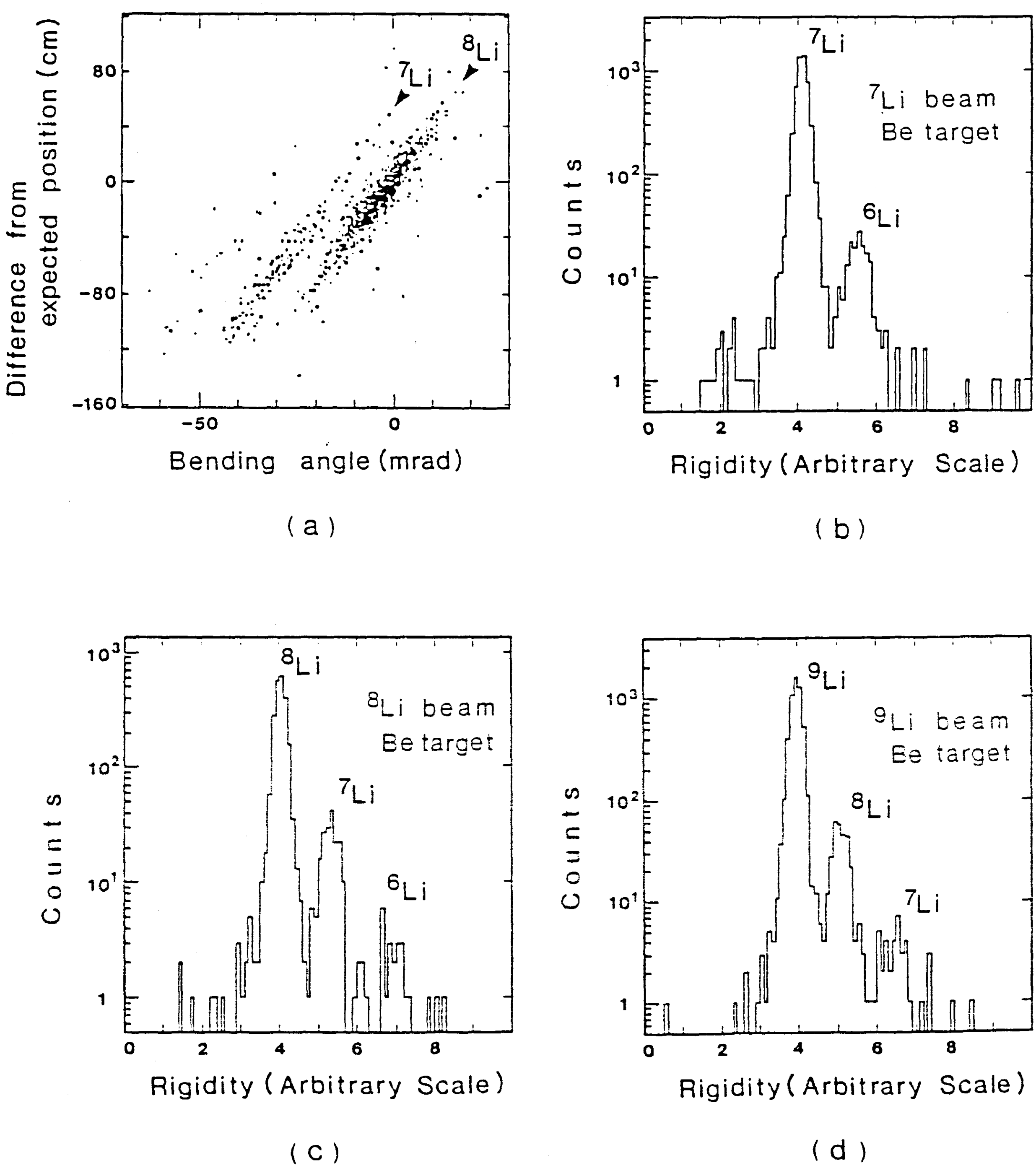

Figure 25

We obtaine the number of non-interacting nuclei (N_{out}) as

$$N_{out} = N_c \frac{N_{wrig}}{N_{wtot}} \tag{3,1}$$

where N_c is the number of nuclei identified as having the same charge as the incident nuclei by the SATs, N_{wrig} is the number of nuclei identified to be in a proper rigidity range by the PATs, and N_{wtot} is the total number of nuclei traced by PATs. The ratio N_{wrig}/N_{wtot} was always at least 0.98. The uncertainty of the factor N_{wrig}/N_{wtot} was less than 1.9×10^{-5} for He isotopes and 2.3×10^{-4} for Li isotopes.

3.1.3. Corrections for the scattering-out of non-interacting nuclei

A small number of non-interacting nuclei were not detected by SATs due to the large-angle scattering. Figure 26 and Figure 27 show the beam profiles at PAT3,4 for a target-out run and a target-in run, respectively. These profiles can be fitted by a Gaussian distribution (for the central part) and an exponential distribution (for the tail part). The number of non-interacting nuclei which escaped was estimated by the following procedure.

(1) The central part of beam profile at PAT3,4 was fitted by Gaussian as

$$G(x,y) = \exp\left[-\left(\frac{x^2}{2S_x^{\,2}} + \frac{y^2}{2S_x^{\,2}}\right)\right] \tag{3.2}$$

and the standard deviations (S_{xout}, S_{yout}) of this Gaussian distribution were obtained for a target-out run. (see Fig. 26).

(2) This procedure was repeated to obtain (S_{xin}, S_{yin}) for a corresponding target-in run. (see Fig. 27)

(3) We assumed the beam profile for the target-out run as a mother distribution $M(x,y)$, which included an exponential part of the beam profile.

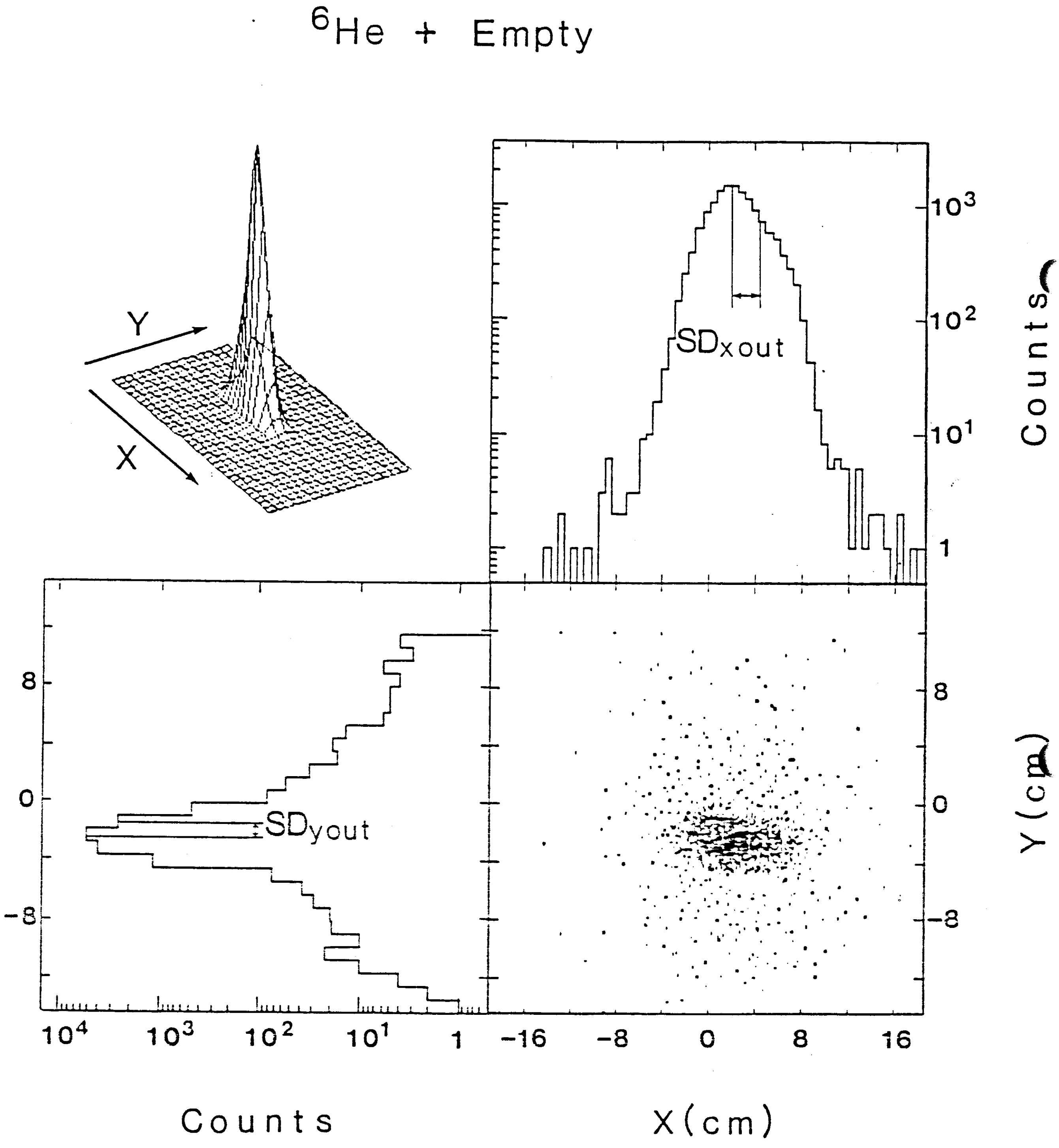

^{6}He + Empty
Y
X
SDxout
Counts
10^3
10^2
10^1
1
SDyout
8
0
-8
10^4
10^3
10^2
10^1
1
-16
-8
0
8
16
Counts
X(cm)
Y(cm)

Figure 26

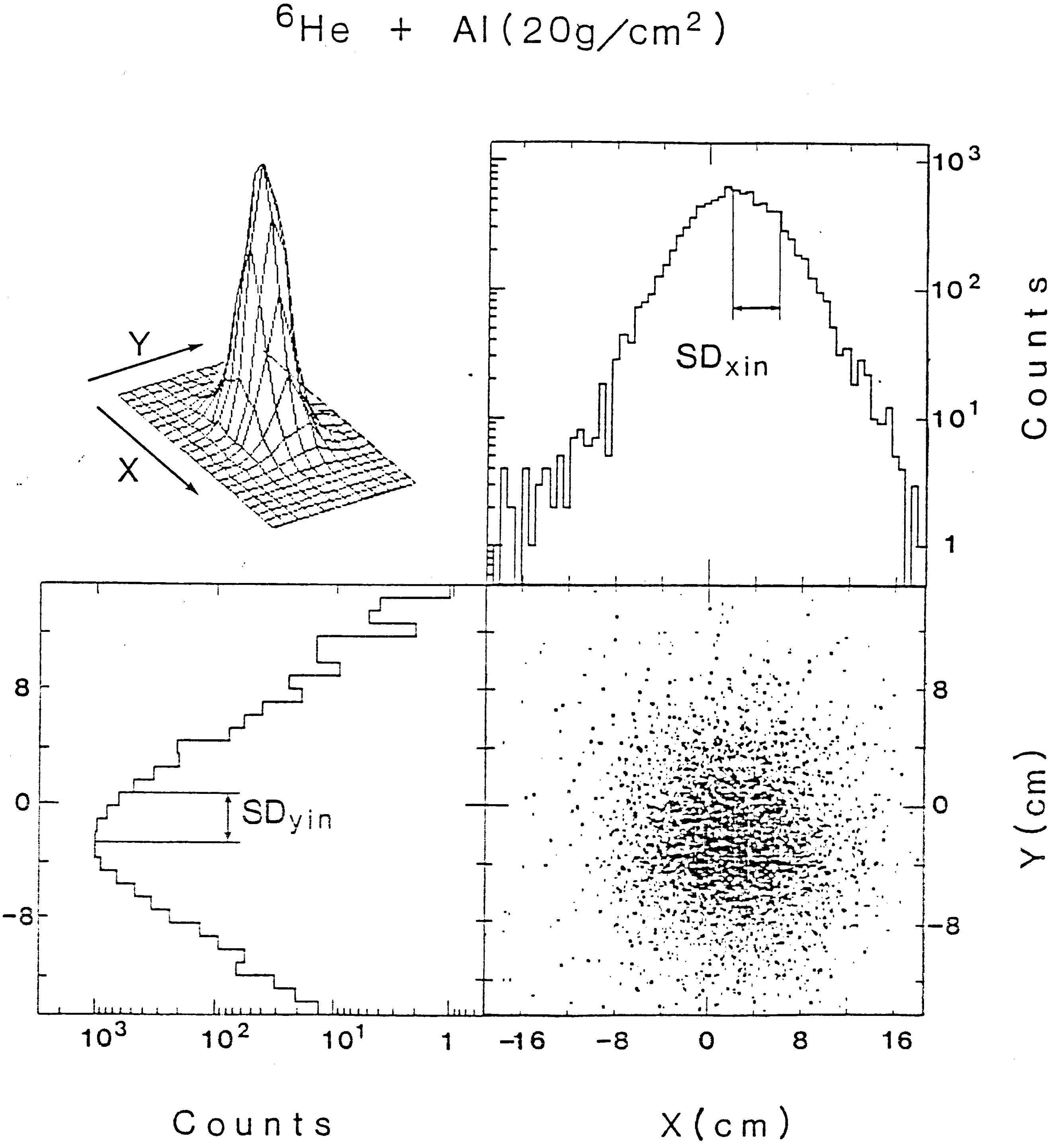
^{6}He + Al(20g/cm^2)
Y
X
SD$_{xin}$
SD$_{yin}$
Counts
Y(cm)
X(cm)
Counts
10^3
10^2
10^1
1
-16
-8
0
8
16

Figure 27

(4) The number of escaped nuclei N_{esc} was then calculated from the beam profile for the target-in run which was assumed by expanding the mother distribution as

$$M(x,y) \rightarrow M\left(x\frac{S_{outx}}{S_{inx}}, y\frac{S_{outy}}{S_{iny}} \right) \tag{3.3}$$

The scattering-out probability (P_m) was then determined as

$$P_m = \frac{N_{esc}}{N_{mt}} \tag{3.4}$$

where N_{mt} is the total number of nuclei in the mother distribution $M(x,y)$. Then the factor P_m was used in Eq. (2.3) for the correction.

Figures 28 - 35 show the scattering-out probability (P_m) thus obtained for He and Li isotope. The dushed line shows a fitting function

$$F\left(\frac{t}{L_R}\right) = \exp\left(-a\sqrt{\frac{L_R}{t}} + b\right) \tag{3.5}$$

which was expected from the model (gaussian + exponential tail) for the beam profile at SAT. Here a and b are the fitting parameters for the function, t is the thickness of the reaction target, and L_R is the radiation length of the target material. The cut-off values of the mother distribution are proportional to the factor $\sqrt{L_R/t}$ when multiple-Coulomb scattering is dominant. A good fitting of this functional shape suggest that the scattering out is mainly due to the multiple-Coulomb scattering. The uncertainties of P_m, which are quoted in Figures 28 - 35, were estimated to be the standard deviations of the factor P_m as obtained from that of the fitting function $F(t/L_R)$.

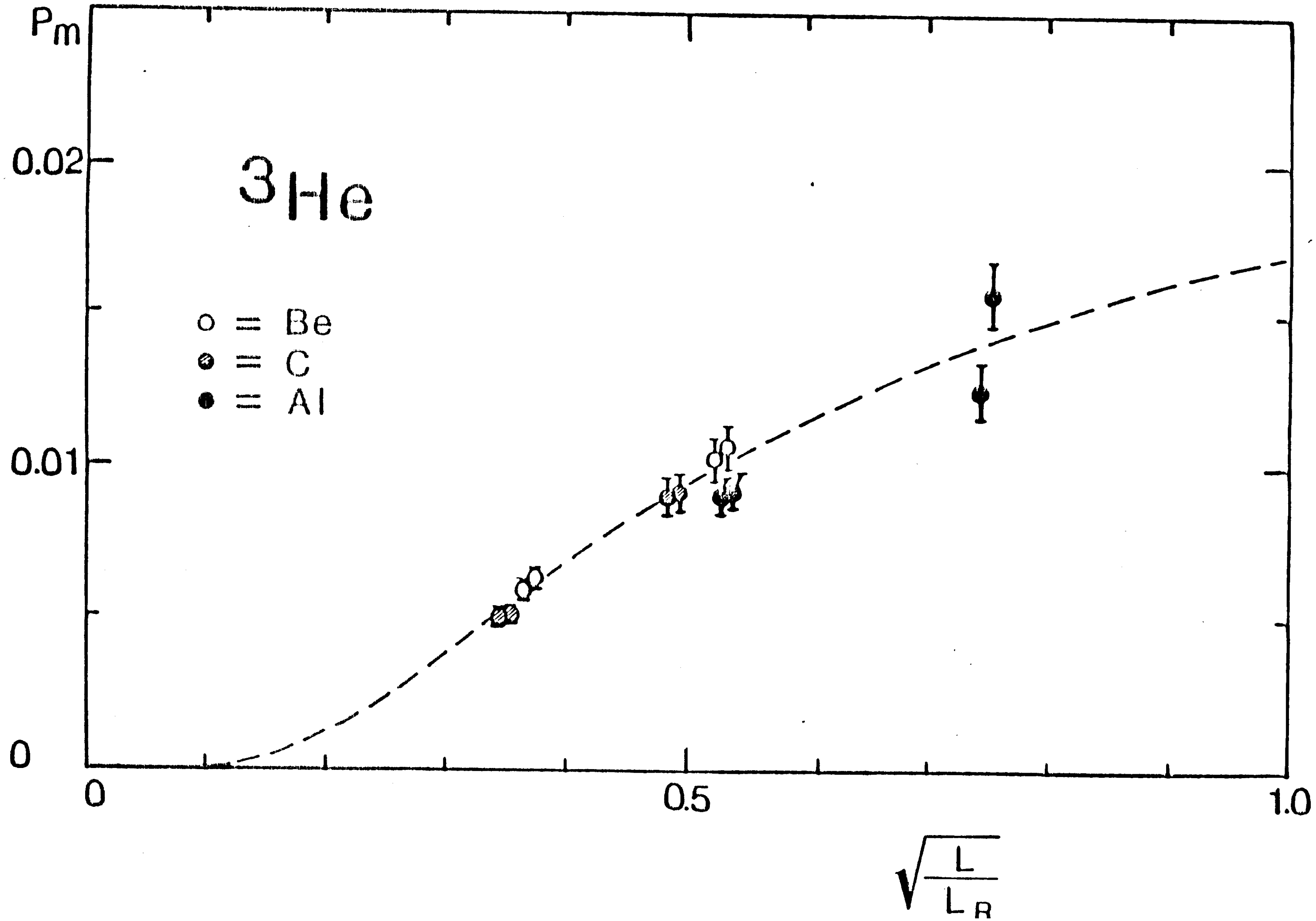

Figure 28

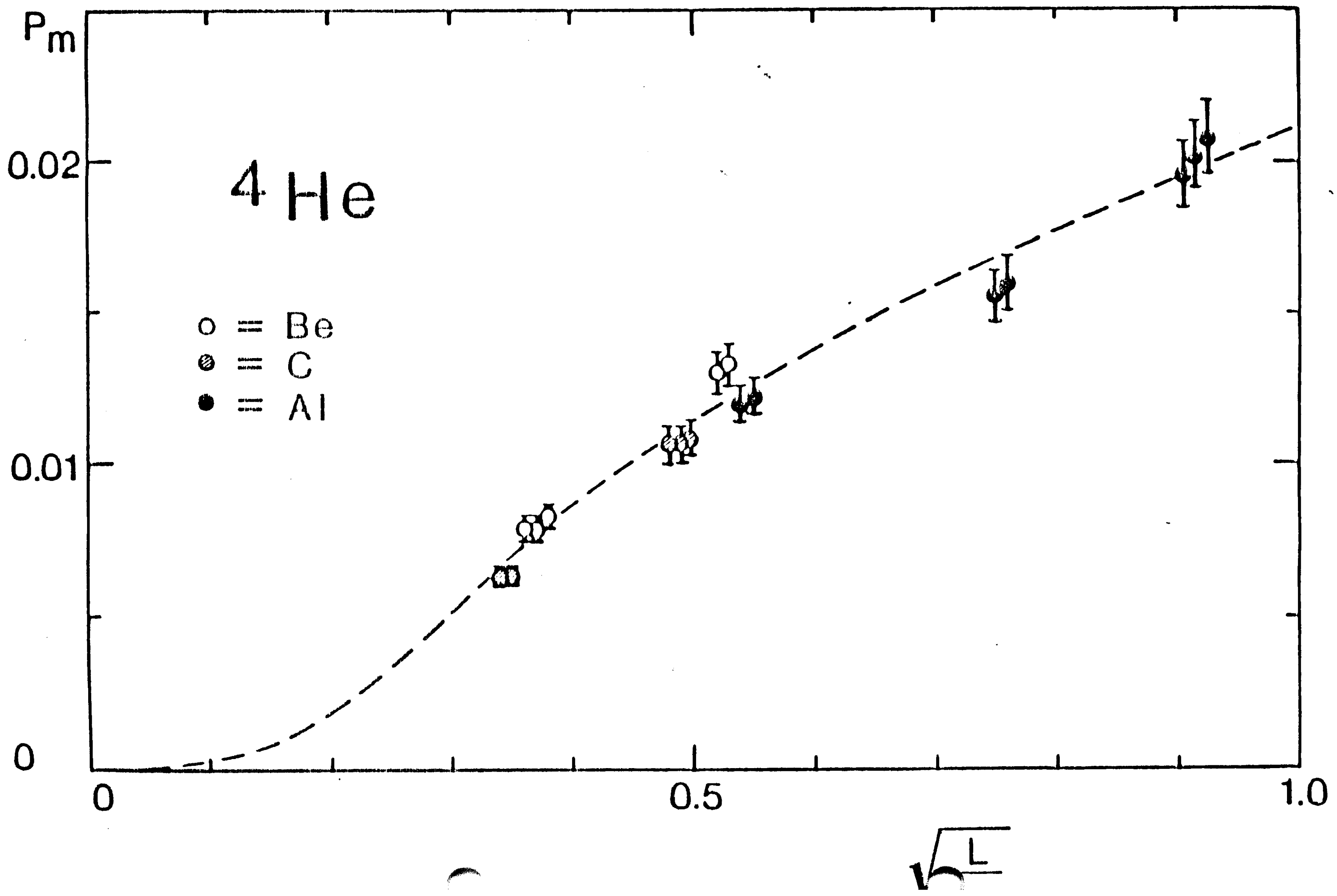

Figure 29

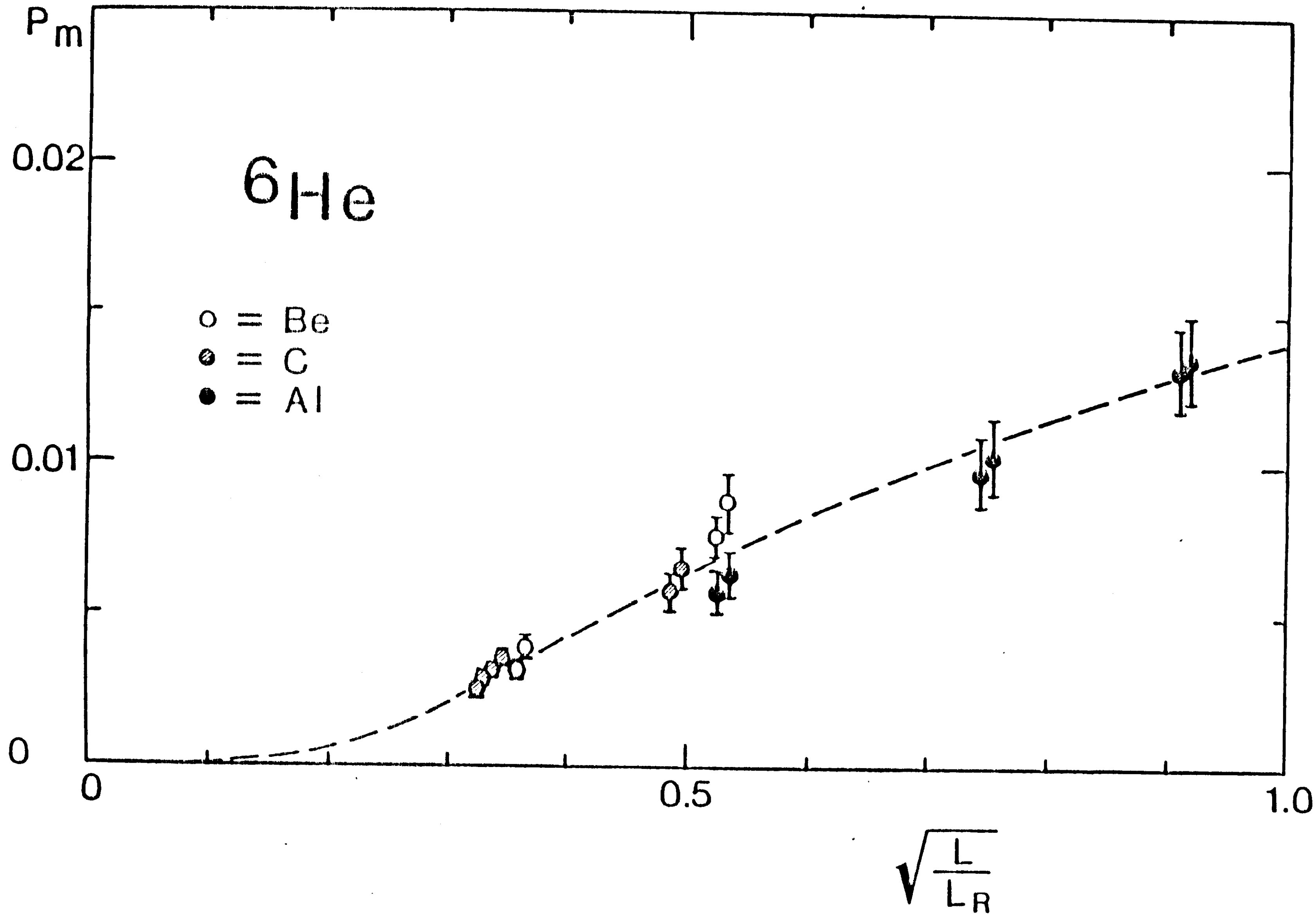

Figure 30

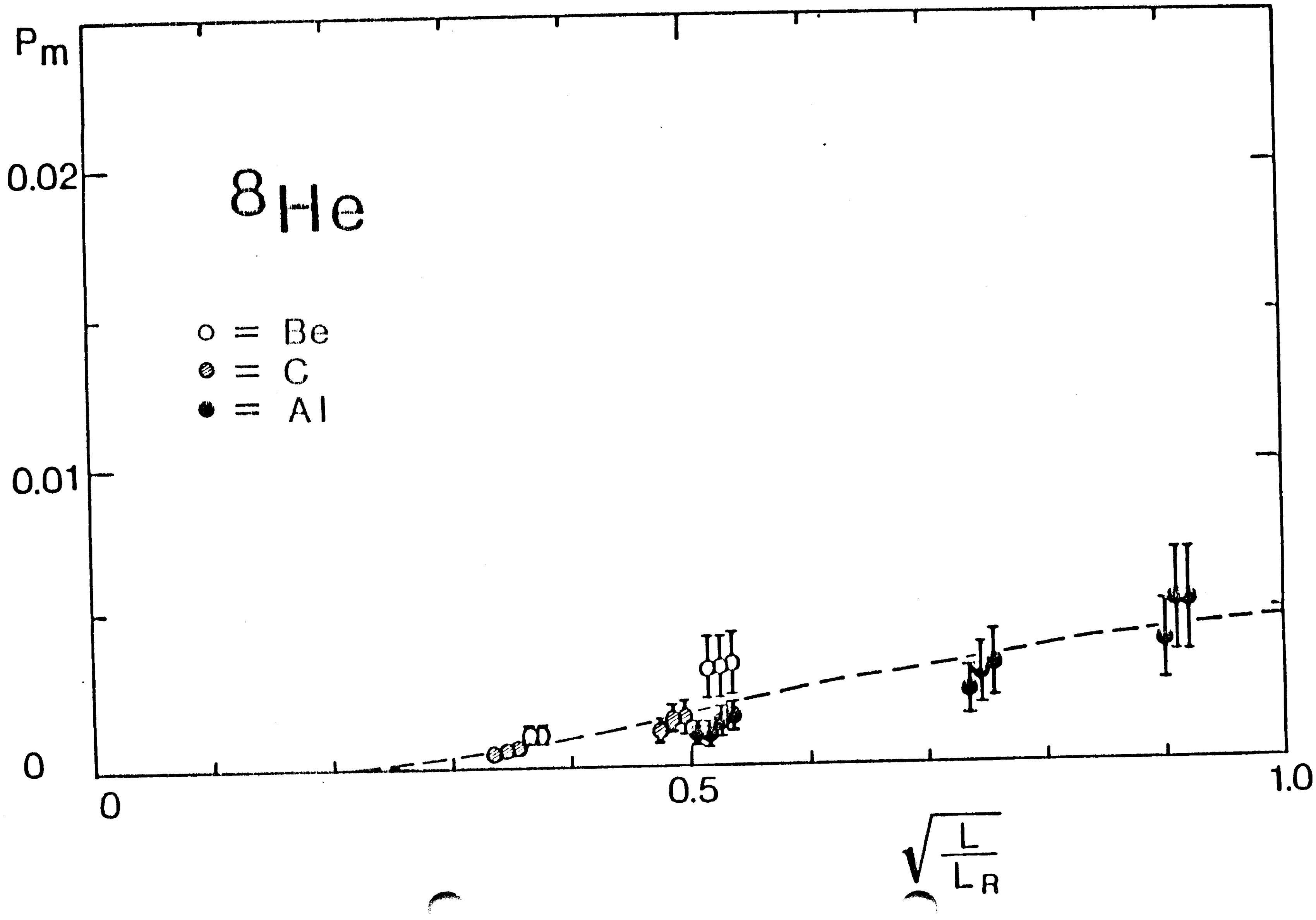

Figure 31

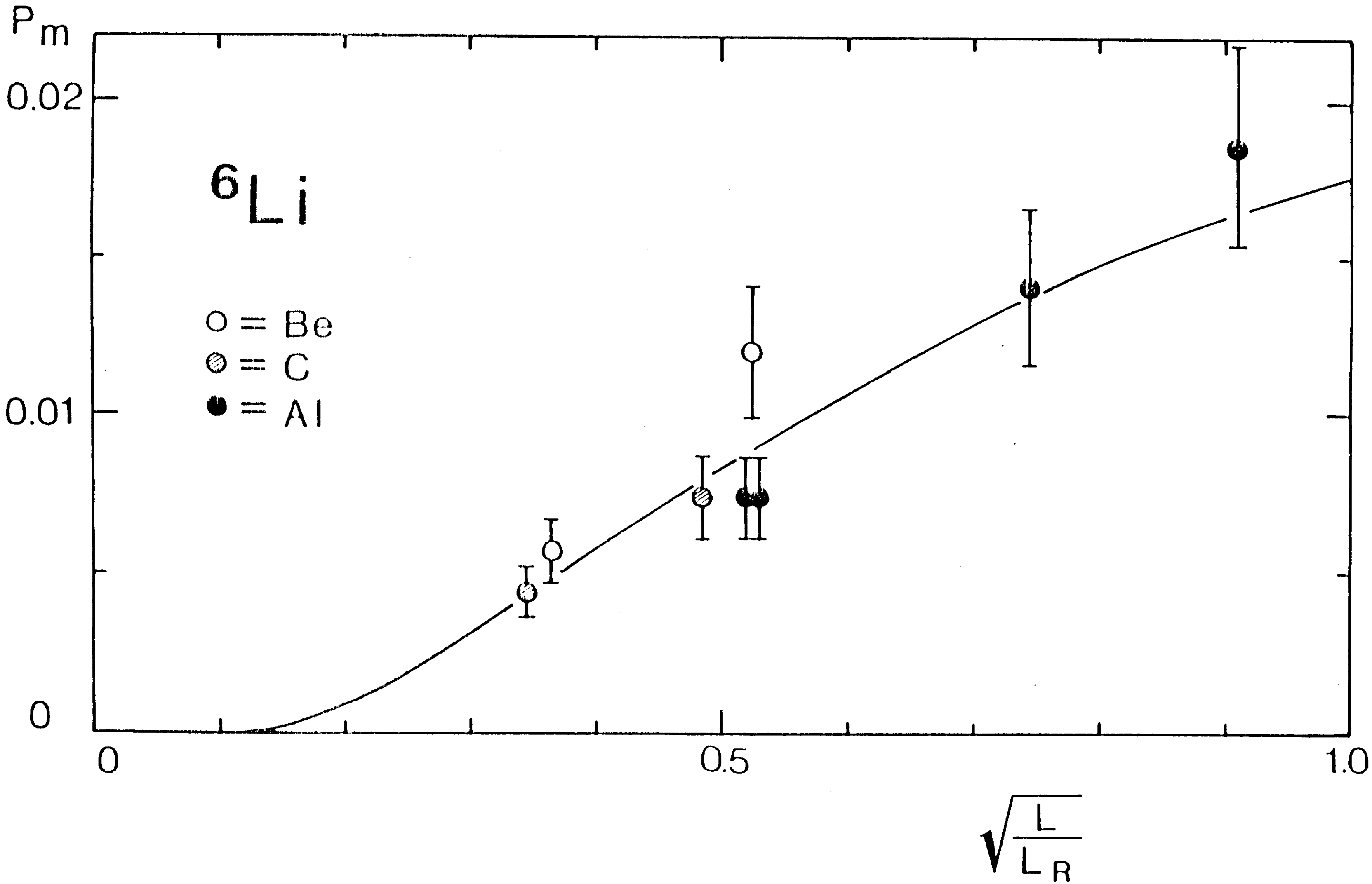

Figure 32

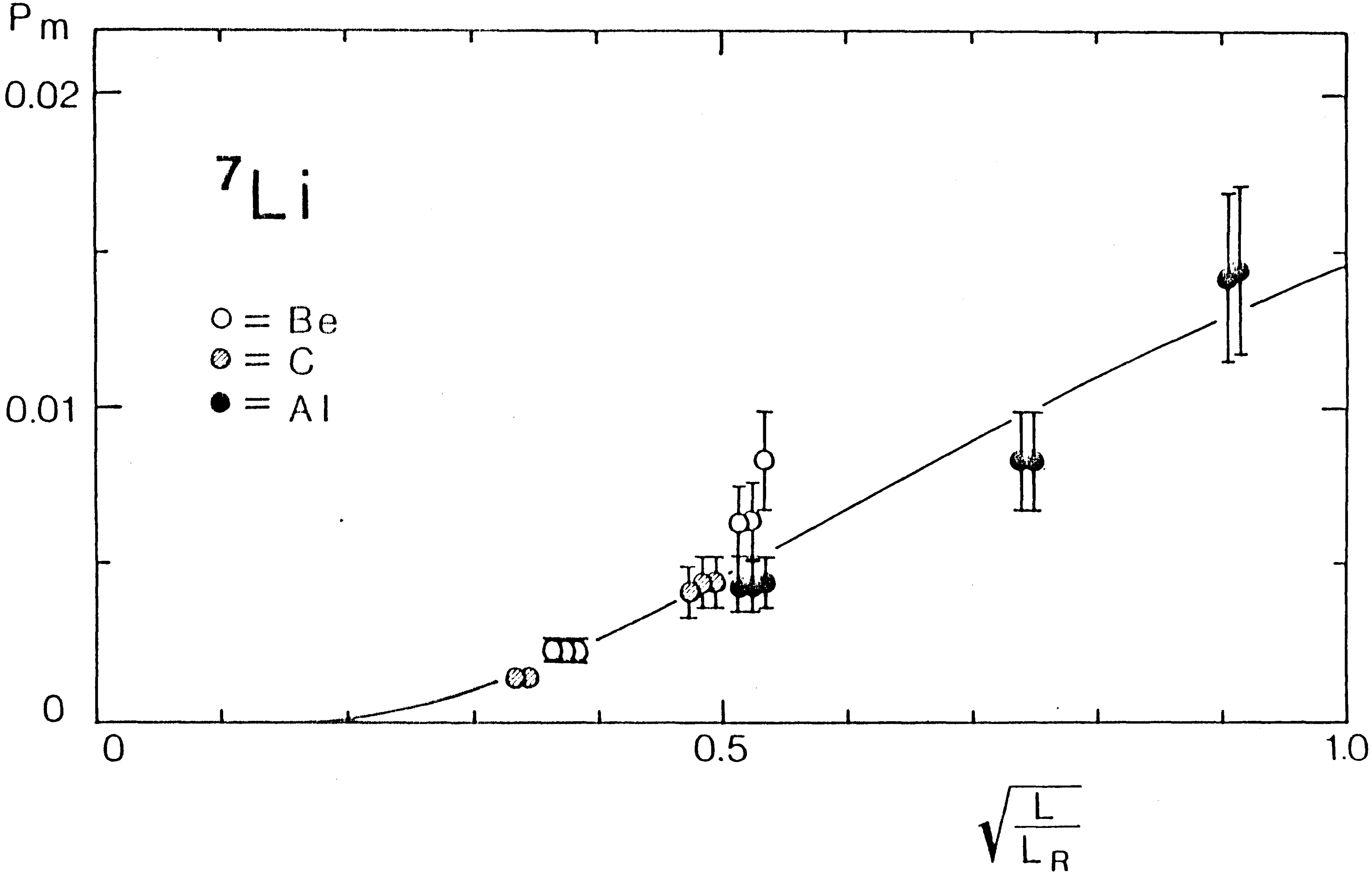

Figure 33

Figure 3.4

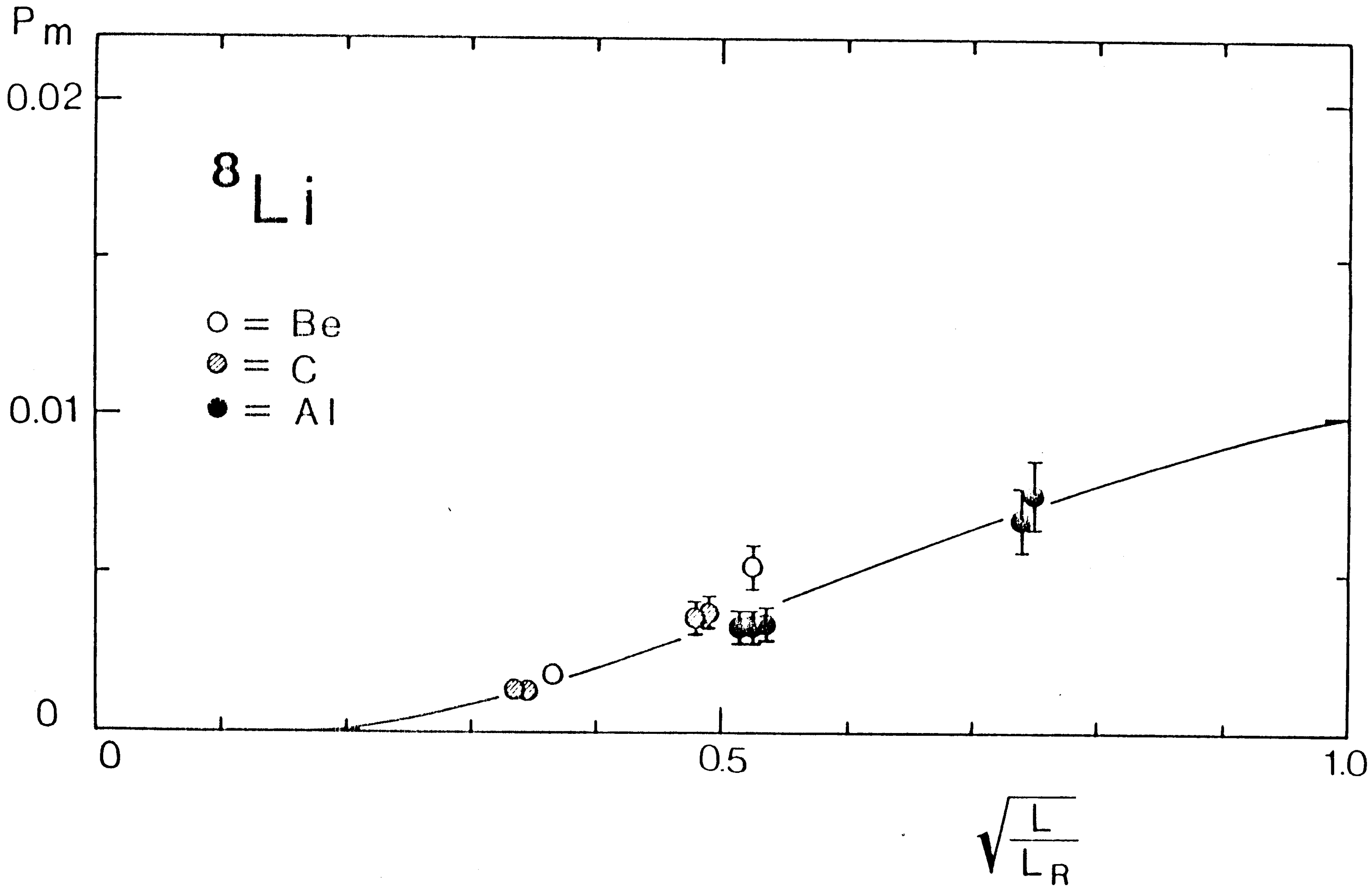

Figure 35

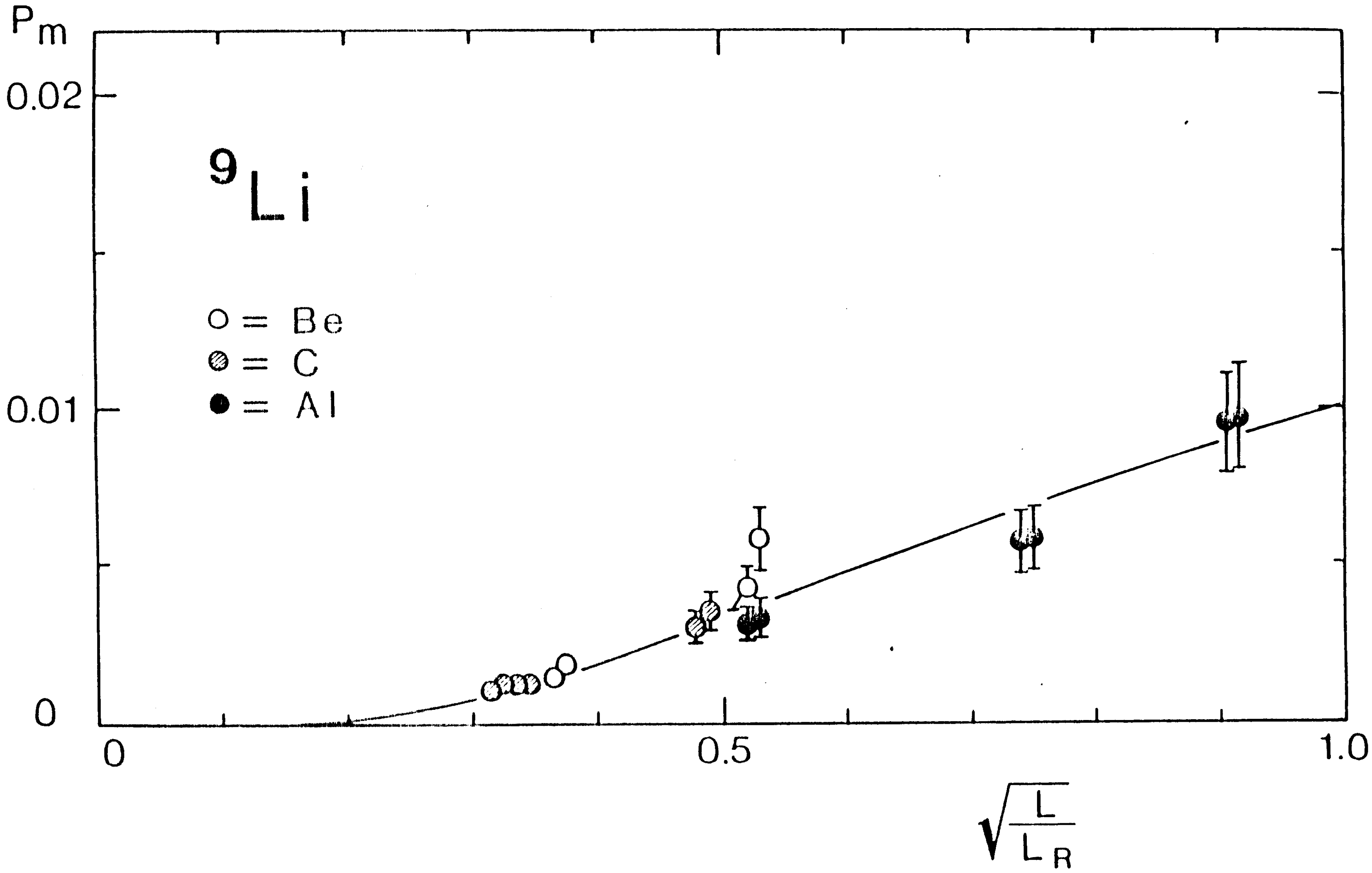

3.1.4. Summary of errors

The errors associated with the interaction cross section were estimated from the uncertainties in γ, γ_0, γ/γ_0, $(1-P_m)$ and t by using the Eq. (2.4). The contribution of each uncertainty to the total error in the interaction cross sections was summarized in Table 7. The main source of error in the interaction cross section is due to the uncertainty in γ. In estimating the errors, we found the first and the second terms in Eq. (2.4) to be dominant and to have a value of 1×10^{-2}. The third term, which is due to the admixture of other nuclei in the charge and the rigidity after the reaction target, was at most 2.6×10^{-3}. The fourth term, which comes from the error in the scattering-out factor P_m, was at most 5.9×10^{-3}. The fifth, term which comes from the error in the target thickness, was at most 6×10^{-4}.

Errors in interaction cross sections $\times 10^{-3}$					
Target	Discription	^3He	^4He	^6He	^8He
Be1	Total $\Delta\sigma_I/\sigma_I$	9.6	10.3	10.8	8.1
	$\Delta\gamma$	8.9	9.5	10.3	7.7
	$\Delta\gamma_0$	3.2	3.5	3.1	2.2
	$\Delta(1-P_m)$	1.5	1.6	0.9	0.8
	$\Delta(\gamma/\gamma_0)$	<1.0	<1.0	<0.8	<0.7
	Δt	0.08	0.08	0.08	0.08
Be2	Total $\Delta\sigma_I/\sigma_I$	9.5	8.9	8.0	5.1
	$\Delta\gamma$	9.2	8.5	7.8	4.9
	$\Delta\gamma_0$	2.2	2.1	1.5	0.9
	$\Delta(1-P_m)$	1.2	1.3	1.2	1.2
	$\Delta(\gamma/\gamma_0)$	<0.5	<0.5	<0.4	<0.3
	Δt	0.3	0.3	0.3	0.3
C1	Total $\Delta\sigma_I/\sigma_I$	10.0	11.0	11.3	6.9
	$\Delta\gamma$	9.1	10.0	10.6	6.5
	$\Delta\gamma_0$	3.3	3.8	3.4	1.9
	$\Delta(1-P_m)$	2.3	2.3	2.0	1.1
	$\Delta(\gamma/\gamma_0)$	<1.1	<1.2	<0.8	<0.7
	Δt	0.6	0.6	0.6	0.6
C3	Total $\Delta\sigma_I/\sigma_I$	15.1	20.6	11.9	10.0
	$\Delta\gamma$	13.2	18.0	10.6	9.1
	$\Delta\gamma_0$	6.6	9.3	4.7	3.3
	$\Delta(1-P_m)$	2.5	2.7	2.0	0.8
	$\Delta(\gamma/\gamma_0)$	<2.1	<2.3	<1.6	<1.4
	Δt	0.1	0.1	0.1	0.1

γ : attenuation factor ($=N_{out}/N_{inc}$) in target-in-run

γ_0 : attenuation factor in target-out-run

(1-P_m) : capture efficiency for non-interacted particles

Table 7 (a)

Errors in interaction cross sections $\times 10^{-3}$					
Target	Discription	^{3}He	^{4}He	^{6}He	^{8}He
Al1	Total $\Delta\sigma_I/\sigma_I$	16.8	22.7	18.9	11.4
	$\Delta\gamma$	14.1	19.2	16.5	10.0
	$\Delta\gamma_0$	7.4	10.3	7.8	4.5
	$\Delta(1-P_m)$	5.0	5.9	4.4	2.7
	$\Delta(\gamma/\gamma_0)$	<2.3	<2.6	<1.9	<1.7
	Δt	0.2	0.2	0.2	0.2
Al2	Total $\Delta\sigma_I/\sigma_I$	11.0	14.5	12.6	7.9
	$\Delta\gamma$	9.5	12.9	11.4	7.0
	$\Delta\gamma_0$	3.7	5.2	3.9	2.3
	$\Delta(1-P_m)$	3.9	3.8	3.7	2.7
	$\Delta(\gamma/\gamma_0)$	<1.2	<1.3	<0.9	<0.8
	Δt	0.4	0.4	0.4	0.4
Al3	Total $\Delta\sigma_I/\sigma_I$	13.5	9.6	10.4	6.7
	$\Delta\gamma$	12.6	8.6	9.5	5.8
	$\Delta\gamma_0$	1.5	2.8	2.6	1.5
	$\Delta(1-P_m)$	1.5	3.2	3.3	3.0
	$\Delta(\gamma/\gamma_0)$	<1.0	<0.9	<0.6	<0.6
	Δt	0.4	0.4	0.4	0.4

γ : attenuation factor ($=N_{out}/N_{inc}$) in target-in-run

γ_0 : attenuation factor in target-out-run

(1-P_m) : capture efficiency for non-interacted particles

Table 7 (b)

Errors in interaction cross sections $\times 10^{-3}$					
Target	Discription	^{6}Li	^{7}Li	^{8}Li	^{9}Li
Be1	Total $\Delta\sigma_I/\sigma_I$	13.0	9.7	11.2	9.0
	$\Delta\gamma$	12.1	9.1	10.7	8.5
	$\Delta\gamma_0$	3.9	3.0	3.3	2.7
	$\Delta(1-P_m)$	2.6	1.0	0.7	0.5
	$\Delta(\gamma/\gamma_0)$	<1.1	<0.8	<0.8	<0.9
	Δt	0.08	0.08	0.08	0.08
Be2	Total $\Delta\sigma_I/\sigma_I$	9.9	7.2	8.4	6.6
	$\Delta\gamma$	9.4	6.9	8.2	6.4
	$\Delta\gamma_0$	1.9	1.4	1.6	1.3
	$\Delta(1-P_m)$	2.5	1.4	0.8	1.1
	$\Delta(\gamma/\gamma_0)$	<0.5	<0.4	<0.4	<0.4
	Δt	0.3	0.3	0.3	0.3
C1	Total $\Delta\sigma_I/\sigma_I$	14.3	10.4	11.9	9.2
	$\Delta\gamma$	13.1	9.6	11.2	8.6
	$\Delta\gamma_0$	4.3	3.2	3.6	2.9
	$\Delta(1-P_m)$	3.7	2.1	1.3	1.2
	$\Delta(\gamma/\gamma_0)$	<1.2	<0.9	<0.9	<0.9
	Δt	0.6	0.6	0.6	0.6
C3	Total $\Delta\sigma_I/\sigma_I$	20.9	15.2	17.9	13.6
	$\Delta\gamma$	18.5	13.6	15.5	12.1
	$\Delta\gamma_0$	8.4	6.3	7.0	5.8
	$\Delta(1-P_m)$	4.5	1.6	1.0	1.0
	$\Delta(\gamma/\gamma_0)$	<2.4	<1.7	<1.7	<1.8
	Δt	0.1	0.1	0.1	0.1

γ : attenuation factor $(=N_{out}/N_{inc})$ in target-in-run

γ_0 : attenuation factor in target-out-run

$(1\text{-}P_m)$: capture efficiency for non-interacted particles

Table 7 (c)

Errors in interaction cross sections $\times 10^{-3}$					
Target	Discription	^{6}Li	^{7}Li	^{8}Li	^{9}Li
Al1	Total $\Delta\sigma_I/\sigma_I$	24.4	17.5	19.0	15.6
	$\Delta\gamma$	20.4	14.9	16.8	13.5
	$\Delta\gamma_0$	9.9	7.5	8.1	7.0
	$\Delta(1-P_m)$	8.6	5.0	2.9	2.9
	$\Delta(\gamma/\gamma_0)$	<2.8	<2.0	<2.0	<2.2
	Δt	0.2	0.2	0.2	0.2
Al2	Total $\Delta\sigma_I/\sigma_I$	16.8	12.1	13.0	10.5
	$\Delta\gamma$	13.8	10.3	11.9	9.4
	$\Delta\gamma_0$	4.9	3.7	4.1	3.5
	$\Delta(1-P_m)$	8.2	5.0	3.2	2.9
	$\Delta(\gamma/\gamma_0)$	<1.4	<1.0	<1.0	<1.1
	Δt	0.4	0.4	0.4	0.4
Al3	Total $\Delta\sigma_I/\sigma_I$	13.8	10.5		8.8
	$\Delta\gamma$	11.4	8.5		7.8
	$\Delta\gamma_0$	3.3	2.5		2.3
	$\Delta(1-P_m)$	7.0	5.6		3.3
	$\Delta(\gamma/\gamma_0)$	<0.9	<0.7		<0.7
	Δt	0.4	0.4		0.4

γ : attenuation factor ($=N_{out}/N_{inc}$) in target-in-run

γ_0 : attenuation factor in target-out-run

(1-P_m) : capture efficiency for non-interacted particles

Table 7 (d)

4. Experimental result

4.1. The interaction cross sections

Figures 36 - 43 show the values of the interaction cross sections obtained in the different runs. The data are plotted against γ (=N_{out}/N_{inc}). No γ (or target thickness) dependence is observed in these figures. The closed circles in the right-hand side of a figure are the average values for different runs.

The interaction cross sections of He,Li and Be isotopes determined in this experiment are listed in table 8. Errors listed in the table were determined as discussed in the previous section. For the case of ^{4}He + Al the data fluctuation among different runs is bigger than the error which was determined in the previous section. Therefore the standard deviation of these fluctuation was used as the final error. In all other cases, errors were comparable to or less than the standard deviations of the fluctuation among the different runs.

The interaction cross sections are plotted in Figures 44 and 45. The mark "X" shows the inelastic cross section data for ^{4}He + C measured by Jaros et al.[15] The present data is in good agreement with their data.

4.2. The interaction radii of nuclei

As discussed in section 2.3, we defined the interaction radius R_I of nucleus as shown in Eq. (2.5). The difference of the radii between nucleus X and Y can be calculated as

$$R_I(X)-R_I(Y)=\sqrt{\sigma_I(X,T)/\pi} - \sqrt{\sigma_I(Y,T)/\pi} \tag{4.1}$$

where T denotes target nuclei. The radius difference between He isotopes and ^{3}He thus obtained is shown in Fig. 46. The radius difference is essentially independent of target nuclei (except the value obtained from ^{4}He + Be). Figure 47 shows the difference of radii between two target nuclei. The difference of target nuclear radii is essentially independent of the beam nuclei

Interaction cross sections (σ_I) in mb			
Beam	Be target	C target	Al target
^{3}He	498±4	550±5	850±9
^{4}He	485±4	503±5	780±13
^{6}He	672±7	722±6	1063±8
^{8}He	757±4	817±6	1197±9
^{6}Li	651±6	688±10	1010±11
^{7}Li	686±4	736±6	1071±7
^{8}Li	727±6	768±9	1147±14
^{9}Li	739±5	796±6	1135±7
^{11}Li		1056.0±30.0	
^{9}Be	755±5	806±9	1174±10

Table 8

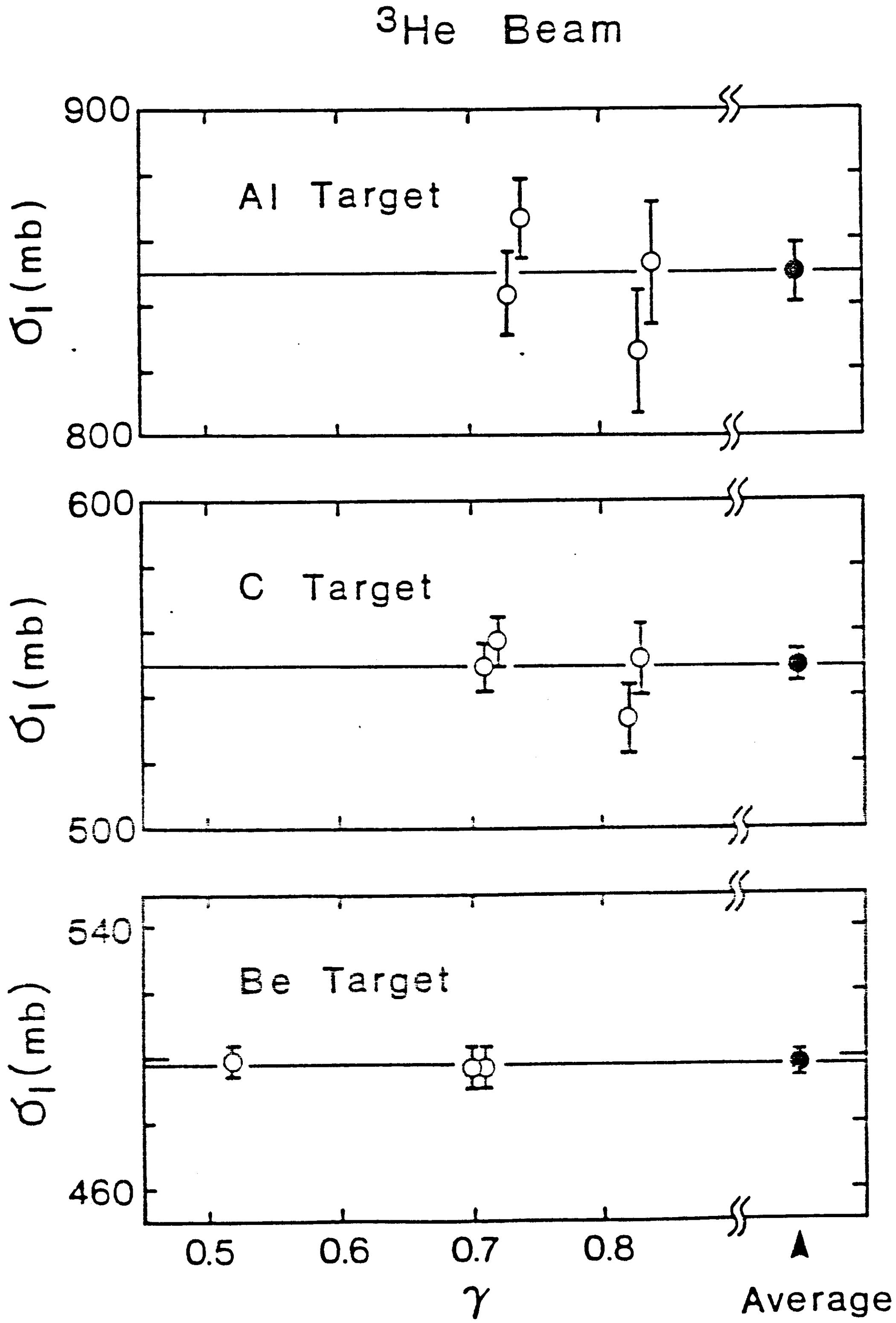

^{3}He Beam
Al Target
C Target
Be Target
900
800
600
500
540
460
σ_I (mb)
0.5
0.6
0.7
0.8
γ
Average

Figure 36

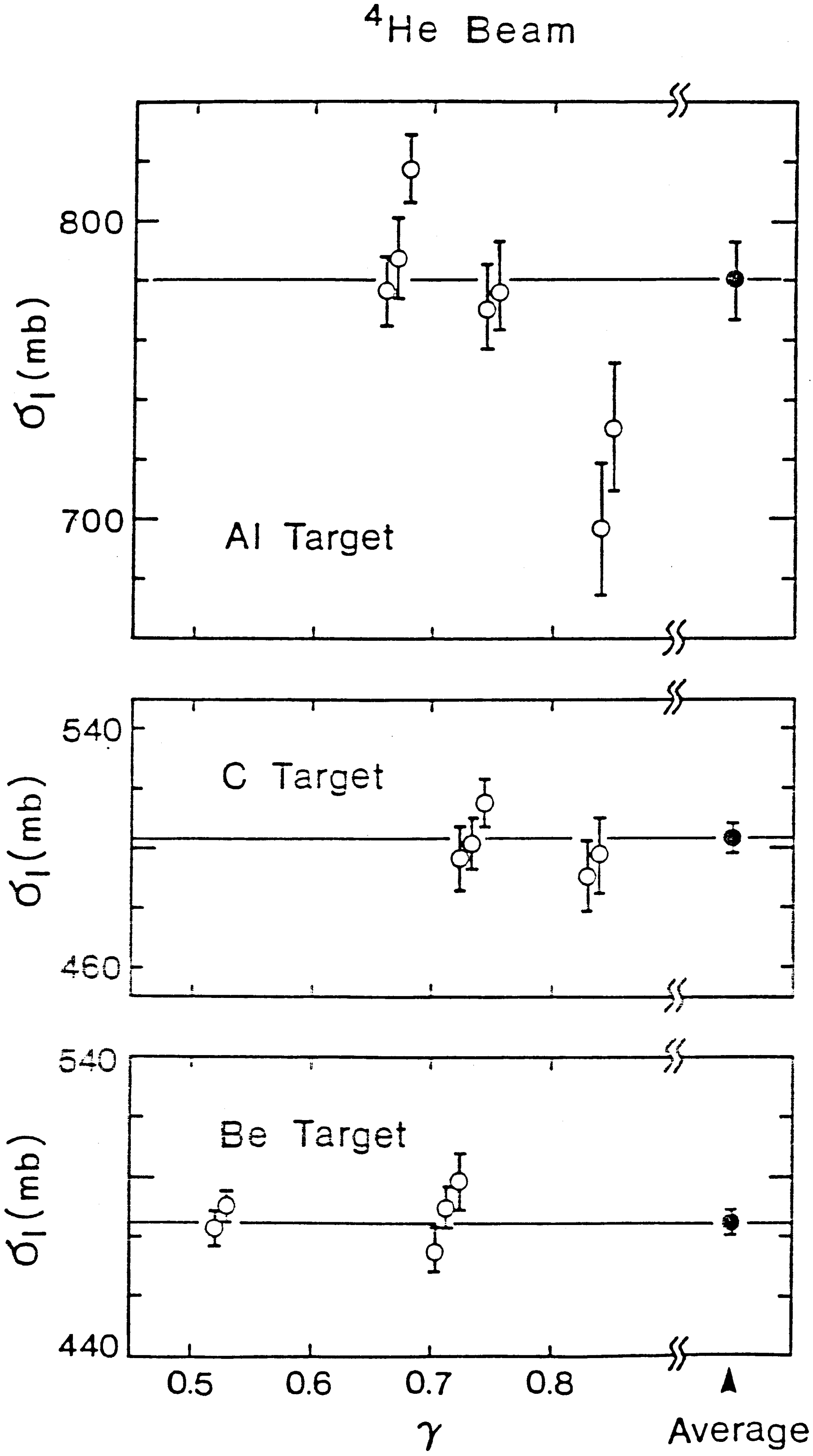
^{4}He Beam
800
700
σ_I(mb)
Al Target
540
460
σ_I(mb)
C Target
540
440
σ_I(mb)
Be Target
0.5
0.6
0.7
0.8
γ
Average

Figure 37

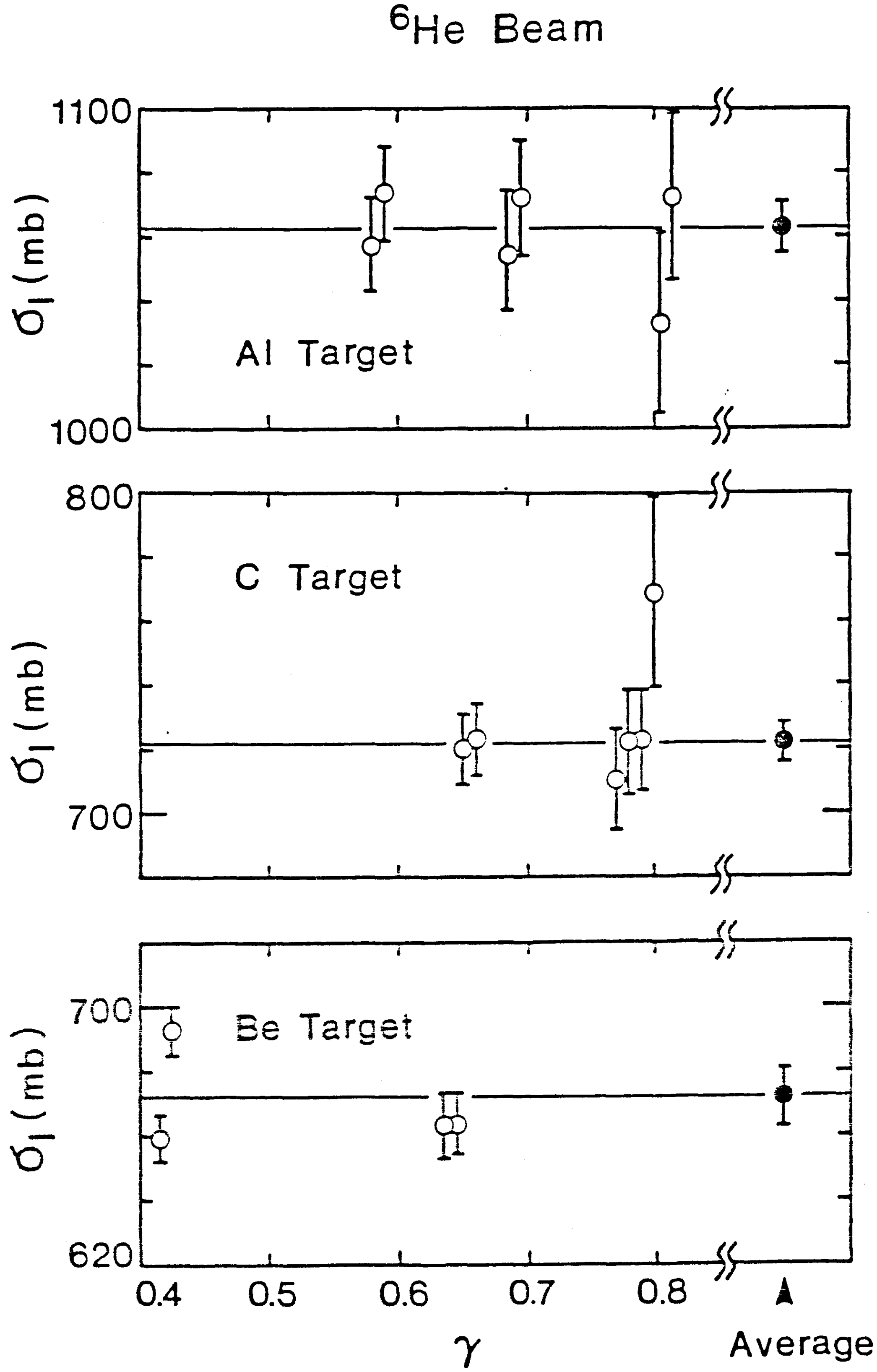

⁶He Beam
1100
1000
σI (mb)
Al Target
800
700
C Target
Be Target
620
0.4
0.5
0.6
0.7
0.8
γ
Average

Figure 38

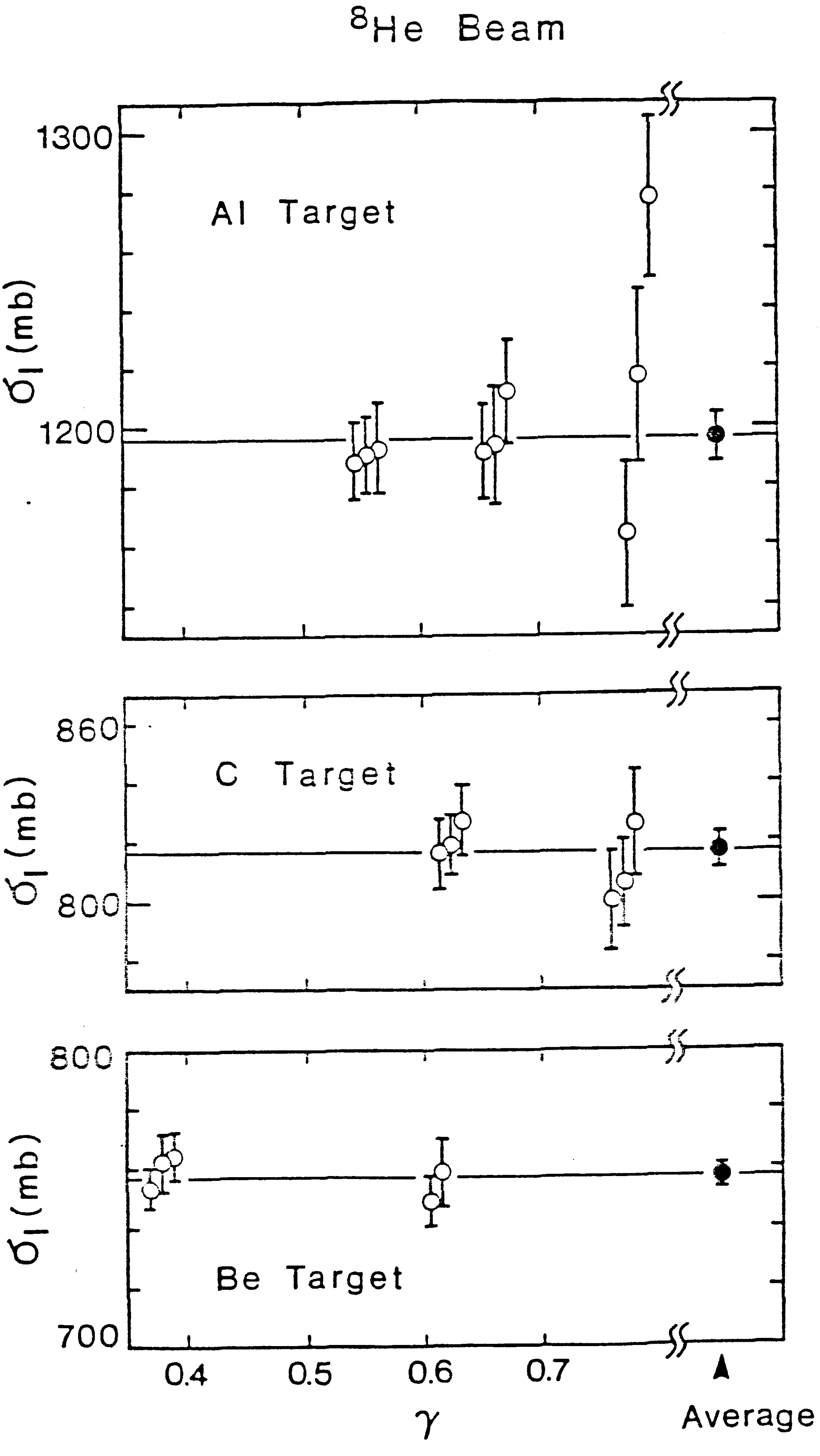

^{8}He Beam
1300
1200
Al Target
860
800
C Target
800
700
Be Target
σ_I (mb)
0.4
0.5
0.6
0.7
γ
Average

Figure 39

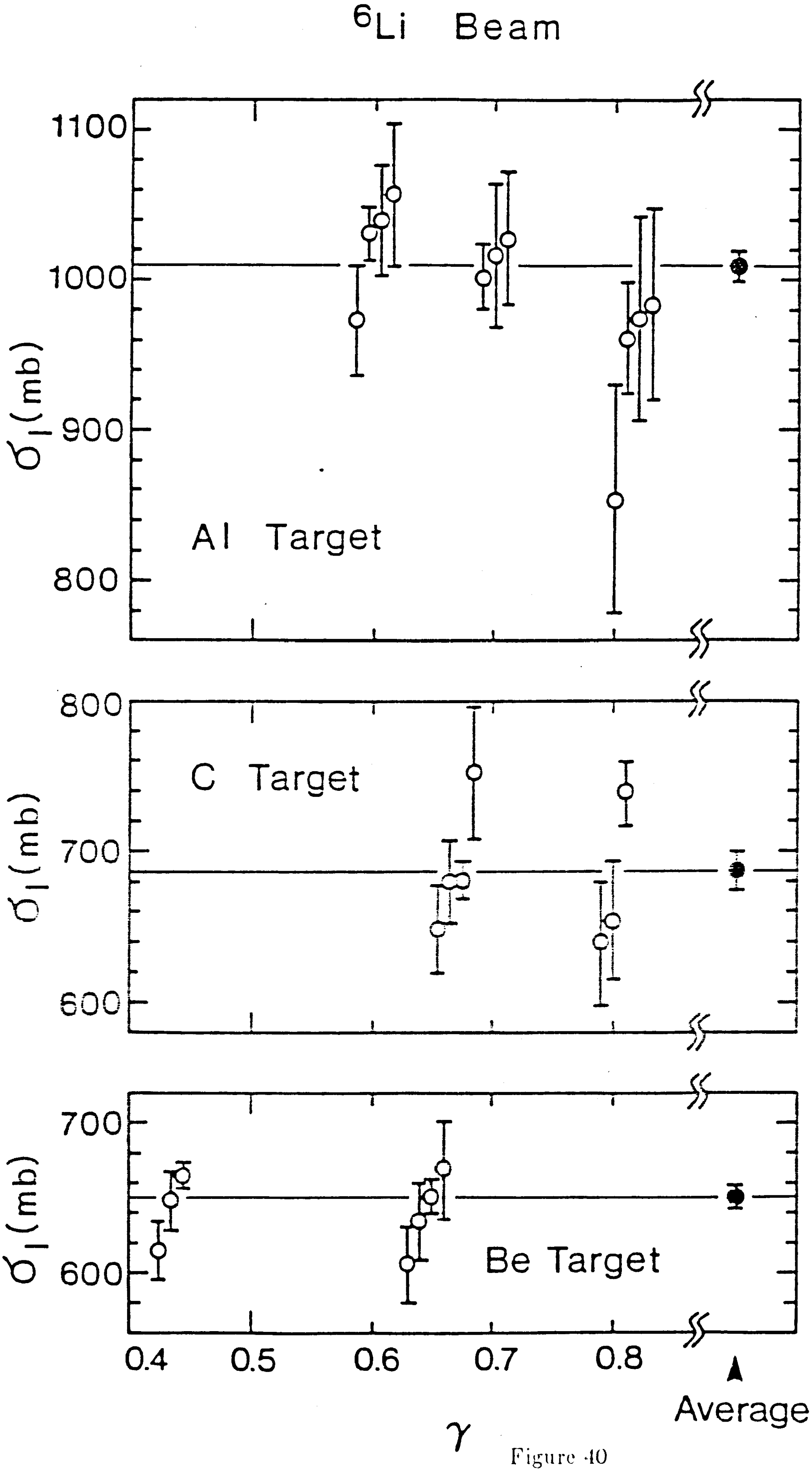

^{6}Li Beam
1100
1000
900
800
σ_I (mb)
Al Target
800
700
600
σ_I (mb)
C Target
700
600
σ_I (mb)
Be Target
0.4
0.5
0.6
0.7
0.8
Average
γ

Figure 40

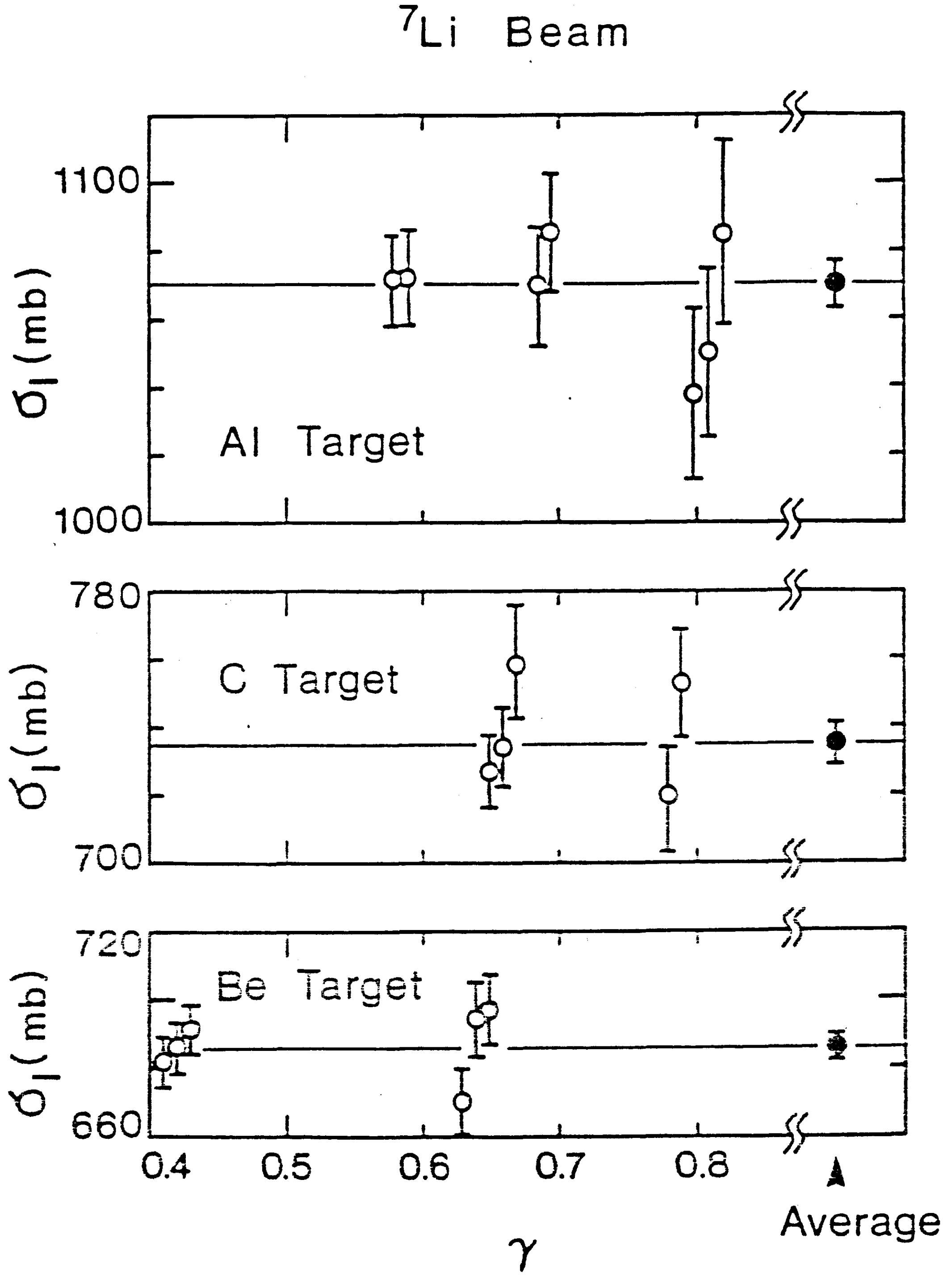

^{7}Li Beam
1100
1000
σ_I (mb)
Al Target
780
700
σ_I (mb)
C Target
720
660
σ_I (mb)
Be Target
0.4
0.5
0.6
0.7
0.8
Average
γ

Figure 41

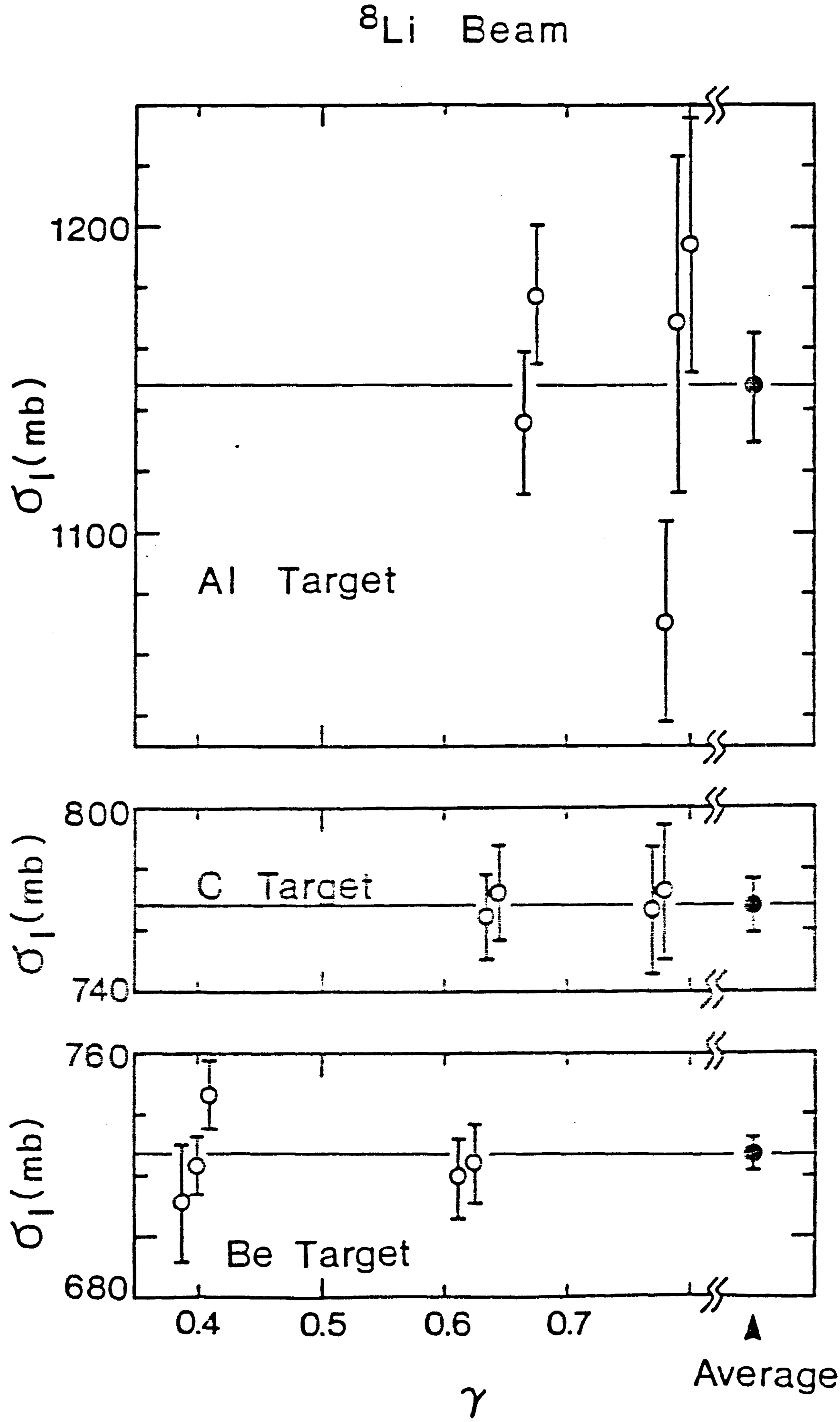
8Li Beam
1200
1100
Al Target
σI(mb)
800
740
C Target
σI(mb)
760
680
Be Target
σI(mb)
0.4
0.5
0.6
0.7
Average
γ

Figure 42

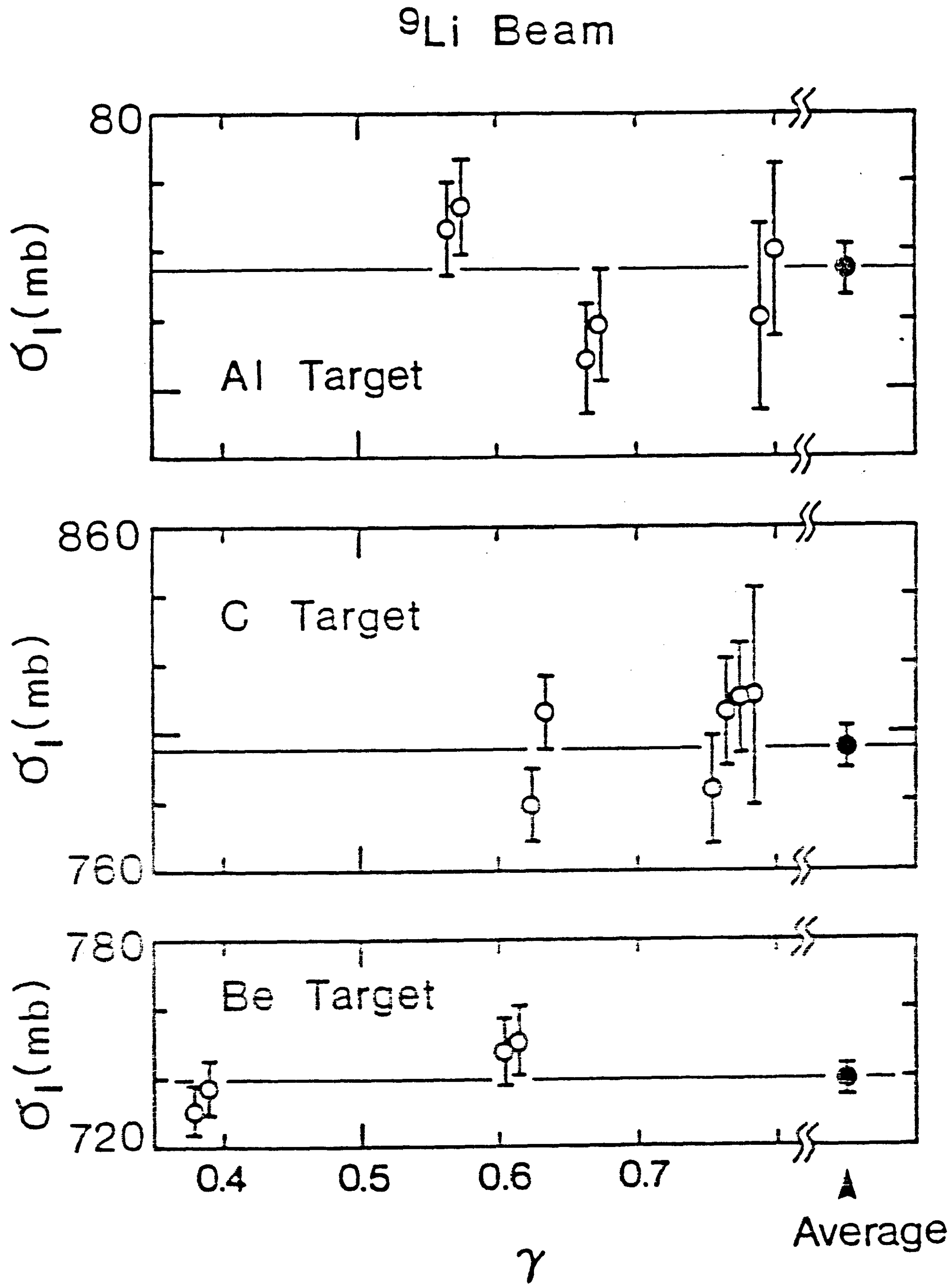
^{9}Li Beam
80
σ_I(mb)
Al Target
860
C Target
σ_I(mb)
760
780
Be Target
σ_I(mb)
720
0.4
0.5
0.6
0.7
Average
γ

Figure 43

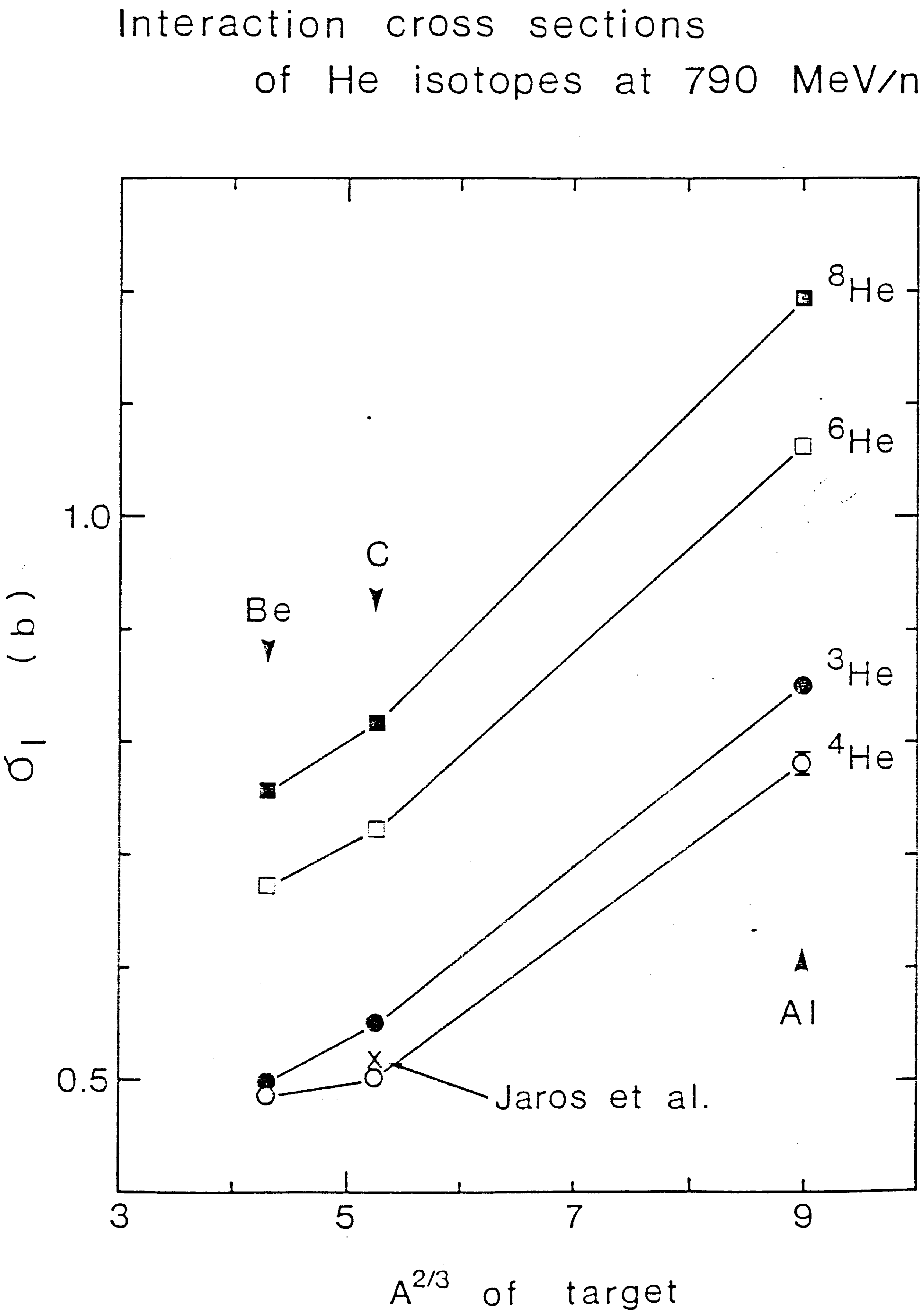
Interaction cross sections
of He isotopes at 790 MeV/n
σI (b)
1.0
0.5
3
5
7
9
A2/3 of target
Be
C
Al
8He
6He
3He
4He
Jaros et al.

Figure 44

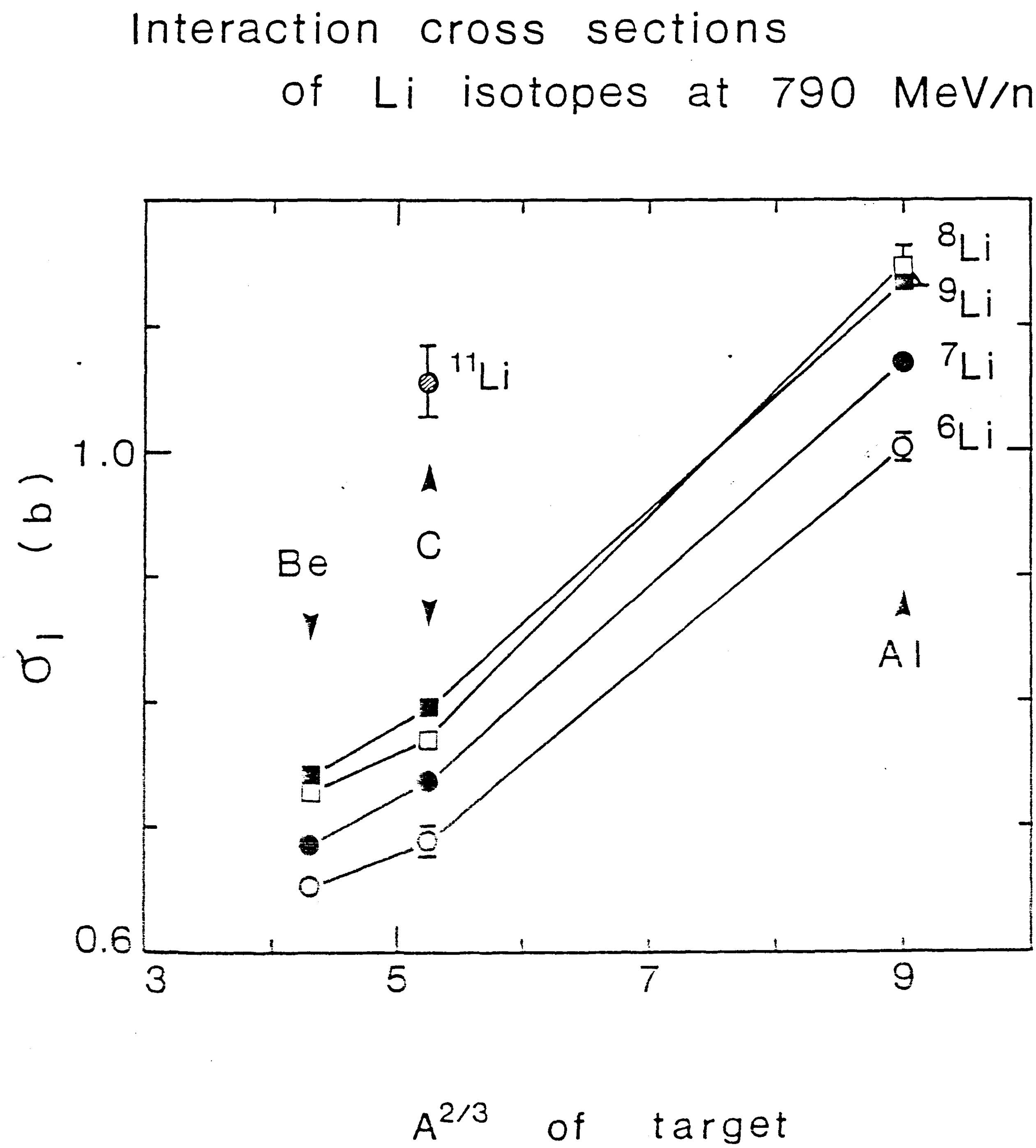
Interaction cross sections
of Li isotopes at 790 MeV/n
σI (b)
1.0
0.6
3
5
7
9
A2/3 of target
8Li
9Li
7Li
6Li
11Li
Be
C
Al

Figure 45

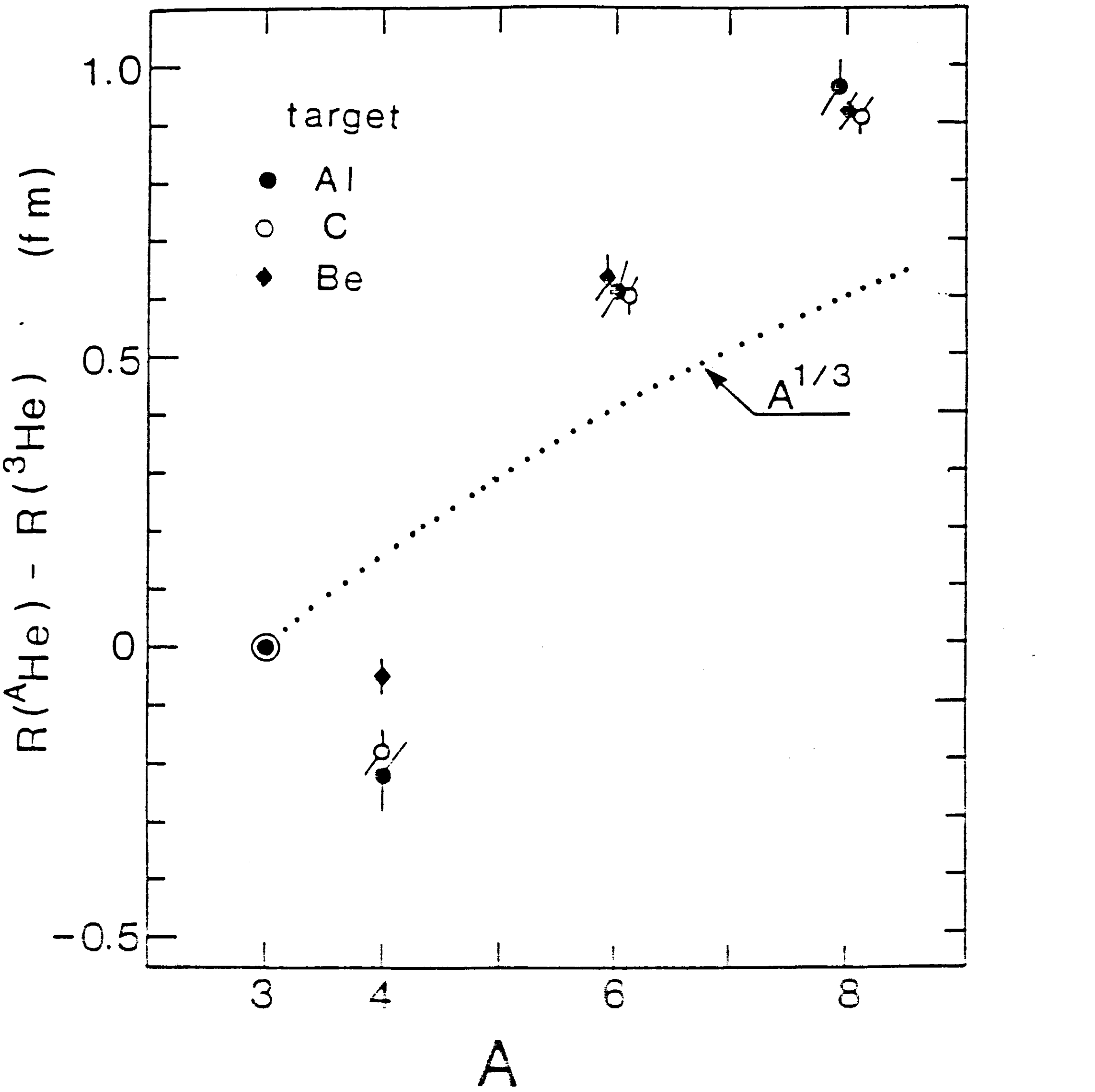

Figure 46

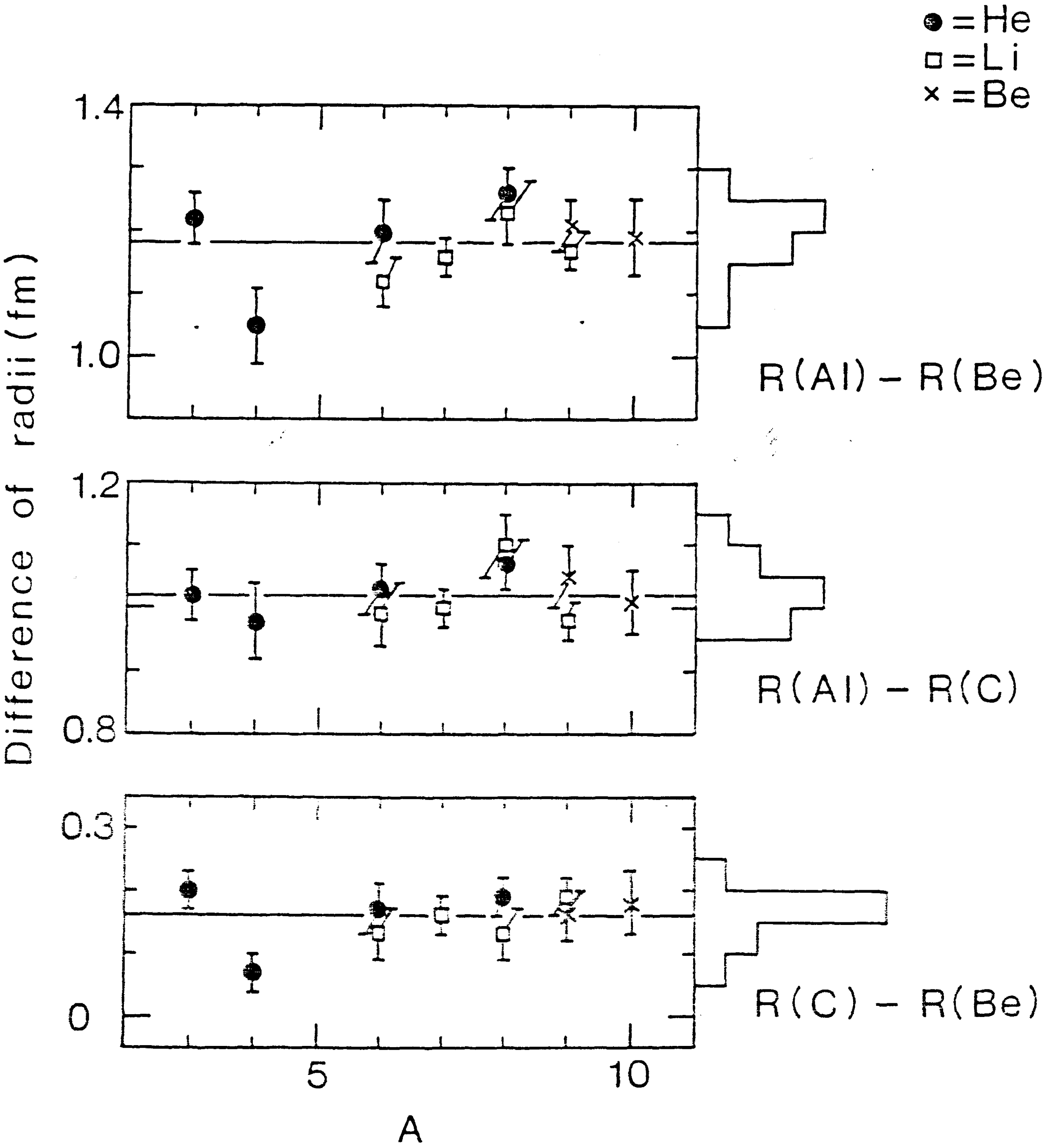
● = He
□ = Li
× = Be
1.4
1.0
R(Al) − R(Be)
1.2
0.8
R(Al) − R(C)
0.3
0
R(C) − R(Be)
5
10
A
Difference of radii (fm)

Figure 47

(except the value obtained from ^{4}He + Be). These results are consistent with the assumption that the target and the projectile radii are separable within ± 0.02 fm as defined in equation (2.5).

The absolute value of ^{4}He, ^{9}Be, and ^{12}C radii can be calculated by the least squares fitting ; using the data of ^{9}Be + ^{9}Be, ^{9}Be + ^{12}C in the this experiment, ^{12}C + ^{12}C, ^{4}He + ^{4}He, ^{12}C + ^{4}He data from Jaros et al.[15], and ^{12}C + ^{12}C data from Lindstrom et al.[18]. The results are $R_I(^4\mathrm{He})=(1.41\pm0.03)$, $R_I(^9\mathrm{Be})=(2.45\pm0.01)$, $R_I(^{12}\mathrm{C})=(2.61\pm0.02)$ in fm.

The radius of ^{27}Al is calculated to be $R_I(^{27}\mathrm{Al})=(3.63\pm0.04)$ fm, from the values of $\sigma_I(^4\mathrm{He},^{27}\mathrm{Al})$ and $\sigma_I(^9\mathrm{Be},^{27}\mathrm{Al})$ together with $R_I(^4\mathrm{He})$ and $R_I(^9\mathrm{Be})$. Using the radii of ^{9}Be, ^{12}C, and ^{27}Al, the radii of the other He and Li isotopes were calculated for each target. The averages of the radii for the He and Li isotopes obtained from all targets are listed in Table 9 and plotted in Fig. 48. The following characteristics should be noted for the radii of He and Li isotopes. The radii of light nuclei determined in this experiment shows a $1.2\times A^{1/3}$ dependence. It shows a good agreement with the behavior of the radii of stable nuclei as discussed in 2.3.1. The radius of ^{4}He is the smallest of the He isotopes. This finding agree with result of the electron scattering experiment which conclude that the root-mean-square radius of ^{4}He was smaller than that of ^{3}He.[19,20] A large increase of radius was observed from ^{9}Li to ^{11}Li. The radii of ^{6}Li and ^{8}Li are about 0.1 fm smaller than the radii of ^{6}He and ^{8}He, respectively. This provide the first observation of the difference of the nuclear radii between isobars.

The interaction radii (R_I) of He isotopes (fm)			
^{3}He	^{4}He	^{6}He	^{8}He
1.55±0.02	1.41±0.03	2.18±0.02	2.48±0.03

The interaction radii (R_I) of Li isotopes (fm)				
^{6}Li	^{7}Li	^{8}Li	^{9}Li	^{11}Li
2.09±0.02	2.23±0.02	2.36±0.02	2.41±0.02	3.20±0.08

The interaction radii (R_I) (fm)		
^{9}Be	^{12}C	^{27}Al
2.45±0.01	2.61±0.02	3.63±0.04

Table 9

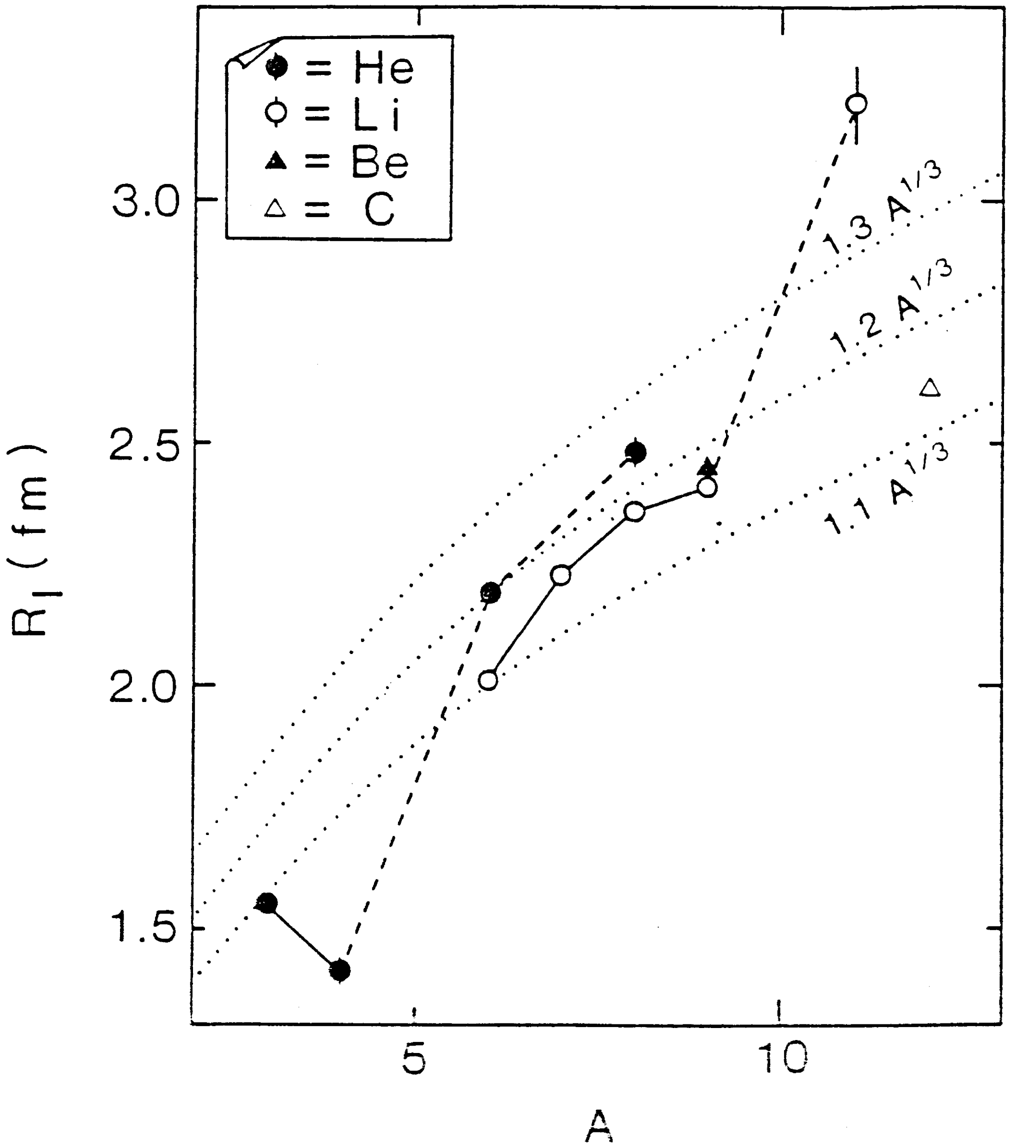

XBL 856-2809

Figure 48

5. Discussion and conclusion

5.1. Summary of the present result

In this experiment secondary beams of ^{3}He, ^{4}He,^{6}He,^{8}He,^{6}Li, ^{7}Li,^{8}Li,^{9}Li,^{11}Li, and ^{9}Be were produced at 790 MeV/nucleon through the projectile fragmentation processes. The interaction cross sections (σ_I) of these nuclei on Be, C, Al targets were measured. From σ_I the intearaction nuclear radii (R_I) were deduced using Eq. (2.5). The following characteristic were observed as the results:

(1) Mass dependence of interaction radii

In general the nuclear interaction radii of light nuclei including β-stable nuclei are in agreement with $R_I = 1.2 \times A^{1/3}$ fm.

(2) Isotope dependence of interaction radii

The interaction radius of ^{4}He is smaller than that of ^{3}He (the charge root-mean-square radius obtained by the electron scattering experiment shows the same result[19,20]), and the interaction radius of ^{11}Li is considerably large compared with $R_I = 1.2 \times A^{1/3}$ fm.

(3) Isobar dependence of interaction radii

The interaction radii of ^{6}Li and ^{8}Li are about 0.1 fm smaller than those of ^{6}He and ^{8}He, respectively.

5.2. Discussion

Assuming that matter distribution of nucleus has a sharp edge, a radius of nucleus can be determined definitely, however the nucleus has a diffused tail. When radii of nuclei are discussed, we should make clear the definition of radii. The definition of the interaction nuclear radius (R_I) have been given already. We will describe R_I more visibly in comparison with the root-mean-square radius (R^e_{rms}) obtained by electron scattering experiments[21].

Figure 49 shows a comparison between the presently determined radii (R_I) for stable isotopes and the root-mean-square radii (R^e_{rms}) obtained from electron scattering[21]. The mass number (A) dependence of R_I and R^e_{rms} show a notable difference: R_I increases with increasing A whereas R^e_{rms} stays almost constant for $A > 5$. In order to understand the difference in the A dependence, we made a Glauber model calculation for the interaction cross sections based on Karol's prescription procedure[22]. Here, the interaction cross section (σ_I) was calculated using a Gaussian nuclear density distributionof the form

$$\rho(r) = \frac{A}{a^3\pi^{3/2}}\exp[-\frac{r^2}{a^2}] \qquad (5.1)$$

where r is the distance from the center of nucleus and a is the width parameter of the Gaussian distribution. The details of the calculation are described in Appendix. Calculations were made for the collisions of identical isotopes, e.g. ^{6}Li+^{6}Li. The width parameter a was taken as a fitting parameter to reproduce the σ_I. Although we did not measure some of σ_I for collision of identical isotopes, e.g. σ_I(^{6}Li,^{6}Li), values were calculated from the presently determined R_I using Eq. (2.5). These values are considered to be accurate within 1 percent because of the projectile-target separability discussed in the previous section.

The root-mean-square radius (R^G_{rms}) thus calculated from the Gaussian matter distribution fitted to reproduce the σ_I are also shown in Fig. 49. Although the absolute values were generally smaller than R^e_{rms}, the A dependence of R^e_{rms} was well reproduced. The obtained Gaussian density distributions are shown in Fig. 50. The values of R_I and R^G_{rms} for ^{4}He, ^{6}Li, ^{7}Li, ^{9}Be, ^{12}C are also shown in Fig. 50. We note that the interaction radius R_I, except for the ^{4}He data, are approximately equal to the radius where the matter density is 0.04-0.05 nucleon/fm^3.

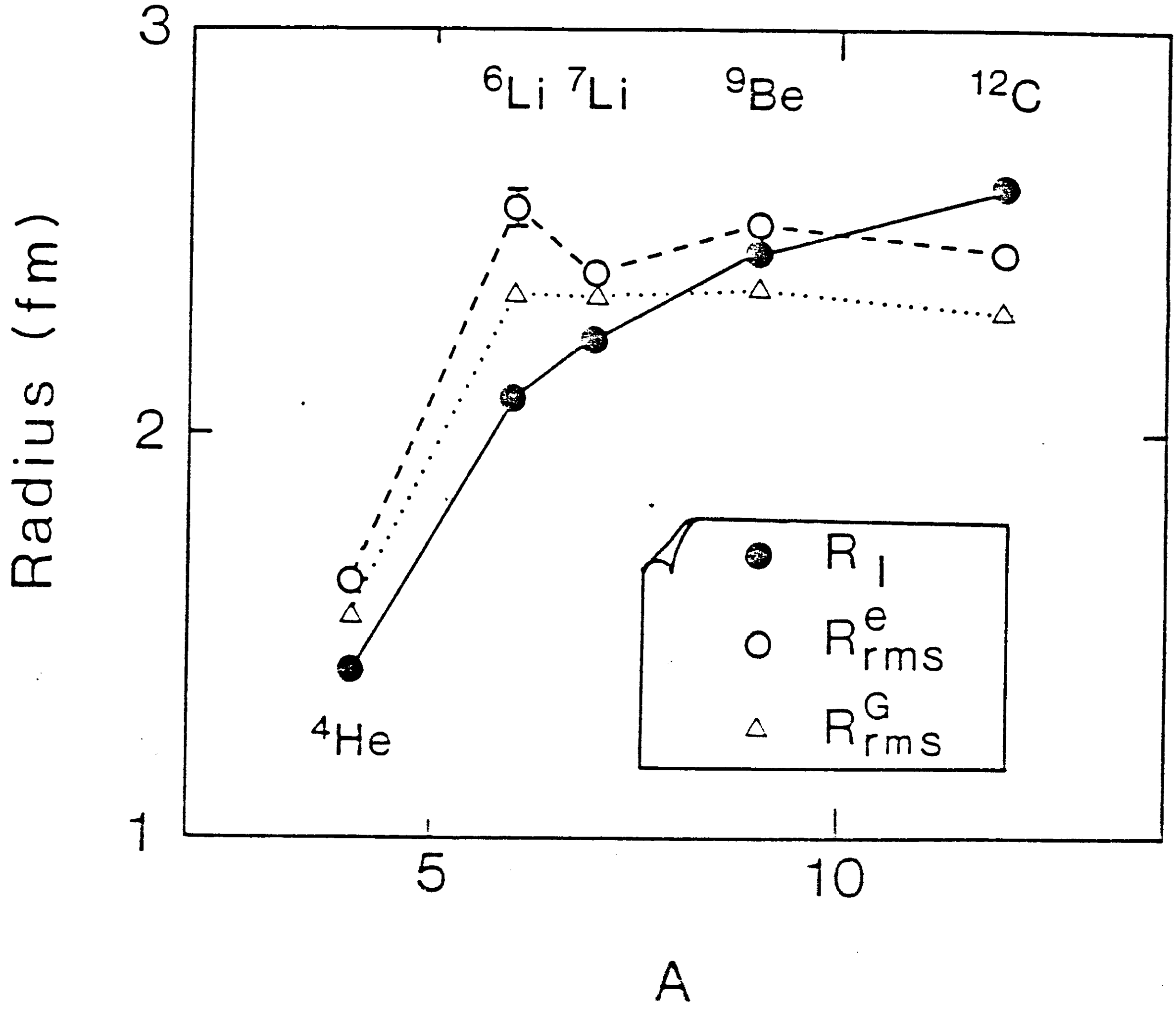

XBL 856-2808

Figure 49

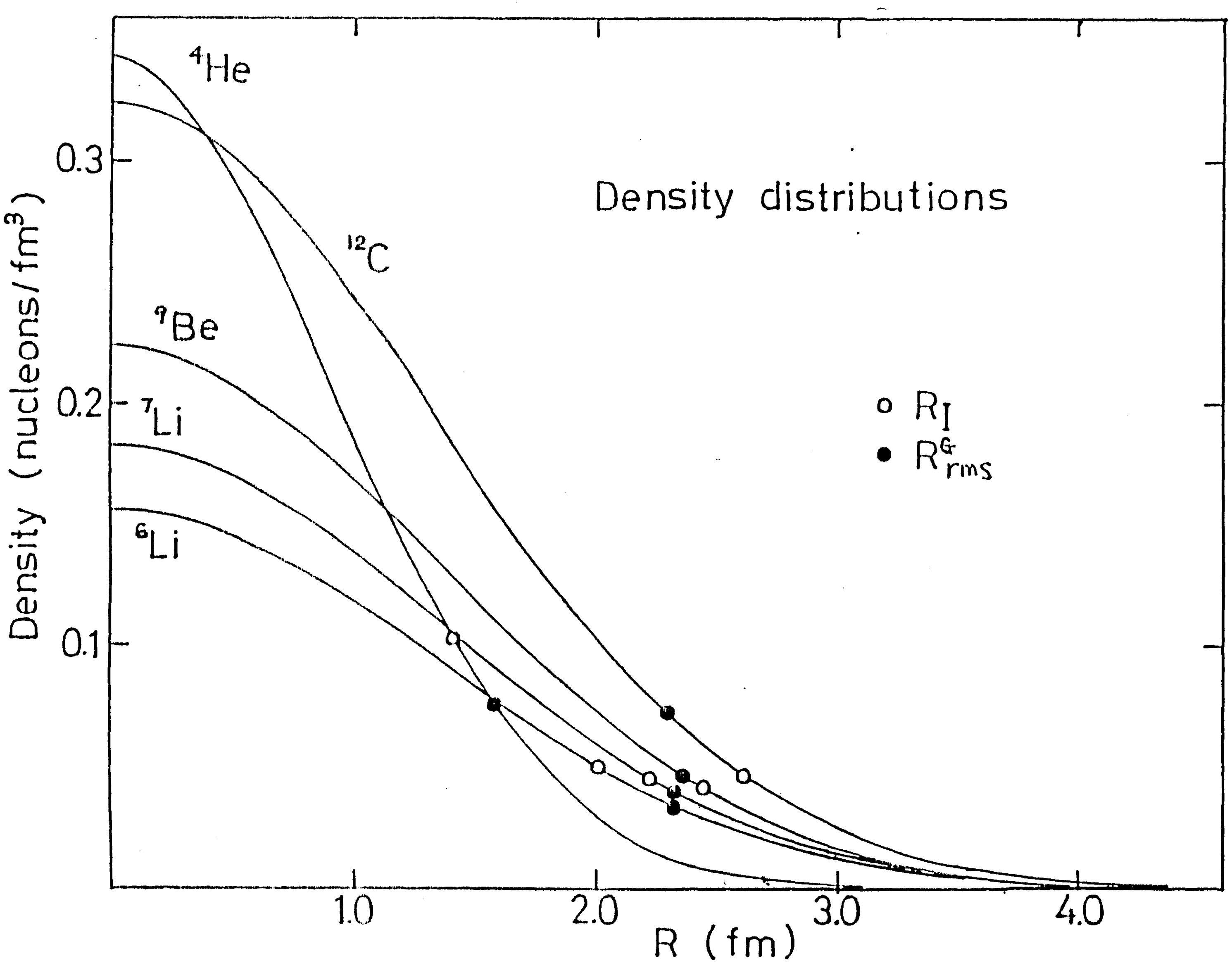

Density distributions
Density (nucleons/fm^3)
R (fm)
0.1
0.2
0.3
1.0
2.0
3.0
4.0
^4He
^{12}C
^9Be
^7Li
^6Li
○ R_I
● R^G_{rms}

Figure 50

Figures 51 and 52 also show the Gaussian density distribution obtained by the same calculation for He and Li isotopes, respectively. The figures show the same characteristic as above.

Next we discuss the isotope dependence of the interaction radius. As seen in Fig. 48, the interaction radii of light nuclei show a rough agreement with $R_I = 1.2 \times A^{1/3}$ except ^{4}He and ^{11}Li. ^{4}He is a double-closed-shell nucleus, therefore its size is extremely small. On the other hand we found that ^{11}Li has a very large radius compared with the dependence $1.2 \times A^{1/3}$. The large radius of ^{11}Li could be due to an expansion of neutron distribution, since ^{11}Li is believed to be the isotope with the largest number of neutrons. In order to see the effect of neutron excess we refer to the calculation of RMS radii for O, Na, K and Rb isotopes by M Beiner et al.[23] using the energy density formalism. Figure 53 shows the RMS radii for proton (r_p), neutron (r_n) and the matter distributions (r_m) in O, Na, K, and Rb isotopes. They are plotted against the neutron number (N). It is seen that the RMS radii of the neutron density distribution increases faster than $A^{1/3}$. The behavior of the calculated RMS radii for O, Na, K and Rb isotopes is similar to that of the interaction radii of the Li isotopes obtained in this experiment.

Very recently, H. Sato calculated the RMS radii[24] of He isotopes (A =4,6,8) using a density-dependent Hartree-Fock (DDHF) calculation[25] with various Skyrme potential (II - VI). The RMS radii obtained by DDHF are plotted in Fig. 54 against the mass number, where SK denotes the Skyrme potential. The proton and the neutron density distributions obtained by Skyrme V are described in Fig. 55. This figure shows the expansion of the neutron density distribution for neutron rich nuclei. The interaction cross sections of He isotopes (A =4,6,8) + C were also calculated using the Glauber theory with the density distribution obtained from the DDHF calculation. The calculated interaction cross section and experimental σ_I of He + C are plotted in Fig. 56. The interaction cross sections of ^{6}He + ^{12}C and ^{8}He + ^{12}C show agreement

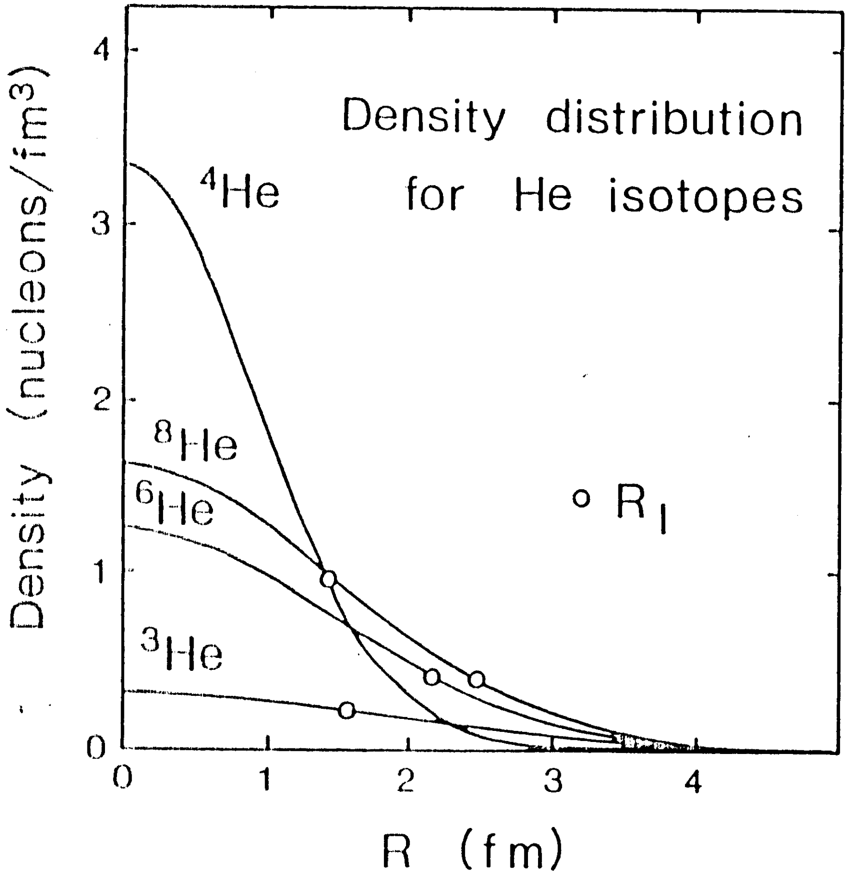
Density distribution
for He isotopes
4He
8He
6He
3He
R I
Density (nucleons/fm3)
R (fm)
0
1
2
3
4

Figure 51

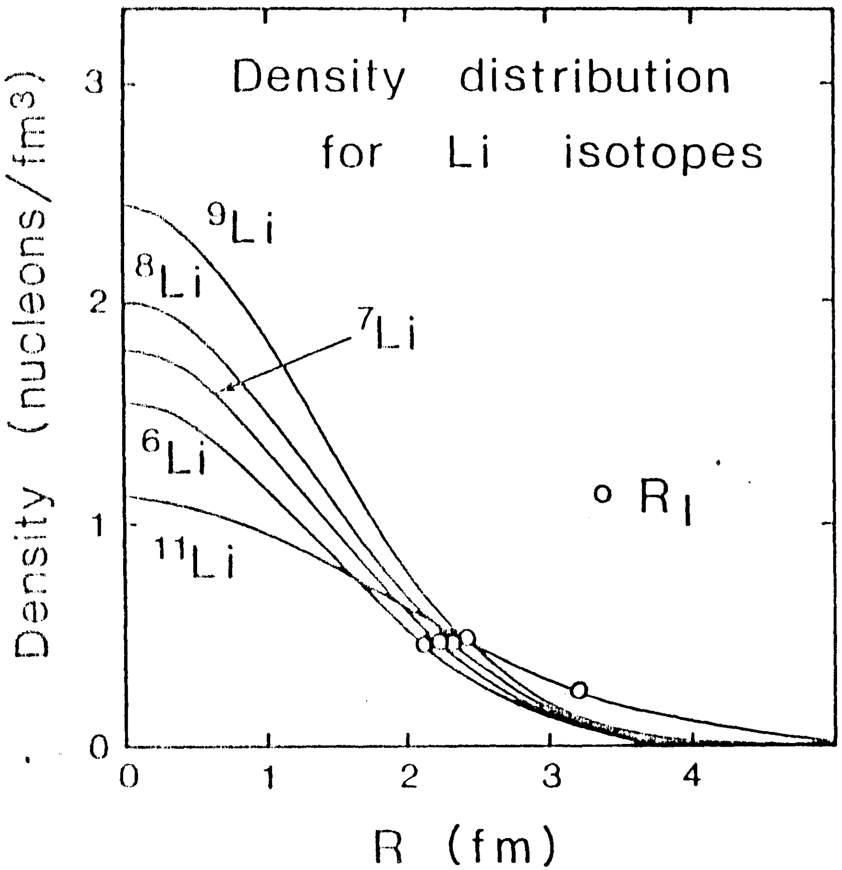
Density distribution
for Li isotopes
^{9}Li
^{8}Li
^{7}Li
^{6}Li
^{11}Li
o R_I
Density (nucleons/fm^3)
R (fm)
0
1
2
3
4

Figure 52

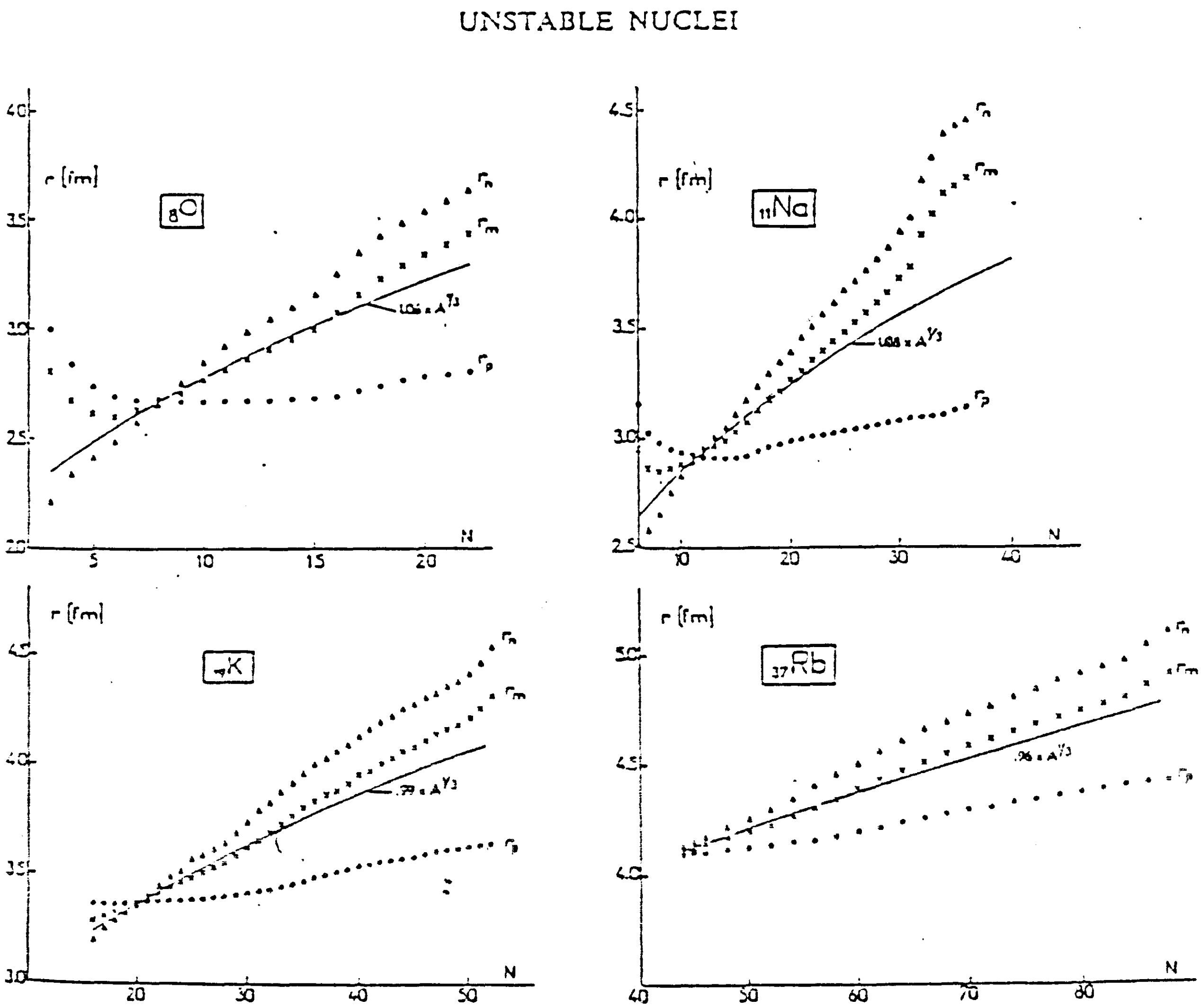

· Proton, neutron and matter radii plotted against N for the O, Na, K and Rb isotopes.

Figure 53

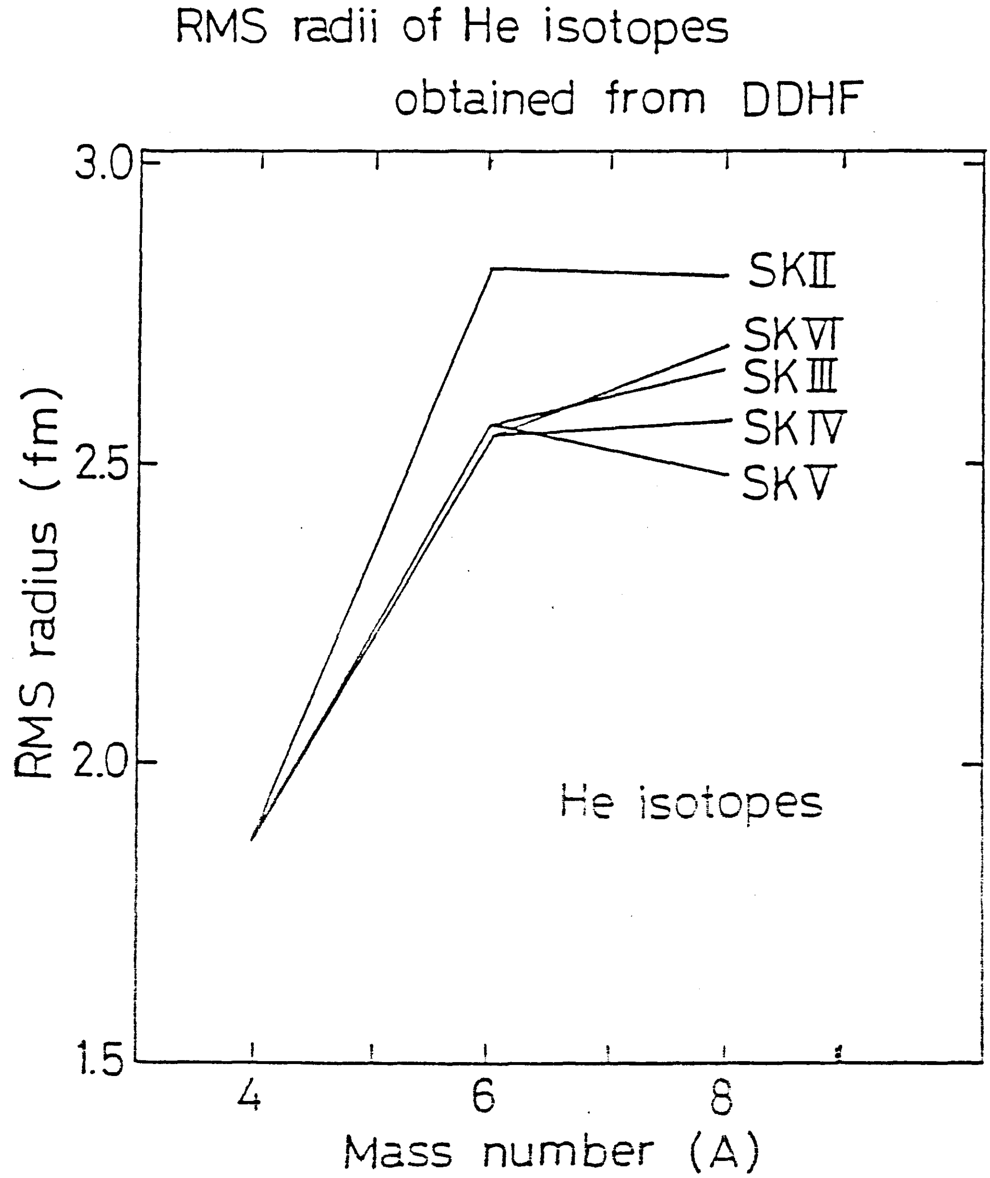
RMS radii of He isotopes
obtained from DDHF
RMS radius (fm)
3.0
2.5
2.0
1.5
4
6
8
Mass number (A)
SKII
SKVI
SKIII
SKIV
SKV
He isotopes

Figure 54

Figure 55

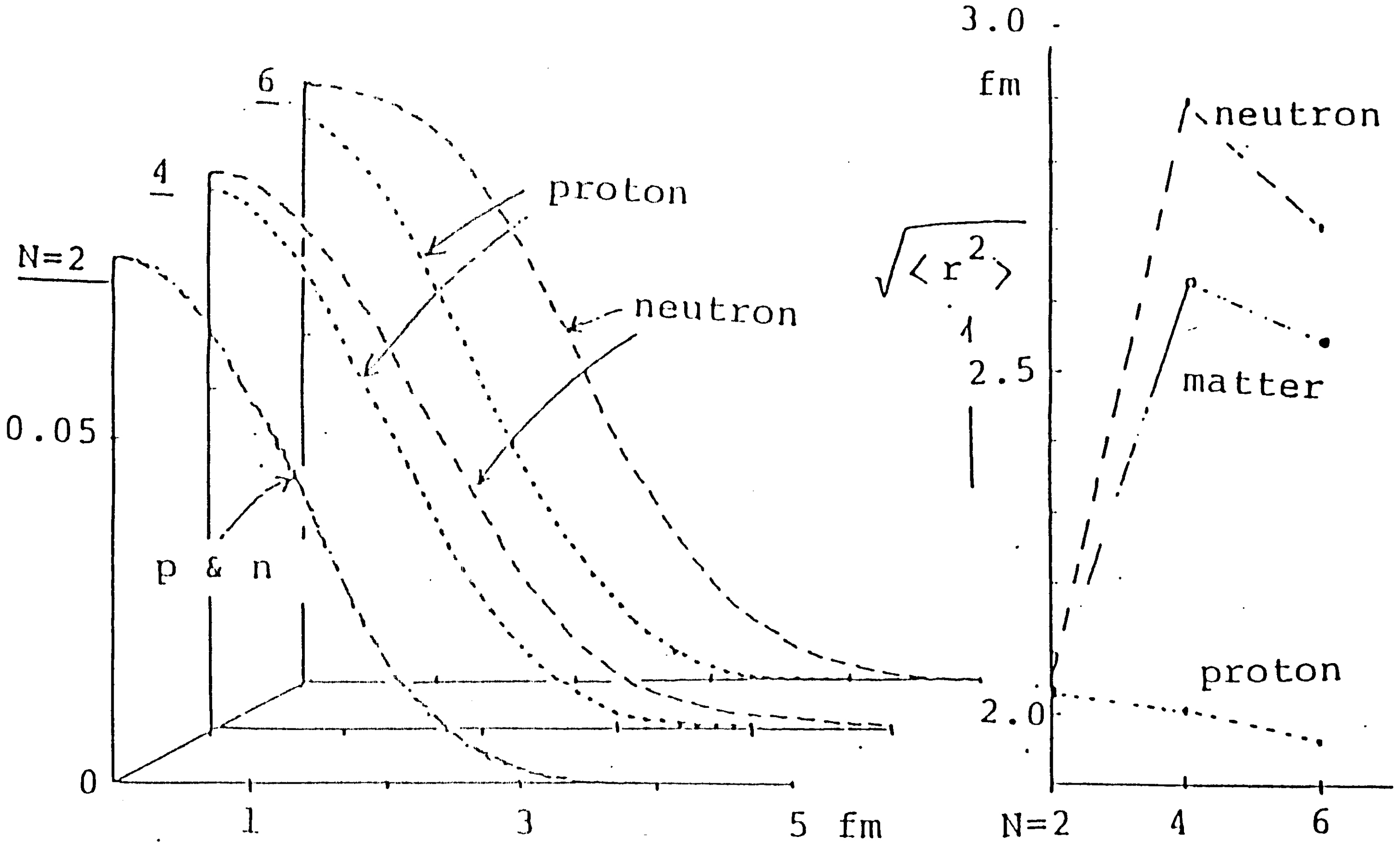

Proton and neutron distribution of He isotopes calculated by a Hartree-Fock method.

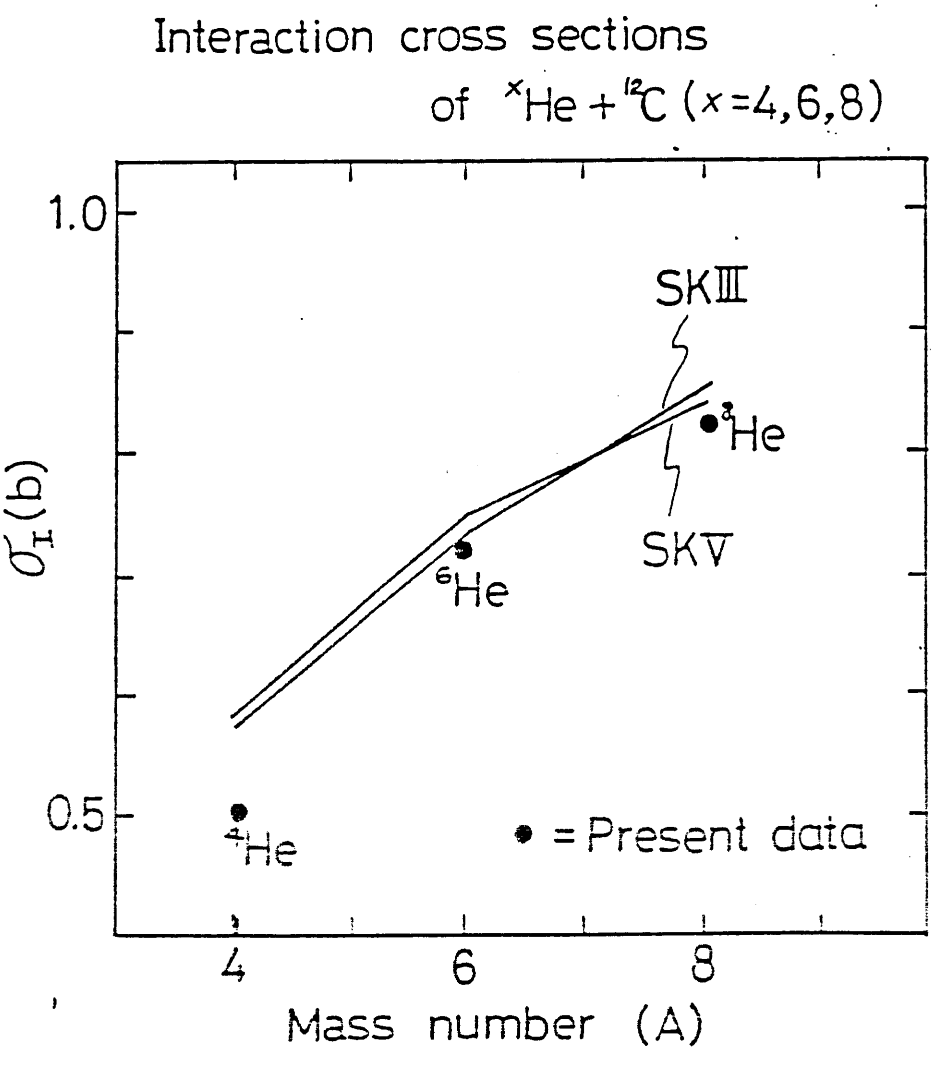
Interaction cross sections
of ^{x}He + ^{12}C (x=4,6,8)
1.0
0.5
σ_I(b)
SKIII
SKV
^{8}He
^{6}He
^{4}He
• = Present data
4
6
8
Mass number (A)

Figure 56

in 5 percent level. This DDHF calculation is considered to be reliable for ^6He and ^8He. However, it is not so reliable for ^3He and ^4He.

The isobar dependence of interaction radii for ^6He between ^6Li and that for ^8He between ^8Li are observed in this experiment. The radii of He isotopes (A=6,8) are about 0.1 fm larger than that of Li isotopes (A=6,8), respectively. The effect is generally explained as that of the symmetry energy in the Weizsäcker-Bethe mass formula.[26,27] According to this mass formula the binding energy ($B(Z,A)$) of nucleus is written as

$$B(Z,A) = a_{vol}A - a_{surf}A^{2/3} - a_{sym}(N-Z)^2/A - a_C Z^2/A^{1/3} + \delta \qquad (5.2)$$

where Z the number of proton, N the number of neutron and A is the number of nucleon, respectively. The coefficients in the equation show volume energy (a_{vol}), surface energy (a_{surf}), symmetric energy (a_{sym}), Coulomb energy (a_C) and pairing energy (δ), respectively. In comparison ^6He with ^6Li, the volume energy and surface energy terms are canceled because both nuclei have the same A number. Since the symmetric energy term causes weakness of the binding energy of ^6He, the radius of ^6He is greater than that of ^6Li. The Coulomb and pairing energy terms cause the opposite effect, however these are smaller than the effect due to the symmetric energy term. In the case of ^8He and ^8Li, we discussed in the same way.

In order to confirm this discussion we compared the radii of ^7Li and ^7Be. The symmetric and pairing energy terms of ^7Li and ^7Be are the same value and the difference of the Coulomb energy term is negligible. Because of this reason the radii of ^7Li and ^7Be should be the same value. Very recently we obtained the radius of ^7Be in this experiment. The result supported the discussion above. (The radius of ^7Be will be reported in a next paper.)

In this way we explained isobar dependence generally, however, further theoretical work is needed to understand the behaviour of interaction nuclear radii.

5.3. Conclusions

We have successfully demonstrated a novel use of secondary beams of unstable nuclei produced by the projectile fragmentation process in high-energy heavy-ion collisions. Interaction cross sections for He,Li and ^{9}Be isotopes at 790 MeV/nucleon on Be, C, Al targets were measured by a transmission type experiment. We have shown that the interaction cross sections yield interaction radii which are related to the matter distributions of nuclei. The interaction radii defined in Eq. (2.5) are well determined with a typical uncertainty of 0.02 fm. The fact that the interaction radii of projectile nuclei are almost constant, irrespective of the target nuclei, shows that this quantity is characteristic of a nucleus. The measured interaction radii show good agreement with the RMS radii obtained from electron scattering experiments. The present experiment is the first to measure the size of the β-unstable nuclei systematically in the light-mass region.

Although changes in the interaction radii of He and Li isotopes are qualitatively understood, further work is required to obtaine knowledge about unstable nuclei. The large deviation of the ^{11}Li radius from the $A^{1/3}$ dependence seems challenging for better understanding. Soon more data up to $A = 17$ will be analyzed and the dependence of the interaction radii on isobars, isotopes and isotones in a wide range will be revealed.

The presently developed technique to handle radioactive nuclear beams opens up a wide possibility of studies in the properties of β-unstable nuclei. Studies in this new field will bring further insight into many aspects of nuclei and also offer a area where the nuclear many-body theory can be tested.

Acknowledgement

I am extremely grateful to Prof. K.Niu who has shared his knowledge with me and allowed me to study nuclear physics involving counter techniques at the Lawrence Berkeley Laboratory. I also wish to express great appreciation to Prof. K.Sugimoto, Prof. Y.Shida, and Prof. N.Takahashi who trained me on so many occasions. I wish to give special thanks to my adviser Dr. I.Tanihata who has helped me in a multitude of ways. I wish to thank Mr. Y.Matsuyama, Mr. T.Fujino and Mr. F.S.Bieser for their technical assistance. Many thanks go to Dr. H.Hamagaki, Dr. O.Hashimoto, Dr. T.Kobayashi and Dr. Y.Nojiri who worked on many shifts even at midnight. I wish to thank Miss H.Saito who drew many diagrams for this thesis. Dr. S.Saito and the member of the G-lab. were of greatest assistance with their advice on theoretical calculations. Many thanks also go to Dr. T.Otofuji and Dr. R.Tatsuoka who helped me in the computer work. This work has been supported by the Director, Division of Nuclear Physics of the Office of High Energy and Nuclear Physics of the U.S. Department of Energy under Contract DE-AC03-76SF00098, the INS-LBL Collaboration Program, and by the Japan-U.S. Joint Program for High-Energy Physics.

References

1. E.M.Lyman et. al., Phys. Rev. **84,** 626 (1931).

2. R.Hofstadter, Revs. Mod. Phys. **28,** 214 (1956).

3. R.Hofstadter, Ann. Rev. Nucl. Science **7,** 231 (1957).

4. V.L.Fitch and J.Rainwater, Phys. Rev. **92,** 789 (1953).

5. P.Brix and H.Kopfermann, Revs. Mod. Phys. **30,** 517 (1958).

6. S.Fernbach, R.Serber and T.B.Taylor, Phys. Rev. **75,** 1352 (1949).

7. H.Feshbach, C.E.Porter and V.F.Weisskopf, Phys. Rev. **96,** 448 (1954).

8. H.Feshbach, Ann. Rev. Nucl. Science **8,** 49 (1958).

9. H.J.Emrich et. al., 4th Int. Conf. on Nuclei Far From Stability, CERN 81-09, P33 (1981).

10. E.W.Otten, Nucl. Phys. **A354,** 471c (1981).

11. D.E.Greiner et.al., Phys. Rev. Lett. **35** 152 (1975).

12. A.S.Goldhaber and H.H.Heckman, Ann. Rev. Nucl. Part. Sci. **28,** 161 (1978).

13. T.J.M.Symons et. al., Phys. Rev. Lett. **42,** 46 (1979).

14. A.S.Goldhaber, Phys. Lett. **53B,** 306 (1974).

15. J.Jaros et. al., Phys. Rev. **C18,** 2273 (1978).

16. H.L.Bradt and B.Peters, Phys. Rev **77,** 54 (1950).

17. D.L.Cheshire et al., Phys. Rev. **D10,** 25 (1974)

18. P.J.Lindstrom et. al., Bull. Ann. Phys. Soc. **17,** 488 (1972).

19. J.S.McCarthy et. al., Phys. Rev. Lett. **25,** 884 (1970).

20. U.Erich et. al., Z. Phys. **208,** 209 (1968).

21. Atomic data and Nuclear table, Vol.14, No.5, 6 (1974)

22. P.J.Karol, Phys. Rev. **C11,** 1203 (1975).

23. M.Beiner, R.J.Lombard and D.Mas, Nucl. Phys. **A249,** 1 (1975).

24. H.Sato and Y.Okuhara, INS-Rep. 546 July (1985).

25. J.W.Negele, Phys. Rev. **C1**, 1260 (1970).

26. C.F.Weizsäcker, Z.Physik 96, 431 (1935).

27. H.A.Bethe and R.F.Bacher, Rev. Mod. Phys. 8, 82 (1936).

Figure captions

Fig 1 : A schematic diagram of the projectile fragmentation process.

Fig 2 : A schematic diagram of the rigidity selection.

Fig 3 : An example of the distributions of projectile fragments at F2.

Fig 4 : An example of a charge separation.

Fig 5 : The secondary beam line at Bevalac (Beam 42).

Fig 6 : A schematic diagram for energy loss in the production target.

Fig 7 : Momentum dispersion vs. Thickness of the production target.

Fig 8-13 : The pulse heights vs. TOF for He and Li isotopes.

Fig 14 : The interaction radii of stable nuclei obtained from other experiments[15,16].

Fig 15 : The dependence of the statistical errors of the interaction cross section on the attenuation factor γ.

Fig 16 : The perspective view of the experimental setup.

Fig 17 : The plan view of the experimental setup.

Fig 18 : The pulse height distribution of a scintillation counter.

Fig 19 : The time resolution between SBT1,2 and SBT3,4.

Fig 20 : The bending angle resolution.

Fig 21 : The circuit diagram of the trigger system.

Fig 22 : A block diagram for the data taking system.

Fig 23 : The pulse height distribution after the reaction target.

Fig 24,25 : The rigidity separations for He and Li isotopes after the reaction target.

Fig 26,27 : Beam profiles at the PAT3,4 for target-out run and for target-in run.

Fig 28-35 : The scattering-out probability (P_m) as a function of the target thickness.

Fig 36-43 : The interaction cross section for He and Li isotopes obtained in each run.

Fig 44-45 : The results of the interaction cross sections of He and Li isotopes.

Fig 46 : The difference of R_I for projectile vs. mass number A .

Fig 47 : The difference of R_I for target nuclei.

Fig 48 : The interaction radii of He and Li isotopes.

Fig 49 : R_I is the interaction radii obtained from the present experiment, R_{rms}^{e} is the charge rms radius obtained from the electron scattering experiment and R_{rms}^{G} is the calculated charge rms value of the Gaussian density distribution by which the R_I is reproduced.

Fig 50 : The Gaussian density distribution of He - C obtained by semi-classical optical model.

Fig 51 : The Gaussian density distribution for He isotopes

Fig 52 : The Gaussian density distribution for Li isotopes

Fig 53 : The rms radii of O, Na, K and Rb isotopes against the neutron number (N).

Fig 54 : The rms radii of He isotopes.

Fig 55 : The proton and the neutron density distributions for He isotopes.

Fig 56 : The calculated interaction cross sections and the experimental σ_I .

Appendix

The calculation methods of the interaction cross section, based on the semi-classical optical model[22], are described in appendix.

Based on the Glauber approximation of high-energy nuclear cillision, the interaction cross section can be written as

$$\sigma_I = 2\pi\int_0^{\infty}[1-T(r)]r\,dr \tag{A.1}$$

where $T(r)$ is the probability that the projectile will pass through the target with an impact parameter r without interaction. The definition of the coordinate for calculating the transparancy function $T(r)$ are shown in Fig. A1. A cylindrical coordinate system is defined, the origin O as the center of the target nucleus, the z axis as the beam direction and r as the impact parameter. The transparancy function $T(r)$ is given by

$$T(r) = \exp\left[-\int_{-\infty}^{\infty}Q(r,z)dz\right] \tag{A.2}$$

where $Q(r,z)$ is called the "thickness function" by Glauber, and gives the probability of interaction per unit path length between z and $z+dz$ at fixed (r,z). This is given by

$$Q(r,z)dz = \overline{\sigma}2\pi\int_{-\infty}^{\infty}\eta\int_{-\infty}^{\infty}\rho_T(r,z,b,\eta)\rho_P(r,z,b,\eta)b\,db\,dz \tag{A.3}$$

where $\overline{\sigma}$ is the average nucleon-nucleon collision cross section, which is given by

$$\overline{\sigma} = \left[\frac{Z_T Z_P}{A_T A_P}+\frac{N_T N_P}{A_T A_P}\right]\sigma_{ii} + \left[\frac{Z_T N_P}{A_T A_P}+\frac{Z_P N_T}{A_P A_T}\right]\sigma_{ij} \tag{A.4}$$

where A_T, Z_T are the mass and the atomic numbers of the target nucleus, A^P, Z_P are the mass and the atomic numbers of the projectile nucleus, and σ_{ii} is the proton-proton (neutron-neutron) total cross section, σ_{ij} is the proton-neutron total cross section, and ρ_T, ρ_P are the density distribution of the target and projectile nucleus, respectively. We calculated the interaction cross sections using the Gaussian-type density distributions.

$$\rho(r) = \frac{A}{a^3\pi^{2/3}}\exp[-\frac{r^2}{a^2}] \tag{A.5}$$

where the factor a is the width parameter of the Gaussian distribution and is related to the root-mean-square radius R^G_{rms} as

$$R^G_{rms} = \sqrt{1.5}a \tag{A.6}$$

As the results, the interaction cross section in fm^2 are given by

$$\begin{aligned} \sigma_I &= \pi(a_T^2+a_P^2)[E_1(\chi)+\ln(\chi)+0.5772] \\ E_1(\chi) &= \int_\chi^\infty \frac{e^{-u}}{u}du \\ \chi &= \frac{\pi^2\overline{\sigma}\rho_T(0)\rho_P(0)a_T^3a_P^3}{a_T^2a_P^2} \end{aligned} \tag{A.7}$$

where a_T , a_P are the width parameters, in fm, for the Gaussian distribution for target and projectile nuclei.

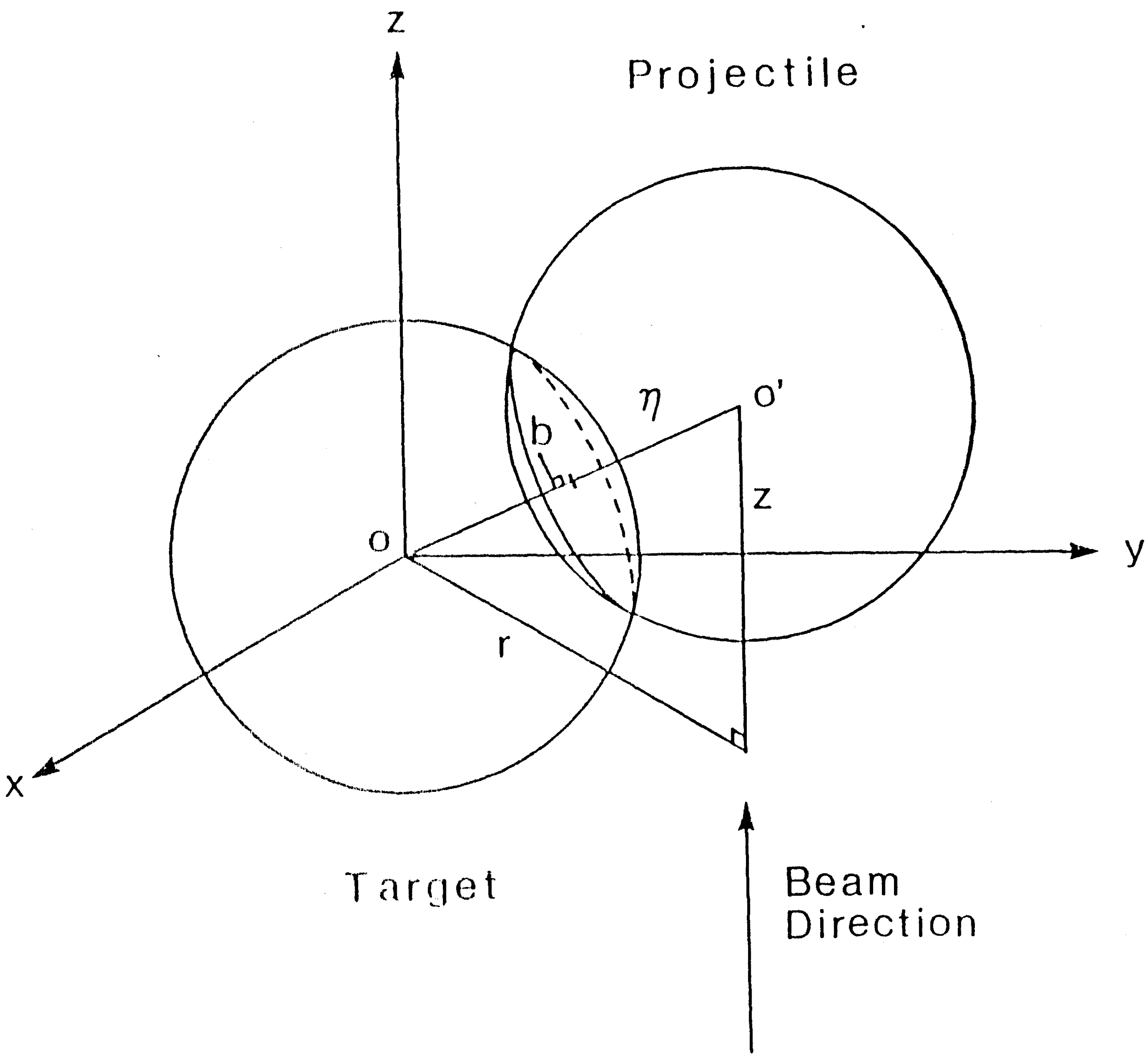

FigureA1